Stratocumulus Transitions

in Present-day and Future Climate

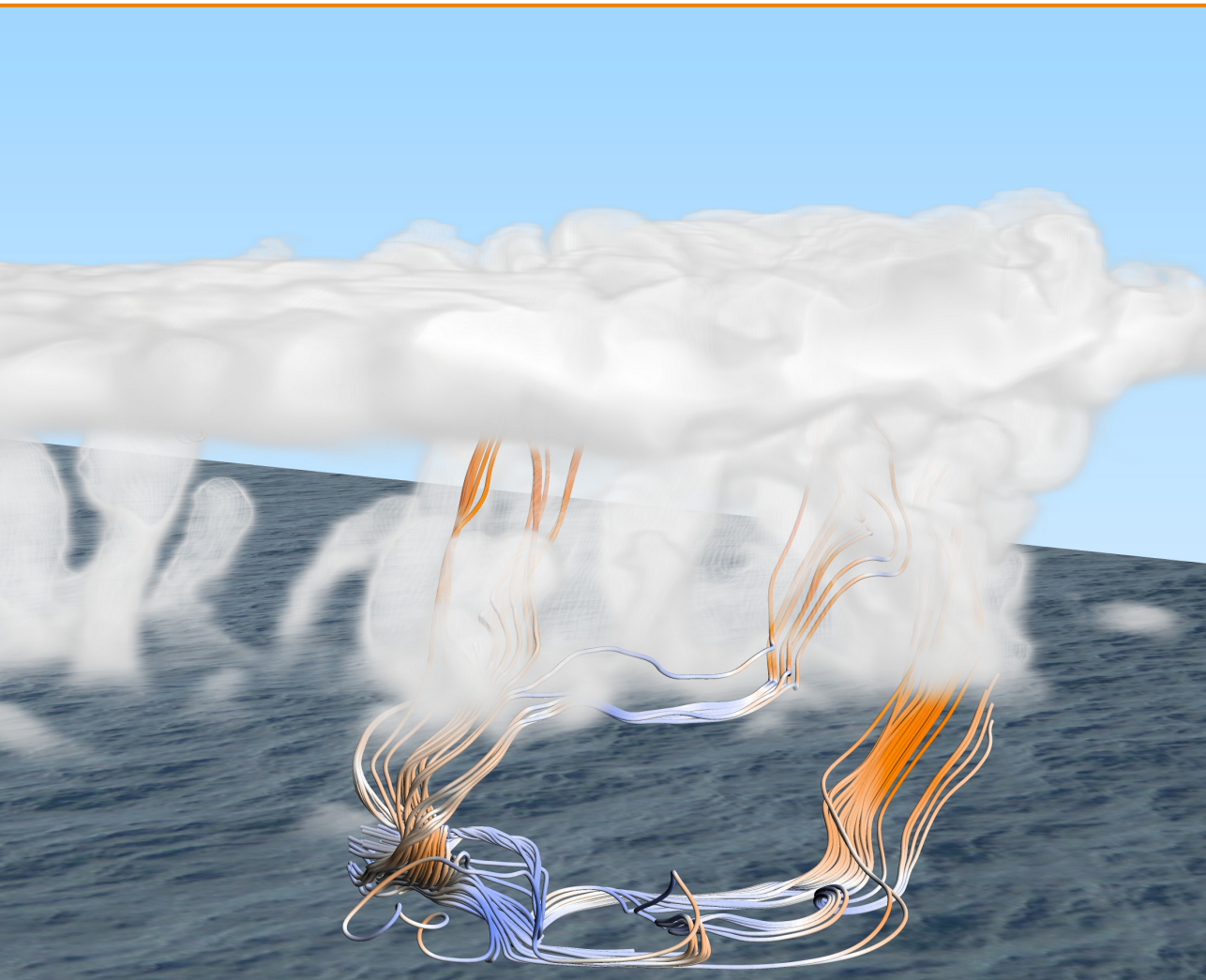

Johan van der Dussen

Stratocumulus Transitions in Present-day and Future Climate

Cover illustration: volume rendering of the cloud liquid water during a stratocumulus transition, as simulated with the Dutch atmospheric large-eddy simulation model.

Stratocumulus Transitions in Present-day and Future Climate

Proefschrift

ter verkrijging van de graad van doctor
aan de Technische Universiteit Delft,
op gezag van de Rector Magnificus prof. ir. K.Ch.A.M. Luyben;
voorzitter van het College voor Promoties,
in het openbaar te verdedigen
op maandag 22 juni 2015 om 12.30 uur

door

Jan Jozias VAN DER DUSSEN

natuurkundig ingenieur
geboren te Dordrecht, Nederland

Dit proefschrift is goedgekeurd door
promotor: Prof. dr. A.P. Siebesma en
copromotor: Dr. S.R. de Roode

Samenstelling promotiecommissie bestaat uit:

Rector Magnificus,	voorzitter
Prof. dr. A.P. Siebesma,	Technische Universiteit Delft, promotor
Dr. S.R. de Roode,	Technische Universiteit Delft, copromotor

onafhankelijke leden:

Prof. dr. ir. H.W.J. Russchenberg,	Technische Universiteit Delft
Prof. dr. ir. B.J. Boersma,	Technische Universiteit Delft
Prof. dr. M.R. van den Broeke,	Universiteit Utrecht
Dr. R. Boers,	Koninklijk Nederlands Meteorologisch Instituut
Dr. J. Teixeira,	Jet Propulsion Laboratory, USA

Dit onderzoek is tot stand gekomen met financiële ondersteuning van het Seventh Framework Program (FP7/2007-2013) van de Europese Unie, onder subsidieovereenkomst n° 244067. Er is gebruik gemaakt van de supercomputer-faciliteiten van SURFSARA, met financiële ondersteuning van NWO.

Geprint door: Proefschriftmaken.nl | Uitgeverij Boxpress, 's Hertogenbosch

Contents

Stratocumulus-transities in het Huidige en Toekomstige Klimaat

Wolken hebben netto een sterk afkoelend effect op onze planeet, doordat ze een groot deel van de invallende zonnestraling weerkaatsen. Om tot betrouwbare verwachtingen voor het wereldwijde klimaat te komen, moet bewolking dus correct worden gerepresenteerd door klimaatmodellen. Momenteel zijn er echter grote verschillen in de verwachte temperatuurstijging tussen klimaatmodellen onderling. Een van de belangrijkste oorzaken van deze verschillen is de onzekerheid in de representatie van wolken, en met name stratocumuluswolken.

Stratocumuluswolken zijn laaghangende wolken die een vrijwel geheel gesloten wolkendek vormen. Ze laten maar weinig zonlicht door, waardoor ze vaak geassocieerd worden met grijs en somber weer. Stratocumuluswolken komen veelvuldig voor boven oceanen in de subtropen, waar ze enorme oppervlakken van enkele miljoenen vierkante kilometer kunnen beslaan. Wanneer ze vanuit de subtropen worden meegevoerd met de passaatwinden richting de evenaar, vindt er typisch een transitie plaats waarbij de stratocumulus langzaam dunner wordt en uiteindelijk opbreekt. Tegelijkertijd ontstaan er stapelwolken, die een veel lagere bewolkingsgraad hebben en daardoor minder zonlicht reflecteren. Stratocumulus-transities zorgen dus voor een abrupte afname van het door wolken geïnduceerde netto afkoelingseffect, wat ze van bijzonder belang maakt voor het klimaat.

Tegelijkertijd is het representeren van stratocumulus-transities zeer uitdagend voor klimaatmodellen, omdat hun ontwikkeling sterk afhankelijk is van transport van onder ander vocht door kleinschalige turbulentie. Door hun grove resolutie kunnen klimaatmodellen processen met een typische grootte van honderd kilometer of minder niet expliciet simuleren. Daarom wordt het turbulente transport, samen met andere wolkengerelateerde processen op een versimpelde statistische manier gerepresenteerd door middel van parameterisaties, wat veel onzekerheid introduceert.

Tijdens dit promotieproject hebben we stratocumuluswolken en hun transities gesimuleerd met een numeriek model dat, in tegenstelling tot klimaatmodellen, in staat is om de interactie tussen turbulentie en stratocumuluswolken tot in detail weer te geven. In hoofdstuk twee vergelijken we zes van deze zogenaamde large-eddy simulatiemodellen met metingen die verzameld zijn tijdens een stratocumulustransitie. Alle modellen blijken in staat te zijn om de belangrijkste eigenschappen van de transitie correct weer te geven, waaronder het langzaam oplossen van stratocumulus en het gelijktijdig ontstaan van stapelwolken.

De simulaties leveren een schat aan gegevens over de driedimensionale structuur van de atmosfeer, die onmogelijk uit metingen gehaald kan worden. Deze gegevens stellen ons in staat om de oorzaken van het oplossen en opbreken van stratocumulus tijdens transities tot in detail te onderzoeken.

Een van deze oorzaken kan gezocht worden in de verandering van de structuur van de turbulentie in de atmosferische grenslaag waarin de stratocumuluswolken zich bevinden. Aan het begin van de transitie is de grenslaag nog relatief ondiep, waardoor turbulentie de lucht daarin verticaal goed door kan mengen. Dit zorgt ervoor dat vocht dat verdampt van het oceaanoppervlak gemakkelijk de stratocumuluswolk kan bereiken, waardoor deze gevoed en in stand gehouden wordt. Naarmate de transitie vordert wordt de grenslaag langzaam dieper en neemt de afstand tussen de wolken en het oppervlak toe. Er is gesuggereerd dat de turbulentie hierdoor uiteindelijk niet meer in staat zou zijn om de hele grenslaag goed door te mengen. Deze zogenaamde ontkoppeling zou ervoor zorgen dat de vochttoevoer naar de stratocumulus vrijwel volledig wordt afgesneden, waardoor deze snel uitdroogt en oplost. In hoofdstuk twee laten we echter met behulp van de modelresultaten zien dat ontkoppeling een kleiner effect heeft op het vochttransport dan eerder werd gedacht.

Een ander proces dat vaak verantwoordelijk wordt gehouden voor het opbreken van stratocumuluswolken is entrainment. Bij dit proces wordt lucht vanuit de relatief warme en droge vrije troposfeer ingemengd in de grenslaag. Entrainment zorgt dus voor opwarming en uitdroging van stratocumuluswolken en wordt daarom geassocieerd met het dunner worden ervan. In hoofdstuk drie leiden we een vergelijking af die beschrijft hoe de totale hoeveelheid gecondenseerd water in de wolk verandert in de tijd. Door middel van deze vergelijking kunnen we laten zien dat entrainment inderdaad een belangrijke oorzaak is voor het dunner worden van stratocumuluswolken tijdens een transitie. We laten echter ook zien dat andere processen, zoals de toevoer van vocht vanaf het zeeoppervlak, sterk genoeg kunnen zijn om dit dunner worden te stoppen zelfs voor condities waarbij eerdere studies een onvoorwaardelijk opbreken van de wolk voorspelden.

In het tweede deel van dit proefschrift onderzoeken we de invloed van klimaatopwarming op stratocumuluswolken. In hoofdstuk vier voeren we een reeks simulaties uit van stratocumuluswolken voor condities die representatief zijn voor het huidige klimaat. Vervolgens bootsen we in een tweede reeks simulaties een toekomstig klimaat na door de temperatuur van het zeewater en van de atmosfeer te verhogen. Deze geïdealiseerde klimaatverstoring zorgt in alle simulaties voor een afname van de dikte en daarmee de reflectiviteit van de stratocumuluswolken. Dit suggereert dat in een toekomstige klimaat meer straling van de zon het aardoppervlak zal bereiken dan in het huidige klimaat. Op deze manier zorgen stratocumuluswolken voor een versterking van de klimaatopwarming.

Als gevolg van de opwarming van het klimaat zal de grootschalige atmosferische circulatie tussen de evenaar en de subtropen, de zogenaamde Hadley-circulatie, afzwakken. In hoofdstuk vijf laten we zien dat het afzwakken van de Hadley-circulatie het opbreken van stratocumuluswolken tijdens transities uitstelt. Effectief leidt dit tot een toename van de hoeveelheid stratocumuluswolken in een toekomstig klimaat. Dit mechanisme werkt de afname van de hoeveelheid stratocumuluswolken als gevolg van de klimaatopwarming die we in hoofdstuk vier vonden, tegen, maar is waarschijnlijk niet sterk genoeg om het volledig te compenseren.

Summary

Stratocumulus Transitions in Present-day and Future Climate

Clouds have a strong net cooling effect on our planet, as they reflect a large part of the incident solar radiation. To be able to make accurate forecasts of the global climate, cloudiness should therefore be correctly represented by climate models. Currently, however there are large differences in the forecasted temperature increase among climate models. One of the most important causes of these differences is the uncertainty in the representation of clouds, in particular of stratocumulus clouds.

Stratocumulus clouds are low clouds that often form an almost completely closed cloud deck. Only little sunlight passes through them, so that they are often associated with grey and dull weather. Stratocumulus clouds are frequently found over oceans in the subtropics, where they can cover enormous areas of several millions of square kilometers. When they are advected by the trade winds from the subtropics toward the equator, a transition typically occurs during which the stratocumulus slowly thins and eventually breaks up. Simultaneously, cumulus clouds appear that have a much lower cloud cover and therefore reflect less sunlight. Hence, stratocumulus transitions cause an abrupt decrease of the cloud-induced net cooling effect, which makes them particularly important for climate models.

At the same time, the representation of stratocumulus clouds is extremely challenging for climate models, since their development strongly depends on the transport of among others moisture by small-scale turbulence. Due to their coarse resolution, climate models are unable to explicitly simulate processes with typical sizes of a hundred kilometers or less. Hence, turbulent transport, together with other cloud related processes, is represented in a simplified statistical manner by parameterizations, which introduces much uncertainty.

During this thesis project we have simulated stratocumulus clouds and their transitions with a numerical model that, in contrast to climate models, is capable of representing the interaction between turbulence and clouds in detail. In chapter two we compare the results of six of these so-called large-eddy simulation models with measurements that had been gathered during a stratocumulus transition. All models are shown to be capable of correctly representing the main features of the transition, including the slow thinning of the stratocumulus and the simultaneous development of cumulus clouds.

The simulations yield a wealth of data on the three-dimensional structure of the atmosphere, which is impossible to obtain from measurements. These data allow us to investigate the causes of the thinning and breaking up of stratocumulus clouds during transitions in detail.

One of these causes can be sought in the change of the turbulent structure of the atmospheric boundary layer in which the stratocumulus resides. At the start of the transition, the boundary layer is still rather shallow, allowing turbulence to

vertically mix the air in it relatively well. Hence, the moisture that evaporates from the ocean surface can easily reach the cloud layer, thereby feeding and maintaining it. As the transition progresses, the boundary layer becomes deeper and the distance between the clouds and the surface increases. It has been suggested that eventually turbulence will not be sufficiently strong anymore to maintain the well-mixed structure of the boundary layer. This so-called decoupling would cause the moisture transport to the stratocumulus to be almost completely cut off, causing it to rapidly dry and dissolve. However, in chapter two we show from the model results that decoupling has less effect on the humidity transport than was originally thought.

Another process that is often held responsible for the breaking up of stratocumulus clouds is entrainment. In this process, air from the relatively warm and dry free troposphere is mixed into the boundary layer. Hence, entrainment causes drying and warming of the stratocumulus cloud and is therefore associated with its thinning. In chapter three we derive an equation that describes the change with time of the total amount of condensed water in the cloud. Using this equation we argue that entrainment is indeed an important cause for the thinning of stratocumulus clouds during a transition. On the other hand, we also show that other processes, such as the supply of moisture from the sea surface, can be strong enough to diminish this thinning, even for conditions for which earlier studies predicted an unconditional breakup of the cloud.

In the second part of this thesis, we investigate the effect of the warming of the climate on stratocumulus clouds. In chapter four, we perform a set of simulations of stratocumulus clouds for conditions that are representative for the current climate. In a second set of simulations we mimic a future climate by increasing the temperature of the atmosphere and of the sea. This idealized climate perturbation causes a decrease of the thickness and hence the reflectivity of the stratocumulus clouds in all simulations. This suggests that, in a future climate, more solar radiation will be able to reach the Earth's surface than in the current climate. This way, stratocumulus clouds will enhance the warming of the climate.

As a result of a warming of the climate, the large-scale atmospheric circulation between the equator and the subtropics, the so-called Hadley circulation, will weaken. In chapter five we show that a weakening of the Hadley circulation delays the breakup of stratocumulus clouds during transitions. Effectively, this leads to an increase of the amount of stratocumulus clouds in a future climate. This mechanism therefore counteracts the reduction of the amount of stratocumulus clouds in response to a climate warming that we found in chapter four, but will likely not be strong enough to completely compensate for it.

1

General Introduction

1.1 Clouds and Climate

Our planet is warming up steadily as a result of the increase of the greenhouse gas concentration in the atmosphere. This global warming has consequences for all life on Earth. Many institutes all over the world are therefore simulating the climate using General Circulation Models (GCMs) in order to forecast the magnitude of the temperature increase.

Figure 1.1a shows with black dots the global mean temperature change due to a doubling of the CO_2 concentration in the atmosphere as forecasted by 11 state-of-the-art GCMs that participated in the most recent Climate Model Intercomparison Project (CMIP5). The diagram indicates that the temperature change forecasted by the different models ranges between 2 and 4.5 K. Nowadays, much research is dedicated to evaluating what processes are responsible for this considerable spread in order to be able to reduce it.

The climate system is influenced by the incredibly complex interplay of many physical processes over a large range of scales. In particular, there are processes that depend on the global near-surface temperature but at the same time affect it. This means that a change of the temperature will induce changes in such processes, which will in turn feedback to the temperature change thereby either enhancing or weakening it. An example is the water vapor feedback. In a warmer climate the atmosphere will contain more water vapor, which is a strong greenhouse gas. Therefore, an increase of the water vapor in the atmosphere will cause the Earth's temperature to increase even further. The water vapor feedback is therefore positive (Cess et al., 1990; Held and Soden, 2000).

Through careful analysis of GCM results, the relative importance of climate feedbacks can be deduced. In Figure 1.1a, the total temperature change for each of the GCMs has been split into contributions of 1) the adjusted radiative forcing as a result of the enhanced greenhouse gas concentration F', 2) the combined water vapor and lapse-rate feedbacks 'wv+lr', 3) the surface albedo feedback 'alb', 4) the cloud feedback 'cl' and 5) a residual 'res' (Vial et al., 2013). The diagram shows that the GCM results are rather robust for some of these mechanisms, for instance for the surface albedo feedback. In contrast, the magnitude and even

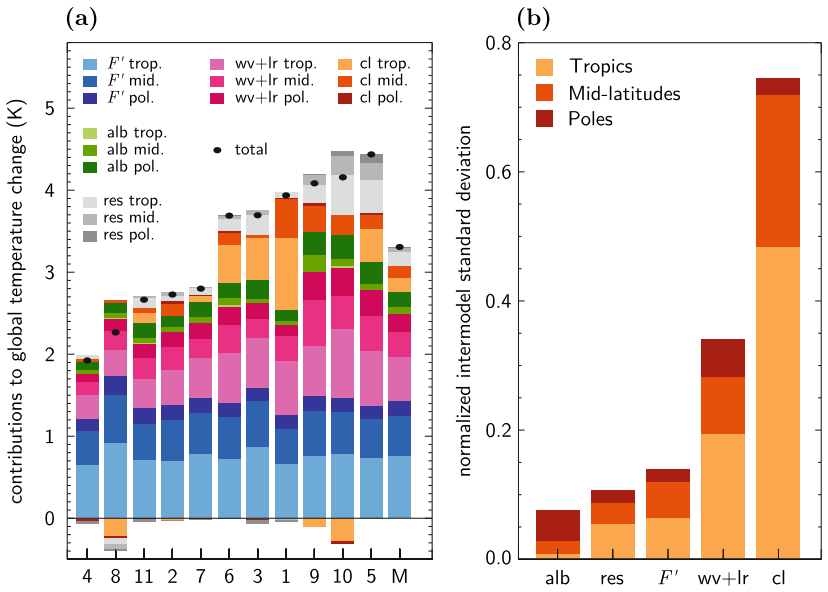

Figure 1.1. (a) The equilibrium global-mean surface temperature change as a result of a doubling of the atmospheric CO_2 concentration, as estimated from 11 GCMs that participated in CMIP5. The total temperature change (black dot) is split into individual contributions from the change of the radiative forcing (F'), the surface albedo feedback (alb), the combined water vapor and lapse-rate feedbacks (wv+lr) and the cloud feedback (cl) according to the legend. Every contribution is subdivided into contributions from the tropics, the mid-latitudes and the poles. The residual is shown in grey shades. The 'M' on the horizontal axis denotes the multi-model mean. (b) The normalized intermodel standard deviation for each of the contributions to the global temperature change, subdivided into contributions from the three latitudinal bands. Figures adapted from Vial et al. (2013) and reprinted with the permission of Springer Science+Business Media.

the sign of the cloud feedback varies significantly among the models. On average, cloud feedbacks have a small positive contribution to the global mean temperature change. In other words, changes in cloudiness as a result of a warming of the climate enhance global temperature increase.

Figure 1.1b shows the extent of the disagreement among the GCMs for each of the mechanisms, as measured by the normalized intermodel standard deviation. Only the six models with the smallest residual were used in this analysis. Clearly, the representation of cloud processes, in particular in the tropics and mid-latitudes, is responsible for most of the spread in the estimated global mean temperature change (Cess et al., 1989, 1990; Bony and Dufresne, 2005; Soden and Held, 2006; Williams and Webb, 2009).

So what is the role of clouds in the climate system? Most importantly, the presence of clouds severely decreases the amount of energy from the sun that reaches the surface of the Earth as they reflect a large portion of the incident solar

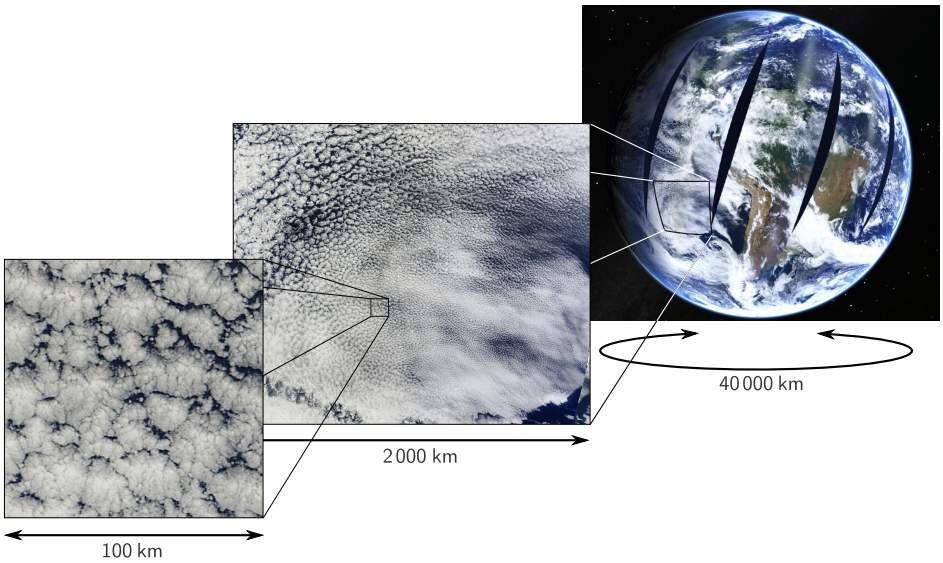

Figure 1.2. Satellite images retrieved from the MODIS instrument aboard the Aqua satellite (https://earthdata.nasa.gov/labs/worldview/) projected onto the globe using Google Earth. The data were obtained on 26 August 2013. The footprint of the instrument is not wide enough to cover the entire planet at the low latitudes, resulting in the black stripes visible in the rightmost panel.

radiation back to space. This gives them their typical bright white appearance when viewed from space, as is visible in the rightmost panel of Figure 1.2. The contrast between the white clouds and the underlying surface is particularly large over oceans, which appear dark from space since they absorb over 90 % of the incoming solar radiation. The impact of clouds on the planet's albedo is therefore largest over the oceans, giving marine clouds an important global cooling effect (Ramanathan et al., 1989).

In addition to this cooling effect, clouds enhance the greenhouse effect as well. This can be explained as follows. Clouds absorb the infrared radiation that the planet emits and re-emit only part of it toward space. Their presence therefore decreases the amount of energy that the planet loses to space, thereby acting as a thermal insulator. The amount of radiation a cloud emits decreases strongly with its temperature. Clouds that are located at high altitudes are much colder than the Earth's surface. They therefore emit but a small amount of radiation so that they act as a relatively strong thermal insulator. This insulation effect partly offsets the cooling induced by their albedo effect. The temperature of clouds at low altitudes, on the other hand, is similar to that of the surface, which makes their insulating effect limited. For low clouds the albedo effect therefore dominates their total radiative effect (Randall et al., 1984). Hence, the induced net radiative cooling is significantly larger for low than for high clouds. This means that a change of the global low cloud amount as a result of global warming will have a much stronger feedback effect on the climate than a similar change in high cloudiness. It is

therefore not surprising that several studies have identified tropical and subtropical low clouds as the key contributors to the uncertainty of the magnitude of the cloud-climate feedback (Bony and Dufresne, 2005; Williams and Webb, 2009).

1.2 Stratocumulus Clouds

1.2.1 Occurrence

The occurrence of low clouds in the subtropics is strongly linked to the Hadley circulation, which is schematically represented in Figure 1.3. This large-scale circulation is driven by the differential heating of the Earth's surface by solar radiation. The average amount of incident solar radiation is highest at the equator and decreases toward the poles. The surface temperature therefore tends to be highest at the Equator, which triggers a mean ascent of air often resulting in the formation of deep convective clouds. Such clouds carry air to heights of up to 20 km until their ascent is stopped by the tropopause. This causes an outflow of air that moves poleward through the upper troposphere. The air descends again around the latitudes of 30°N and 30°S, where it creates persistent high-pressure systems.

The descending air is warm relative to the sea water and the air in the lower atmosphere at these latitudes. This contrast causes a stable temperature stratification, or thermal inversion, to develop in the lower atmosphere. The inversion separates the quiescent free troposphere above from the turbulent planetary boundary layer below. It acts as a lid that traps the moisture evaporating from the surface of the ocean inside the boundary layer. If enough moisture builds up, the boundary layer air becomes saturated and a cloud layer forms just below the inversion. Such stratiform clouds at low altitudes are called stratocumulus clouds. Stratocumulus clouds occur frequently in the presence of cool ocean surface currents, which can for instance be found just off the coasts of California, Peru and West Africa. At these locations stratocumulus fields often cover vast areas of several millions of square kilometers (Wood, 2012). A satellite derived image of such an extensive stratocumulus field is shown in the middle panel of Figure 1.2. Their high frequency of occurrence, persistence and their large impact on the albedo make stratocumulus clouds of particular relevance to the climate system. Hence, much research has in the past decades been dedicated to improve the understanding of the physics and dynamics of stratocumulus clouds.

1.2.2 Physics of Stratocumulus Clouds

Radiation

Stratocumulus clouds emit infrared radiation approximately as a black body. This emission causes a large energy loss at the top of the cloud layer resulting in a significant cooling tendency. This mechanism is referred to as cloud-top radiative cooling and it tends to thicken the cloud layer through two different mechanisms. First, it acts to lower the temperature of the cloud, thereby enhancing the condensation of water vapor into cloud droplets. Second, the cooling at cloud top destabilizes the boundary layer by generating a tendency for parcels at the

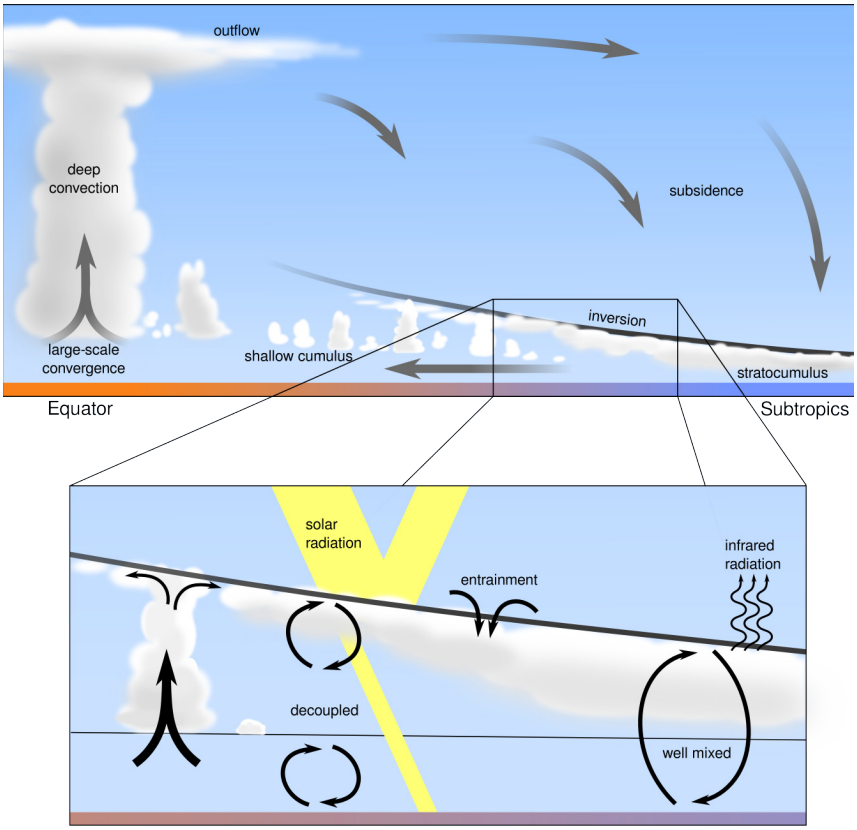

Figure 1.3. A schematic representation of the Hadley circulation and the cloud types that typically occur within this large-scale circulation (after Arakawa, 1975; Emanuel, 1994). The bottom panel zooms in on the stratocumulus transition regime within the Hadley circulation that is the main topic of this thesis.

top to sink, which induces mixing by turbulence throughout the upper part of the boundary layer (Lilly, 1968; Nicholls, 1989; Bretherton et al., 1999b). In stratocumulus-topped boundary layers, turbulence is therefore not only generated by heating from the surface but also by radiative cooling at the top of the boundary layer. As a result of the generation of turbulence at the top as well as at the bottom of the boundary layer, the air in stratocumulus-topped boundary layers is often vertically well mixed. This allows the moisture that evaporates from the surface to easily reach the stratocumulus layer, where it acts to thicken the cloud.

Stratocumulus clouds interact with solar radiation as well. This radiation has a much smaller wavelength then the infrared radiation emitted by the stratocumulus layer and is hence commonly called shortwave radiation. Up to 80 % of the incident solar radiation is reflected at the top stratocumulus cloud. A small part is absorbed by the cloud. This absorption causes a warming tendency that offsets the radiative

cooling of the cloud layer so that by day the cloud cools less strongly than during the night. Therefore, stratocumulus clouds are often found to be much thinner during the day than during the night (Bougeault, 1985; Turton and Nicholls, 1987; Duynkerke and Hignett, 1993; Caldwell and Bretherton, 2009).

Entrainment

The vigorous turbulent mixing in stratocumulus-topped boundary layers causes air from the free troposphere to be dragged into the boundary layer continuously, despite the stable thermal inversion that separates them. This process is called entrainment. In the first place, entrainment acts to deepen the boundary layer, which tends to increase the thickness of the stratocumulus cloud. On the other hand, the entrained air that originates from the free troposphere is warmer and drier than the air in the cloud. Therefore, entrainment tends to warm and dry the stratocumulus cloud, causing it to thin. Of these two competing effects, the cloud thinning effect due to entrainment typically dominates (Randall, 1984; De Roode et al., 2014). Enhanced entrainment is therefore often associated with thinning of stratocumulus clouds and has been suggested as an important cause for their break up (Randall, 1980; Deardorff, 1980a; De Roode and Duynkerke, 1997).

The entrainment rate depends on a large number of parameters, such as the strength of the inversion, the radiative cooling rate, the cooling as a result of evaporation of cloud droplets in the boundary layer and the turbulence in the boundary layer (Nicholls and Turton, 1986; Moeng, 2000; Stevens, 2002). This causes the modeling of the entrainment rate to be challenging. Furthermore, the entrainment velocity is only of the order of $1\,\mathrm{cm\,s^{-1}}$, which makes it particularly difficult to accurately measure it (De Roode and Duynkerke, 1997; Faloona et al., 2005; Carman et al., 2012). The process of entrainment therefore remains a very active field of research for stratocumulus clouds (Caldwell et al., 2005; Bretherton et al., 2007; Yamaguchi and Randall, 2012; Mellado et al., 2013).

Microphysics

Stratocumulus clouds typically generate only little precipitation, because of their limited depth of a few hundred meters. However, precipitation and in particular the sedimentation of cloud droplets is important to the evolution of stratocumulus clouds as these processes diminish the liquid water specific humidity near cloud top. This reduces the potential for evaporative cooling when cloud air mixes with warm and dry free tropospheric air, which leads to a reduction of the entrainment rate (Stevens et al., 1998; Uchida et al., 2010). Microphysics therefore has a significant indirect effect on the thickness of the stratocumulus layer (Ackerman et al., 2004).

Decoupling

Above, it was noted that stratocumulus-topped boundary layers are often vertically well mixed as a result of radiative cooling at the top of the cloud layer that destabilizes the boundary layer. This mixing causes humidity to be almost homogeneously distributed with height throughout the boundary layer, in particular for shallow boundary layers where the inversion is located below approximately 1 km height.

However, as the boundary layer deepens under the influence of entrainment, the mixing induced by cloud-top radiative cooling is often found to be insufficiently strong to maintain this well-mixed structure (Wyant et al., 1997). For such conditions, the boundary layer separates into the stratocumulus layer at the top that remains well mixed due to cloud top radiative cooling, and the subcloud layer that is mixed by the surface buoyancy flux (Bretherton and Wyant, 1997; Park et al., 2004; Wood and Bretherton, 2004). The air in between these layers is relatively quiescent. This phenomenon is loosely referred to as decoupling and its effect on the turbulent motion in the boundary layer is schematically represented in the bottom panel of Figure 1.3. In early studies, it was hypothesized that decoupling would lead to a rapid breakup of the stratocumulus layer by diminishing the transport of humidity that evaporates at the sea surface toward the stratocumulus layer (Nicholls, 1984).

As the subcloud layer humidifies, updrafts initiated at the surface become more buoyant, making it possible for them to penetrate into the conditionally stable layer and reach the height at which they saturate. These saturated updrafts form cumulus clouds below the stratocumulus layer (Albrecht et al., 1995). Their role is to transport humidity out of the subcloud layer toward the stratocumulus layer, thereby recoupling the two layers. However, from observations or conceptual models it is difficult to quantify the transport performed by these clouds and to determine how relevant it is for the persistence of the stratocumulus layer (Martin et al., 1995).

1.2.3 Stratocumulus Transitions

Figure 1.3 shows that the air that is transported toward the subtropics through the upper atmosphere flows back toward the equator in the lower part of the atmosphere, forming prevailing winds commonly referred to as the trade winds. These prevailing winds advect the stratocumulus clouds over increasingly warm water, effectively causing the temperature of the sea surface below the stratocumulus cloud to increase. The stratocumulus cloud is typically observed to slowly thin and eventually break up, so that a boundary layer populated by cumulus clouds remains. As cumulus clouds have a much lower cloud cover, the transition from stratocumulus to cumulus results in a large decrease of the area averaged albedo, which makes them important for the radiative budget of the planet. In GCMs, stratocumulus transitions often occur too early on the trajectory from the subtropics to the tropics, which is an important cause for the negative bias of the stratocumulus cloud amount that climate models often suffer from (Teixeira et al., 2011). With respect to the cloud-climate feedback, we would like to know how the changing climate affects stratocumulus transitions. For instance, if climate warming would cause the transition to occur earlier, this would lead to a decrease of stratocumulus in favor of cumulus clouds and hence to a positive cloud-climate feedback.

The thinning and breaking up of stratocumulus clouds during transitions has been mostly attributed to entrainment and to decoupling. The increasing sea surface temperature reduces the temperature contrast between the free tropospheric air and the sea surface. This leads to a weaker inversion and hence to increased entrainment. At the same time, subsidence tends to dry the free troposphere.

These two effects enhance the drying tendency of the stratocumulus layer by entrainment as it is advected toward the equator, eventually leading to its break up. The enhanced entrainment furthermore leads to a more rapid deepening of the boundary layer, causing it to decouple (Wyant et al., 1997). In this thesis, we investigate the role that these processes play in the thinning of stratocumulus clouds during transitions.

1.3 Process Modeling

In a GCM, the atmosphere of the entire planet is represented on a grid that consists of millions of three-dimensional cells. The total number of cells, and thus the resolution of a GCM, is limited by the available computational resources. Currently, the horizontal size of a GCM's grid cell is of the order of 100 km (Taylor et al., 2011) and the grid levels are typically spaced a few hundreds meters apart. Hence, the resolution of a GCM is too coarse to adequately resolve the mixing processes that are crucial to the existence of stratocumulus clouds. In GCMs turbulent transport therefore needs to be represented in a simplified statistical way on the basis of the local mean properties of the air, a practice that is referred to as parameterization.

Even though the available computational power has been increasing at an exponential rate (Schalkwijk et al., 2014), global simulations at fine enough resolution to properly resolve the bulk of the turbulent transport and that last for climatologically relevant timescales will remain unfeasible for the foreseeable future. It is therefore important to understand how parameterizations affect the sign and the magnitude of the stratocumulus cloud-climate feedback in GCMs. This requires a thorough knowledge of the interaction between turbulence, radiation, precipitation and large-scale subsidence in stratocumulus-topped boundary layers. Three different model types are described next that are commonly used to research this interaction.

1.3.1 Mixed-layer Models

Mixed-layer models (MLMs) exploit the well-mixed structure of a stratocumulus-topped boundary layer by treating it as a single reservoir in which conserved variables for humidity and heat are constant with height. The only sources and sinks are due to surface fluxes, entrainment, radiation and precipitation (Lilly, 1968). With these assumptions, the evolution of the temperature and the humidity in the boundary layer can be described with just a few simple equations. Due to this simplicity, the use of MLMs is computationally very cheap and their results are relatively straightforward to interpret. Therefore, they are still being used extensively for the research on stratocumulus clouds (Uchida et al., 2010; Caldwell et al., 2012; Bretherton et al., 2013; De Roode et al., 2014; Jones et al., 2014; Dal Gesso et al., 2014b).

However, the assumption of a well-mixed boundary layer causes MLMs to be of limited use for understanding stratocumulus transitions, during which the boundary layer is decoupled and turbulent transport by cumulus clouds plays an important role. Furthermore, to close the set of MLM equations, the entrainment rate has to be parameterized. Many entrainment parameterizations have been

developed (e.g. Turton and Nicholls, 1987; Lock, 1998; Lewellen and Lewellen, 1998; Moeng, 2000; Lilly, 2002; Stevens, 2002), but due to the complexity of the entrainment process and the lack of accurate observations it is often unclear how well these parameterizations represent the actual entrainment rate.

1.3.2 Large-eddy Simulation

In large-eddy simulation (LES) models, the lower part of the atmosphere is simulated on a fine, three-dimensional grid. As compared to GCMs, the computational power in LESs is concentrated on a limited simulation domain, ranging in size from ten to a few thousand square kilometers (see the left panel of Figure 1.2). The resolution of the numerical grid is fine enough to explicitly represent the energetic part of the turbulence spectrum. The smaller subgrid scales that contribute little to the turbulent transport are filtered out of the numerical solution by applying a low-pass filter on the Navier-Stokes equations that describe the momentum of gases and fluids. The effects of these subgrid scales are subsequently parameterized by the subgrid model. Solving these filtered Navier-Stokes equations reduces the computational cost of the simulations by orders of magnitude as compared to direct numerical simulation methods in which turbulence is resolved down to the smallest length scales.

LES models were first used several decades ago (Lilly, 1962; Deardorff, 1972) and their ability to explicitly simulate the complex interaction between turbulence and clouds has made them the tool of choice for much boundary-layer cloud research today. In contrast to MLMs, LES models are well-suited for the simulation of the process of decoupling. Moreover, the influences of radiation, evaporative cooling and microphysical processes on the turbulence and hence on the entrainment rate are typically well represented by LES models. Through comparison with observations LES models have been shown to be capable of realistically simulating stratocumulus clouds (Caldwell and Bretherton, 2009; Ackerman et al., 2009).

The fine resolution and the three-dimensional domain make LES computationally demanding. Hence, LESs were typically performed on relatively small domains and often lasted only a few hours. For instance, the first LESs of a stratocumulus-topped boundary layer were performed on a numerical domain of 2^3 km^3 consisting of only 40^3 grid cells and each simulation lasted for less than an hour (Deardorff, 1980b). Stratocumulus transitions typically last several days and their LES has therefore been unfeasible for a long time. Moreover, a relatively high resolution is required to properly resolve the structure of the sharp temperature and humidity gradients at the inversion (Stevens et al., 1999).

However, computational resources have been increasing at a very rapid pace, allowing for simulation domains of up to a few hundred kilometers in both horizontal directions (Schalkwijk et al., 2014) as well as for very fine resolutions of only a few meters (Yamaguchi and Randall, 2012). The first LESs of stratocumulus transitions have therefore recently been performed (Sandu and Stevens, 2011). In chapter 2 of this thesis, LES results are presented and compared to measurements gathered during an observed stratocumulus transition, with the purpose of validating the use of LES for the simulation of stratocumulus transitions.

The Dutch Atmospheric LES (DALES) model (Heus et al., 2010; Böing et al.,

Figure 1.4. Three-dimensional visualization of a thin stratocumulus layer with cumulus updrafts appearing below as simulated with the Dutch Atmospheric LES (DALES) model at a resolution of $40 \times 40 \times 10$ m^3. A video of part of the simulation can be found online (https://www.youtube.com/watch?v=vZpyVWye3S4).

2012) was used to perform the simulations in this thesis. Figure 1.4 shows a three-dimensional visualization of the cloud field during a stratocumulus transition as simulated with DALES.

1.3.3 Single-column Models

To determine how well GCMs represent clouds, ideally one would want to directly compare GCMs, in which turbulent transport is parameterized, to LES models that resolve most of this turbulent transport. However, such a comparison is complicated as GCMs are designed to simulate the global climate and cannot easily be configured to run idealized simulations on domain sizes similar to those used by LES models.

Therefore, Single-Column Model (SCM) versions of GCMs have been developed. An SCM consists of just a single column of grid cells and uses the same parameterization schemes as the GCM from which it is derived to represent the vertical turbulent transport as well as other cloud processes. The advantage of an SCM over a GCMs is that the former can be easily run using the same boundary conditions and forcings as MLMs and LES models. Furthermore, SCMs are computationally much cheaper to operate than their GCM counterparts. To evaluate the performance of parameterization schemes, SCMs are therefore often compared to LES results (e.g. Duynkerke et al., 1999; Zhu et al., 2005; Zhang et al., 2010).

1.4 Modeling Strategies

The process models described in the previous section are typically used for two different types of studies. First, the models can be forced using realistic boundary conditions derived from observations. The comparison of the model results with the observations allows for the validation of the model (e.g. Nicholls, 1984; Lenschow et al., 1988; Stevens et al., 2003a; Bretherton et al., 2004; Malinowski et al., 2013). Second, after validation of the model, it can be used to perform reproducible experiments allowing for the systematic study of the sensitivity of clouds to changes in the environmental properties (Uchida et al., 2010; Xiao et al., 2011; Chung et al., 2012). Such sensitivity studies are very difficult to perform on the basis of observations alone. Below, for either modeling approach an example is given that is particularly relevant to this thesis project.

1.4.1 ASTEX

In June 1992, the Atlantic Stratocumulus Transition EXperiment (ASTEX, Albrecht et al., 1995) was performed. The main goal of ASTEX was to gather observations at different stages of a stratocumulus transition. To this end, a stratocumulus-topped boundary layer was followed as it was advected toward the equator and five aircraft flights were undertaken at different moments during the observed transition. The campaign was a great success and the data gathered during ASTEX has been analyzed in many subsequent studies (e.g. Bretherton and Pincus, 1995; Bretherton et al., 1995; Wang and Lenschow, 1995; De Roode and Duynkerke, 1996).

Despite the wealth of data that was gathered as part of the experiment, the role of decoupling and of cumulus clouds during the transition remained uncertain (Martin et al., 1995). Several attempts to model the stratocumulus transition with one- and two-dimensional turbulence models were made, to help interpret the observational data (Krueger et al., 1995; Bretherton et al., 1999a; Svensson et al., 2000). As the LES of the entire ASTEX transition was computationally not feasible at the time, shorter LES studies were performed on the basis of the second (Duynkerke et al., 1999) and the third flight of the ASTEX campaign. In chapter 2, LES results for the complete transition are presented and compared to the measurements.

1.4.2 CGILS

Motivated by the large spread that was found among GCMs in the magnitude of the cloud-climate feedback, the main objective of the CGILS[1] project was to determine on a process level how marine cloud-topped boundary layers respond to climate change (Zhang et al., 2013).

In CGILS, three cases were designed ranging from shallow, relatively well-mixed stratocumulus (S12) and decoupled cumulus-under-stratocumulus (S11) to trade cumulus (S6) (Blossey et al., 2013). Furthermore, the large-scale conditions that

[1] Cloud Feedback Model Intercomparison Project (CFMIP)/Global Atmospheric System Study (GASS) Intercomparison of Large-Eddy and Single-Column Models

correspond to a future warmer climate were derived from GCM results. Through comparison of the results of the control simulations to those obtained with the perturbed large-scale conditions, the stratocumulus cloud-climate feedback can be diagnosed. The forcings in the CGILS experiment were kept constant in time and diurnally average insolation was prescribed so that an approximate steady state was reached at the end of the ten-day simulations. This ensured robust cloud responses from the comparison of the perturbed climate to the control simulations.

The results of the five models that participated in the intercomparison study indicated that stratocumulus clouds tend to thin as a result of a 2 K warming at constant initial relative humidity (Blossey et al., 2013). In contrast, the response of the SCMs to this perturbation ranged from a significant thickening to strong thinning for the stratocumulus and the cumulus-under-stratocumulus cases (Zhang et al., 2013), which possibly reflects the large spread of the cloud-climate feedback among GCMs. At the moment of writing, the results of the second phase of CGILS are being prepared for publication (Blossey et al., 2015). For this study, the response of the different cloud regimes to an increase of the CO_2 concentration is among others investigated.

1.5 Context and Research Aims

The research presented in this thesis has been performed as part of the EUCLIPSE[2] project that was initiated at the beginning of 2010. A total number of twelve institutes throughout Europe collaborated within this project with the common goal of decreasing the uncertainty in future climate projections, specifically those uncertainties due to the representation of cloud processes.

The project was divided into four work packages. The objective of the first work package (WP1) was to perform simulations of several climate change scenarios with the current generation of GCMs. These scenarios were designed to help disentangling the many feedback processes that the climate system is rich. WP2 was responsible for the analysis of this data in order to determine what the main sources of disagreement among the GCMs are. In parallel with WP2, systematic studies were performed as part of WP3 that focused on understanding the cloud controlling parameters on a process level. Moreover, the performance of SCM versions of GCMs was validated against in situ observations and LES results. The last work package, WP4, was responsible for the design of new experiments and the implementation and improvement of parameterization schemes, which should eventually lead to a decrease of the intermodel spread.

The research presented in this thesis is part of WP3. The following questions are addressed:

- How suitable are current LES models for the simulation of stratocumulus transitions? This question is treated in two steps. First, can LES models faithfully represent observed stratocumulus transitions? Second, how large is the spread among different LES models for a specific transition case and what processes are responsible for this spread?

[2]European Union CLoud Intercomparison, Process Study and Evaluation; http://www.euclipse.eu/

- What physical mechanisms or large-scale conditions are responsible for the thinning and breaking up of stratocumulus clouds during stratocumulus transitions?
- How do stratocumulus-topped boundary layers respond to changes in the large-scale conditions that are related to future climate change?

1.6 Outline

The thesis is divided into the following chapters.

Chapter 2 describes the setup of the Global Atmospheric System Study (GASS)-EUCLIPSE stratocumulus transition case based on the observed ASTEX transition. The results of six LES models are presented and evaluated against the available in situ observations. The simulations provide a continuous set of high-resolution data on the turbulence structure of the boundary layer. These data allow for the evaluation of for instance the effect of decoupling on the transport of humidity by shallow cumulus clouds from the subcloud layer to the stratocumulus cloud. Additionally, several sensitivity experiments were performed using DALES, in which the prescribed cloud droplet number density was varied to identify the effects of differences in the microphysics parameterization schemes.

In chapter 3 a budget equation is derived that describes the tendency of the stratocumulus liquid water path (LWP) following Randall (1984). From this equation, the individual contributions of all relevant physical processes (entrainment, radiation, precipitation, turbulent transport at cloud base and subsidence) to the LWP tendency can be studied. The main focus of the chapter is the influence of the thermodynamic properties of the free tropospheric air on the thinning of the stratocumulus layer. The rapid thinning of stratocumulus clouds has often been attributed to an entrainment feedback process (Randall, 1980; Deardorff, 1980a). Chapter 3 offers an alternative explanation to this dependency of the stratocumulus cloud thickness on the free tropospheric thermodynamic conditions.

In chapter 4, the influence of the free troposphere on stratocumulus-topped boundary layers is further investigated. To this end, a set of LESs is performed in which the free tropospheric humidity and temperature are systematically varied. The setup of the simulations was provided by Dal Gesso et al. (2014b), who developed the framework as an extension of the CGILS cumulus-under-stratocumulus case (Blossey et al., 2013) and who performed the simulations with an MLM and later with an SCM (Dal Gesso et al., 2014a). The LES study of chapter 4 complements these studies. Each of the simulations is initialized with a thick layer of stratocumulus and is run for ten days to an approximate steady state. To investigate the response of the stratocumulus layers to an idealized climate perturbation, another set of simulations was performed for which the initial temperature was increased by 2 K, while the initial relative humidity profile was kept constant.

It has been found that the Hadley circulation will weaken in a future climate (Held and Soden, 2006; Soden and Held, 2006), resulting in weakening of the large-scale subsidence in the stratocumulus regimes. In chapter 5 we researched how such a weakening affects the timing of the breakup of the stratocumulus layer. Several LESs are performed that show that a weakening of the subsidence velocity

delays the moment of break up of the stratocumulus cloud, thereby corroborating earlier results by Svensson et al. (2000) and Sandu and Stevens (2011). The theory developed in chapter 3 is used to investigate which of the physical processes are responsible for this delay.

Appendix A describes the origin of a numerical problem that caused unphysical behavior close to the sharp temperature and humidity inversion at the top of the boundary layer. A detailed description is given of the numerical advection scheme that was included in DALES as part of this thesis project to avoid this problem.

As chapters 2-5 have been, or are intended to be, published individually in scientific journals, some redundancy is unavoidable. Each chapter can be read separately and contains detailed conclusions. A synthesis of the main conclusions and an outlook on further research is given in chapter 6.

2

The GASS/EUCLIPSE Model Intercomparison of the Stratocumulus Transition as Observed During ASTEX: LES Results

Large-eddy simulations of a Lagrangian transition from a vertically well-mixed stratocumulus-topped boundary layer to a situation in which shallow cumuli penetrate an overlying layer of thin and broken stratocumulus are compared with aircraft observations collected during the Atlantic Stratocumulus Transition EXperiment (ASTEX). Despite the complexity of the case and the long simulation period of 40 hours, the six participating state-of-the-art models skilfully and consistently represent the observed gradual deepening of the boundary layer, a negative buoyancy flux at the top of the subcloud layer and the development of a double-peaked vertical velocity variance profile. The moisture flux from the subcloud to the stratocumulus cloud layer by cumulus convection exhibits a distinct diurnal cycle. During the night the moisture flux at the stratocumulus cloud base exceeds the surface evaporation flux, causing a net drying of the subcloud layer, and vice versa during daytime. The spread in the liquid water path (LWP) among the models is rather large during the first 12 hours. From additional sensitivity experiments it is demonstrated that this spread is mainly attributable to differences in the parameterized precipitation rate. The LWP differences are limited through a feedback mechanism in which enhanced drizzle fluxes result in lower entrainment rates and subsequently a reduced drying at cloud top. The spread is furthermore reduced during the day as cloud layers with a greater LWP absorb more solar radiation and hence evaporate more.

Published in *J. Adv. Model. Earth Syst.* (2013), with S.R. de Roode, A.S. Ackerman, P.N. Blossey, C.S. Bretherton, M.J. Kurowski, A.P. Lock, R.A.J. Neggers, I. Sandu and A.P. Siebesma.

2.1 Introduction

Large portions of the Earth's oceans are covered by fields of stratocumulus clouds (Wood, 2012). As these clouds are advected from the subtropics toward the equator by the trade winds, they are gradually replaced by shallow cumulus clouds. Because these cumuli have a much lower area coverage, the radiative forcing of the two cloud types is very different. Stratocumulus to cumulus transitions are therefore key to the subtropical energy balance, making it crucial for numerical weather prediction and global climate models to accurately capture them. Teixeira et al. (2011) however show that these transitions often occur too early as compared with observations, which partly causes the underestimation of the subtropical low cloud amount many such models suffer from.

The first studies on stratocumulus cloud transitions were performed with one- or two-dimensional turbulence models (e.g. Krueger et al., 1995; Bretherton and Wyant, 1997; Wyant et al., 1997; Bretherton et al., 1999a; Svensson et al., 2000). Owing to the continuous advance in the amount of available computational power, three-dimensional large-eddy simulation (LES) modeling on a sufficiently large domain and for sufficiently long time periods has now become feasible as is demonstrated by Sandu and Stevens (2011). Their results show that LES models are well capable of representing a smooth transition between the two cloud regimes. However, because the cases were based on composites of satellite observations and reanalysis data (Sandu et al., 2010), features like the evolution of the mean state and turbulence structure of the boundary layer could not be critically compared with changed in situ observations.

Another approach to determine what processes cause the stratocumulus to cumulus transition is to perform idealized simulations toward an equilibrium state (Zhang et al., 2010). Using this methodology Chung et al. (2012) found that the steady-state inversion height increases as the sea surface temperature (SST) is increased. The boundary layer structure furthermore changes from relatively well-mixed to decoupled with cumulus clouds developing underneath a thin stratocumulus layer. The stratocumulus cloud layer eventually vanishes at sufficiently high SSTs. On the basis of Lagrangian LES experiments Sandu and Stevens (2011) also concluded that the SST is the main factor explaining the stratocumulus transition. Klein and Hartmann (1993) furthermore showed that the seasonally averaged cloud fraction typically increases with lower tropospheric stability, which is a measure of vertical stability and is defined as the potential temperature difference between the 700 hPa level and the surface.

During the first Lagrangian of the Atlantic Stratocumulus Transition EXperiment (ASTEX), aircraft observations of a transition from a solid stratocumulus-topped boundary layer to a boundary layer dominated by shallow cumulus clouds penetrating a thin veil of broken stratocumulus were collected (Albrecht et al., 1995; Bretherton and Pincus, 1995; Bretherton et al., 1995; De Roode and Duynkerke, 1997). These observations were used by Bretherton et al. (1999a) to set up a model intercomparison case in order to study the representation of the entire transition with single-column model (SCM) versions of numerical weather prediction and climate models as well as with two-dimensional turbulence models. All models were shown to be able to predict the deepening and decoupling of the boundary

layer and the appearance of cumuli below the stratocumulus clouds. However, significant quantitative differences were found in the liquid water path and cloud cover that were ascribed to the parameterizations of radiation, microphysics and subgrid scale turbulence.

Two model intercomparison studies for both SCM and LES models were set up on the basis of the second (A209) and the third flight (RF06) (Duynkerke et al., 1999; Chlond and Wolkau, 2000) of the ASTEX first Lagrangian as part of the GEWEX Cloud System Study (GCSS) project. Due to the limited computational resources, the LES runs lasted just three hours and used a rather coarse vertical grid resolution. The results suggested that the entrainment rate in the LES models was on average about 50 % greater than the values derived from the aircraft observations. However, the entrainment rate was shown to decrease if cloud microphysics was included or if the vertical resolution was increased.

In this paper, some slight modifications to the ASTEX first Lagrangian model intercomparison case proposed by Bretherton et al. (1999a) are described and the simulation results of six state-of-the-art LES models are presented. These models each include detailed parameterization schemes for radiation and microphysics. The aim is to assess how well LES models are capable of representing stratocumulus transitions by making a detailed comparison with the observations. Together with the three stratocumulus transition cases designed by Sandu and Stevens (2011), this case was run as a joint Global Atmospheric System Study (GASS) and European Union CLoud Intercomparison, Process Study and Evaluation (EUCLIPSE) project effort. De Roode et al. (2012) presents the preliminary LES results of all four cases and discusses the development of stratocumulus transitions under different forcing conditions. The simulation results of the SCM versions of numerical weather prediction and climate models will be presented and compared with the LES results in a separate paper.

The setup of the paper is as follows. Section 2.2 presents the initialization of the case, the boundary conditions and the large-scale forcings as well as numerical aspects such as resolution and domain size. The results submitted by the participating modelers are compared with the observations in Section 2.3. In Section 2.4 the humidity budget is analyzed with particular attention to drizzle and surface latent heat fluxes. The last section contains a summary of the main conclusions and some discussion.

2.2 Setup

2.2.1 Initial Conditions

The initial vertical profiles are taken from the GCSS model intercomparison case based on flight 2 of the ASTEX first Lagrangian, which was set up by Peter Duynkerke. These profiles are given by

$$\varphi(z) = \begin{cases} \varphi_{\mathrm{ml}} & z \le z_{\mathrm{i}} \\ \varphi_{\mathrm{ml}} + \Delta\varphi(z - z_{\mathrm{i}})/\Delta z & z_{\mathrm{i}} < z \le z_{\mathrm{i}} + \Delta z \\ \varphi_{\mathrm{ml}} + \Delta\varphi - & \\ \quad \Gamma_{\varphi}(z - z_{\mathrm{i}} - \Delta z) & z_{\mathrm{i}} + \Delta z < z \le 2\,\mathrm{km} \end{cases} \tag{2.1}$$

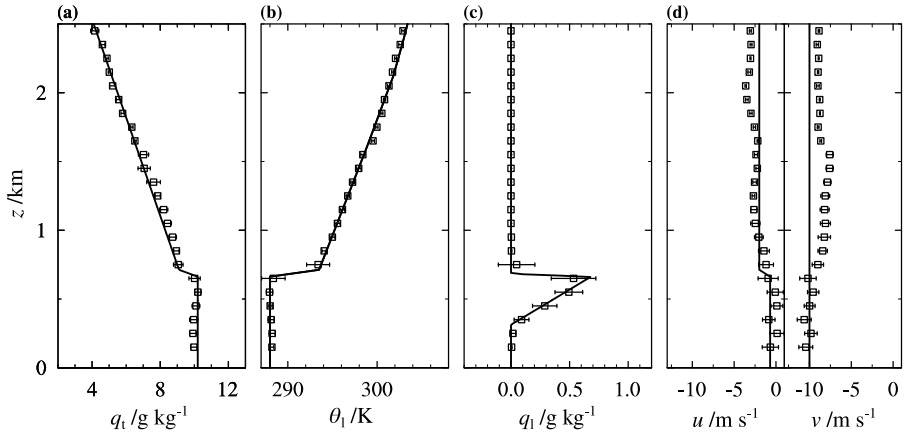

Figure 2.1. Initial profiles of total humidity q_t (a), liquid water potential temperature θ_l (b), liquid water specific humidity q_l (c) and horizontal wind components u (east-west) and v (south-north) (d). Squares denote observations gathered during flight 2 of the First Lagrangian, bin-averaged over height intervals of 100 m. Error bars show the $\pm$ one standard deviation range.

where $\varphi \in \{q_t, \theta_l, u, v\}$ are the total specific humidity, the liquid water potential temperature and the wind components in east-west and south-north directions respectively. Initial values of the mixed layer variables φ_{ml}, the inversion jumps $\Delta\varphi$ and the free atmospheric lapse rates Γ_φ for each of these variables are given in Table 2.1. The inversion layer initially has a thickness of $\Delta z = 50$ m and its base is at a height $z_i = 662.5$ m. The initial profile for the pressure is constructed by assuming hydrostatic equilibrium, with a surface pressure $p_s = 1029.0$ hPa that is constant in time. The motivation for choosing the second flight of the ASTEX first Lagrangian is that the boundary layer was vertically well-mixed and horizontally homogeneous, making it a more suitable starting point than the first flight during which the boundary layer structure was inhomogeneous with occasional small cumuli and fog (De Roode and Duynkerke, 1997). The simulations start 13 June 1992 at 0000 UTC and last 40 h, approximately corresponding to the time between ASTEX measurement flights 2 and 5.

Table 2.1. Values of the parameters used in Eq. (2.1) to describe the initial profiles of the relevant variables.

φ	φ_{ml}	$\Delta\varphi$	Γ_φ (km^{-1})
q_t (g kg^{-1})	10.2	-1.1	2.8
θ_l (K)	288.0	5.5	-6.0
u (m s^{-1})	-0.7	-1.3	0.0
v (m s^{-1})	-10.0	0.0	0.0

The initial vertical profiles defined by Eq. (2.1) are shown in Figure 2.1 together

with the observations from which the profiles were originally derived. Above 2 km, the profiles are determined from ERA-Interim reanalysis data as described in Section 2.2.2. Note that all the necessary model input data presented in this section can be downloaded from the EUCLIPSE project website[1].

2.2.2 Model Forcings

The ASTEX observations were performed following a Lagrangian strategy during which a column of air was followed as it was advected toward the equator. An advantage of this approach is that the effect of horizontal advection on the budgets of heat and moisture can be neglected, provided that the vertical shear of horizontal winds is negligibly small. Time-varying forcings and boundary conditions are prescribed to account for changing conditions along the Lagrangian trajectory. They differ slightly from the forcing prescribed by Bretherton et al. (1999a). For example, a relaxation towards the observed mean winds is not required in the current setup.

Sea surface temperature

The SST time series as compiled by Bretherton et al. (1995, Figure 1a) is used for the simulations, which contains reanalysis data supplied by the ECMWF and measurements from two aircraft and a ship. These data give a relatively fast SST increase of about 4 K over the 40-hour simulation period. In contrast to the GCSS model intercomparison cases based on flights 2 and 3 that used prescribed surface fluxes, the surface fluxes are here computed from the prescribed SST.

Geostrophic wind

Figure 2.2a shows that the mean wind velocity in both the boundary layer and the free atmosphere changed from a mainly north to a north-east direction during the transition. We estimated the temporal variation of the geostrophic wind velocity using the observed wind components in the free atmosphere and their respective budget equations,

$$\frac{\partial u_{\mathrm{fa}}}{\partial t} = \quad f(v_{\mathrm{fa}} - v_{\mathrm{g}}), \tag{2.2a}$$

$$\frac{\partial v_{\mathrm{fa}}}{\partial t} = -f(u_{\mathrm{fa}} - u_{\mathrm{g}}). \tag{2.2b}$$

Here, the subscript "fa" indicates free atmospheric values, f is the Coriolis parameter and u_{g} and v_{g} are the horizontal components of the geostrophic wind. Figure 2.2a shows the estimated geostrophic wind components, which are assumed to be constant with height. It can also be noticed from this figure that the horizontal winds in the free atmosphere will be correctly predicted if this prescribed geostrophic forcing is used in a time integration of Eqs. (2.2). The prescribed geostrophic forcing will furthermore enforce a weakening of the total horizontal boundary layer wind speed, which was observed to decrease from 10 to approximately 4 m s^{-1} during the Lagrangian. Note that Figure 2.2a also indicates that the

[1] www.euclipse.nl/wp3/ASTEX_Lagrangian/LES_astex_setup.shtml

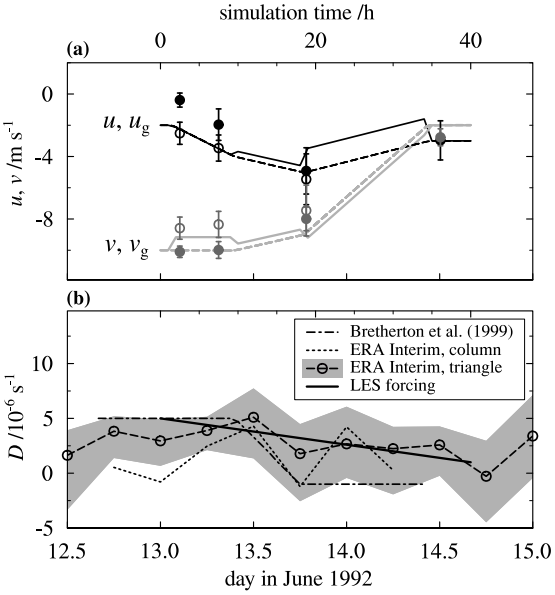

Figure 2.2. Figure (a) shows the geostrophic wind (solid lines) and the expected free atmospheric horizontal wind components calculated using Eqs. (2.2) (dashed) as a function of time. The filled and the open circles respectively indicate the observed boundary layer and free atmospheric velocities. Figure (b) shows the boundary layer averaged large scale divergence of the horizontal winds D as derived from ERA-40 data by Bretherton et al. (1999a) (dash-dotted). The dotted line was obtained by taking a weighted area and a boundary layer average of D from ERA-Interim data along the trajectory as reported by Bretherton and Pincus (1995). The dashed line represents the boundary layer averaged D, averaged over the ASTEX triangle (Albrecht et al., 1995). The area between the 20th and the 80th percentile has been shaded in grey. The large scale divergence that was used for the simulations is indicated by the solid black line.

observed wind shear across the inversion is generally less than $2\,\mathrm{m\,s^{-1}}$, suggesting that the influence of horizontal advection of q_t and θ_l into the Lagrangian column is small. The variation of the horizontal wind with time needs to be accounted for in the model simulations as it controls the magnitude of the surface fluxes of momentum, heat and moisture. These surface fluxes were all calculated using a fixed surface roughness length $z_0 = 2 \times 10^{-4}\,\mathrm{m}$.

Large-scale divergence

The GCSS model intercomparison cases based on flights 2 and 3 prescribed a large-scale divergence rate D of $5 \times 10^{-6}\,\mathrm{s^{-1}}$ and $15 \times 10^{-6}\,\mathrm{s^{-1}}$, respectively. These values were chosen on the basis of an assumed balance between the large-scale subsidence and the entrainment rate in order to yield an approximate steady-state boundary layer height in the LESs. These prescribed values for D are likely too large because the used LES models were run with a rather coarse vertical resolution

and did not include cloud droplet sedimentation, and thus gave unrealistically large entrainment rates. For the ASTEX model intercomparison study by Bretherton et al. (1999a), a time-varying value for D was applied based on measurements and ECMWF reanalysis data (see Figure 2.2b). LES runs performed by De Roode and Van der Dussen (2010) showed that with these values for D the boundary layer depth is overestimated by almost 1 km as compared to the observations at the end of the 40-hour simulation.

Ciesielski et al. (1999) used soundings of the horizontal winds to calculate D and the large-scale subsidence for the period 1-15 June 1992. Their results show only a slight and gradual decrease of D during the first Lagrangian, resulting in an average value of about $4 \times 10^{-6}\,\mathrm{s}^{-1}$. This finding is in line with the conclusion of Sigg and Svensson (2004), who state that there is no evidence for a strong decrease in D as suggested by Bretherton and Pincus (1995). Figure 2.2b shows D as diagnosed from ERA-Interim data. The spatial and temporal variation in the data is large, as is the case with ERA-40 data (Duynkerke et al., 1999). The value for D as averaged over the boundary layer column and at the actual position during the Lagrangian therefore fluctuates between about 5×10^{-6} and $-1 \times 10^{-6}\,\mathrm{s}^{-1}$. Ciesielski et al. (2001) found a diurnal signal in D with an amplitude of up to $2 \times 10^{-6}\,\mathrm{s}^{-1}$ and a similar diurnal cycle was proposed in other studies (e.g. Bretherton et al., 2004). Due to the low temporal resolution a diurnal cycle cannot be discerned in the ERA-Interim data. When D is averaged over the ASTEX triangle the signal fluctuates less and decreases slightly during the period of the First Lagrangian. On the basis of these studies a simple function for D is prescribed that decreases linearly with time from a value of 5×10^{-6} to $1 \times 10^{-6}\,\mathrm{s}^{-1}$. Following Bretherton et al. (1999a), $D = 0$ above 1600 m such that the subsidence is constant above this height. This forcing produces q_t and θ_l tendencies in the free atmosphere that are close to those observed.

Radiation

Radiative transfer codes are used to provide accurate temperature tendencies due to longwave and shortwave radiation in the LES domain. The required background profiles of humidity, temperature and ozone needed in these schemes were obtained from ERA-Interim reanalysis data. These profiles are kept constant in time. The precise amount of cirrus clouds that was present at the end of the Lagrangian (Ciesielski et al., 1999) cannot be quantified from the field observations and is therefore neglected for simplicity.

An important factor for the calculation of both radiative and microphysical effects on the cloud layer is the size of the cloud droplets. The cloud droplet number density N_c is assumed to be constant at $100\,\mathrm{cm}^{-3}$ (Bretherton et al., 1995) wherever liquid water is present. A log-normal cloud droplet size distribution is assumed, resulting in a correction factor for the calculation of the effective radius r_e that is a function of the geometric standard deviation σ_g. Using $\sigma_\mathrm{g} = 1.2$,

$$r_\mathrm{e} = r_V \exp\left[\ln(\sigma_\mathrm{g})^2\right] \approx 1.03\, r_V, \tag{2.3}$$

Table 2.2. List of the participating modelers and the used models including parameterization schemes.

Modeler	Model	Model description	Microphysics	Radiation	Advection
A. Ackerman	DHARMA	Stevens et al. (2002)	Morrison et al. (2005)	Toon et al. (1989)	Stevens and Bretherton (1996)
P. Blossey	SAM 6.8.2	Khairoutdinov and Randall (2003)	Khairoutdinov and Kogan (2000)	Mlawer et al. (1997, RRTMG)	Smolarkiewicz and Grabowski (1990)
M. Kurowski	EULAG	Prusa et al. (2008)	Khairoutdinov and Kogan (2000, single moment)	Briegleb (1992)	Smolarkiewicz (2006)
A. Lock	MOLEM	Shutts and Gray (1994); Abel and Shipway (2007)	Abel and Shipway (2007)	Edwards and Slingo (1996)	Yamaguchi et al. (2011)
I. Sandu	UCLA LES	Stevens and Seifert (2008)	Seifert and Beheng (2001)	Fu and Liou (1993); Pincus and Stevens (2009)	Stevens et al. (2005b)
J. van der Dussen	DALES 3.2	Heus et al. (2010)	Khairoutdinov and Kogan (2000)	Fu and Liou (1993); Pincus and Stevens (2009)	Blossey and Durran (2008)

in which r_V is the mean volume radius of the droplets,

$$r_V = \left(\frac{3\rho q_\mathrm{l}}{4\pi\rho_\mathrm{w} N_\mathrm{c}} \right)^{1/3}. \tag{2.4}$$

Here, ρ and ρ_w are the densities of respectively moist air and liquid water and q_l is the liquid water specific humidity. The value of 1.03 in Eq. (2.3) is in good agreement with observational findings by Pawlowska and Brenguier (2000).

The sea surface albedo α_s is a function of μ, the cosine of the solar zenith angle, and is approximated by (Briegleb, 1992):

$$\begin{aligned} \alpha_\mathrm{s} = & \frac{0.026}{\mu^{1.7} + 0.065} + \\ & 0.15(\mu - 0.10)(\mu - 0.50)(\mu - 1.00). \end{aligned} \tag{2.5}$$

2.2.3 Numerical and Model Details

References to the descriptions of the six participating LES models can be found in Table 2.2. Following Sandu and Stevens (2011), the LES runs were performed using a horizontal domain size of 4480^2 m^2 consisting of 128 grid points with a resolution of 35 m in each horizontal direction. In the z-direction a varying vertical grid resolution was used, ranging from 15 m at the surface to 5 m in the cloud layer and at the inversion. The base of the sponge layer is located at approximately 2400 m and above this height the vertical grid distance is stretched with increments of 10 % per level. Although it is recognized that the horizontal domain size is rather small, Sandu and Stevens (2011) showed that for simulations of cases with little precipitation a larger horizontal domain size of 8960^2 m^2 hardly affected the LES results.

The domain is translated with a constant velocity of $-2\,\mathrm{m\,s^{-1}}$ in the x- and $-7\,\mathrm{m\,s^{-1}}$ in the y-direction. These velocities are chosen as optimal values for computational efficiency.

All modelers were asked to provide the same output data as in the RICO (Rain in Cumulus over the Ocean) model intercomparison (vanZanten et al., 2011).

2.3 Model Results and Observations

2.3.1 Timeseries

The three snapshots of the cloud fields as obtained from the Dutch Atmospheric LES (DALES) model presented in Figure 2.3 show a clear evolution of the stratocumulus transition. As the boundary layer gradually deepens, shallow cumulus clouds develop which penetrate the stratocumulus cloud layer above. The onset of the breakup of the thinning stratocumulus is marked by the appearance of clear air patches at the top of the cloud layer.

The domain averaged cloud cover σ presented in the upper panel of Figure 2.4 shows that only at the end of the simulation does the stratocumulus layer start to break up. All models except DHARMA agree well on the timing of breakup.

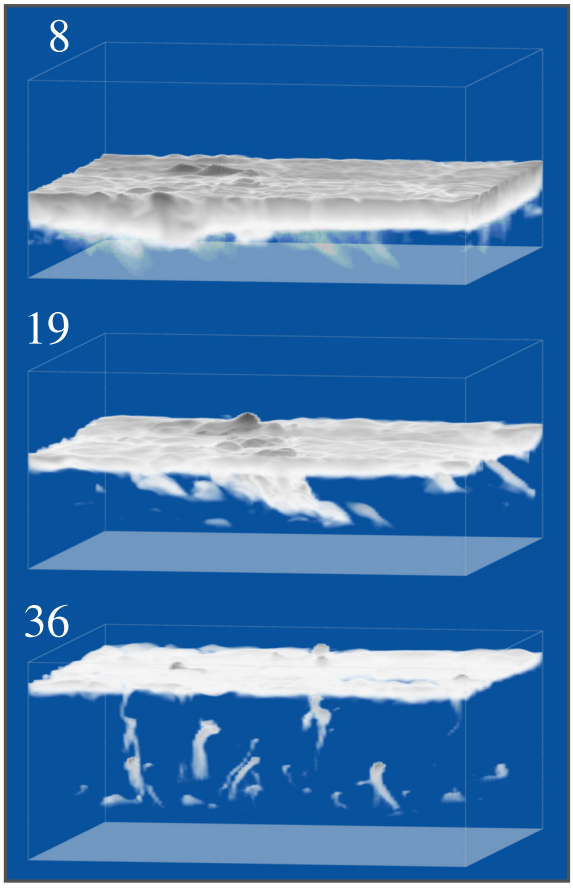

Figure 2.3. Snapshots of the condensed water (including rain) at hours 8, 19 and 36 as simulated using DALES. High q_l values have a darker shade. The white plane indicates the surface. The total height of the box is 2 km.

The bottom panel of the figure shows the development of the cloud boundaries. In particular, the set of upper lines represents the inversion height z_i, which is typically located just above the stratocumulus cloud top. The middle set of lines depict the domain averaged cloud base height z_b. As the cumulus cloud fraction is very small, the value of z_b is dominated by the stratocumulus cloud base height. The lowest set shows the minimum cloud base height $z_{b,min}$, which represents the lowest cumulus cloud base height. The stratocumulus cloud base height gradually increases with time, whereas the cumulus cloud base is almost constant. The increasing difference between z_b and $z_{b,min}$ is indicative of the development of a decoupled boundary layer structure, in which cumulus clouds supply the stratocumulus cloud layer with heat and moisture from the subcloud layer. The general picture of the transition is consistent in the models. Differences in the minimum (cumulus) cloud base height are negligible, while the spread in the modeled inversion height and average cloud

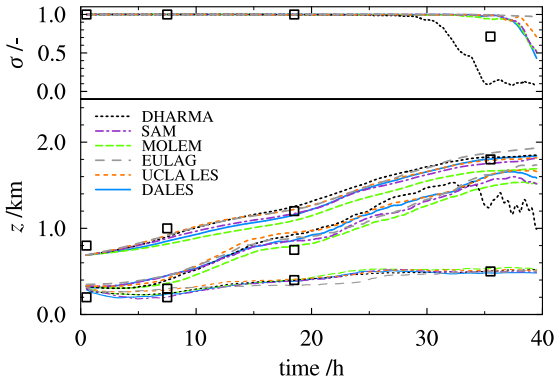

Figure 2.4. The total cloud cover (top) and the contours of the simulated clouds (bottom) composed of the inversion height z_i as an indication of the mean stratocumulus cloud top, minimum cloud base height $z_{\mathrm{b,min}}$ and mean cloud base height z_b for each of the models shown in the legend. The squares denote similar quantities estimated from the profiles of q_l shown in Figure 2.7.

base height is of the order of 200 m. This is about 20 % of the total inversion height increase over the course of the transition.

Figure 2.5a shows the entrainment rate w_e as a function of time. Estimates made on the basis of observations (De Roode and Duynkerke, 1997) are included as a reference. The diurnal cycle is clearly visible in this plot, with significantly more entrainment during the night as compared to the daytime.

Overall, there is better agreement between the simulated entrainment rates than the simulated LWPs, as has been seen in past LES intercomparison studies for stratocumulus clouds (Stevens et al., 2005b; Ackerman et al., 2009). The relatively good agreement in entrainment rate has been explained in the past as a consequence of the heat budget of the boundary layer, which is dominated by radiative cooling, counterbalanced by heat storage needed to keep the layer warming at a rate similar to the SST, and entrainment warming. Since the other two dominant terms are similar between models, and the inversion potential temperature jump is also similar between models, this argument implies the entrainment rate will be similar between models. However, due to differences in transport and subgrid scale turbulence, different models require stratocumulus cloud layers of different thickness to maintain a given entrainment rate, hence LWP can vary more substantially between models (e.g., Zhu et al., 2005).

One other term that can be important to the heat budget (and hence entrainment rate) is net latent heating due to surface precipitation. It will be argued in Section 2.4.3 that microphysical processes are the major cause of the significant intermodel spread in the entrainment rate that is present during the initial 10 hours.

The inclusion of precipitation is also an important cause of the decreased entrainment rate as compared to the GCSS model intercomparison study based on ASTEX flight 3 (hour 8), in which microphysical processes were not taken into account (Duynkerke et al., 1999). The reported average entrainment rate of about

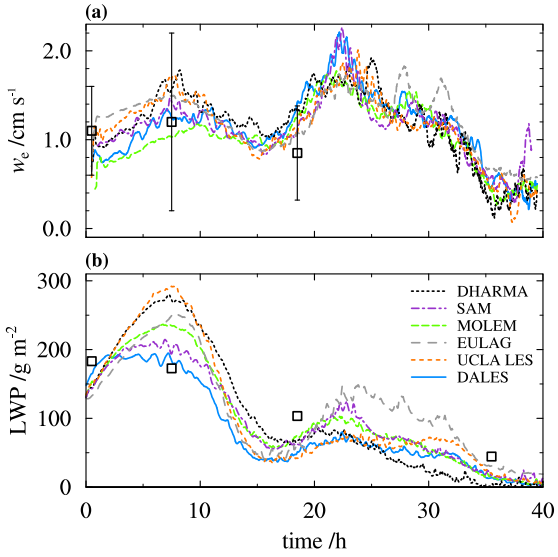

Figure 2.5. The entrainment rate w_e (a) and the liquid water path LWP (b) as a function of time for the models indicated in the legend. Estimates based on observations of w_e including uncertainties were obtained from De Roode and Duynkerke (1997), while the values of the LWP where obtained by integrating the mean q_l profiles shown in Figure 2.7. A running averaging filter with a width of one hour has been applied on the simulated entrainment rates.

1.9 cm s^{-1} for those simulations was recognized to be high compared to the observed value of about 1.2 cm s^{-1}. The average entrainment rate presented here is, at about 1.4 cm s^{-1}, much better in line with the observations. Another contribution to this decrease of the entrainment rate comes from the use of interactive radiation schemes. These schemes produce a slight warming at cloud base that was not accounted for by the idealized longwave radiation parameterization schemes in the previous model intercomparisons. A final cause for the decrease is the higher vertical resolution of 5 m as compared to the 25 m resolution used by Duynkerke et al. (1999). Yamaguchi and Randall (2012) showed that stratocumulus simulations benefit from even higher resolutions. The current resolution however, which is necessary to properly resolve the large gradient in the inversion layer, already limits the maximum time-step of integration to less than 1 s. Using an even higher resolution in combination with the 40 h duration would make the simulation of the entire transition computationally too demanding. Based on the results of Yamaguchi and Randall (2012), the expected error in the entrainment rate due to the limited resolution is of the order of several percent. The deepening rate of the boundary layer, which is governed by the entrainment and the prescribed large-scale subsidence, is in a good agreement with the observations.

Figure 2.5b shows the liquid water path LWP, which is defined as:

$$\mathrm{LWP} = \int_0^\infty \rho q_l \mathrm{d}z. \tag{2.6}$$

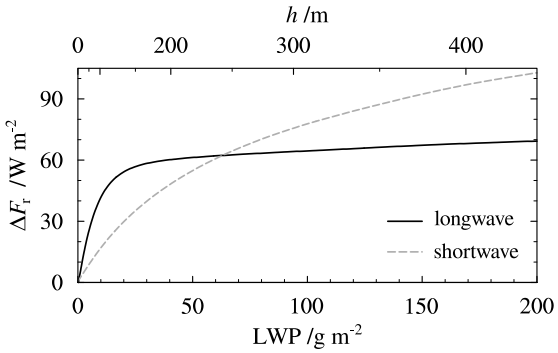

Figure 2.6. The difference in total longwave as well as shortwave radiative flux between the top and the base of an adiabatic stratocumulus cloud layer as a function of LWP (bottom axis) and of cloud thickness h (top axis). The radiative transfer code based on Fu and Liou (1993) that is used in DALES and UCLA LES was used to perform the calculations. By varying the total humidity in the mixed layer, $q_{\mathrm{t,ml}}$ in Eq. (2.1), different values for the liquid water path were obtained. The solar radiation fluxes were calculated at local noon and a cloud droplet number density of $N_{\mathrm{c}} = 100\,\mathrm{cm}^{-3}$ was used.

Note that q_{l} includes rain water. Estimates derived from the measured average liquid water specific humidity profiles are indicated by squares. The models show a steady or even increasing LWP during the first night, despite the boundary layer decoupling evident in Figure 2.4. Approximately eight hours after the start of the simulation the sun rises and the LWP decreases to a local minimum approximately two to three hours after local noon. It is also evident that the large spread in the modeled LWP of over $100\,\mathrm{g\,m}^{-2}$ found during the first night is reduced significantly during daytime. An important reason explaining this LWP convergence is the fact that thicker clouds tend to absorb more solar radiation. This effect is illustrated in Figure 2.6, which shows the difference in both the total shortwave and longwave radiative fluxes between cloud top and cloud base as a function of LWP for an idealized vertically well-mixed stratocumulus layer with a cloud droplet number density $N_{\mathrm{c}} = 100\,\mathrm{cm}^{-3}$. During daytime, stratocumulus clouds with a higher LWP will absorb more solar radiation causing a stronger cloud thinning tendency.

Figure 2.6 also shows that for LWP $> 25\,\mathrm{g\,m}^{-2}$ the total longwave radiative flux divergence across the cloud layer becomes almost independent of LWP. For smaller LWP values the cloud layer becomes optically thin yielding a reduction in the emission as well as the absorption of longwave radiation. As an elevated source of negative buoyancy, longwave radiative cooling at the stratocumulus cloud top drives the vertical mixing. We notice from the DHARMA simulation results that after the LWP drops below $25\,\mathrm{g\,m}^{-2}$ around hour 30, the cloud cover quickly reduces to about 5 to 10 %. This indicates that the decrease of longwave radiative cooling in combination with continued entrainment causes the stratocumulus layer to dissolve and break up. It furthermore shows that in this case the moisture input from the subcloud layer by cumuli is insufficient to maintain the cloud layer.

Table 2.3. Summary of the flight details (for more information, see De Roode and Duynkerke, 1997, Table 1).

Number	Code	UTC time (date)	Simulation time
1	RF05	1719-2133 (12 June)	-
2	A209	0032-0426 (13 June)	Initialization
3	RF06	0451-1013 (13 June)	8th hour average
4	RF07	1627-2109 (13 June)	19th hour average
5	A210	1111-1302 (14 June)	36th hour average

2.3.2 Mean State Vertical Profiles

Hourly-averaged LES results at selected times are next compared with observations gathered during flights 2 to 5 of the ASTEX Lagrangian experiment (see Table 2.3). The mean state of the atmosphere was calculated by bin-averaging all measurements collected during horizontal, profiling and porpoising legs of the respective flights over height intervals of 100 m and the standard deviation of each of the bins was calculated.

Figure 2.7 compares the aircraft observations with domain-averaged vertical profiles of thermodynamic state variables q_t, θ_l and q_l as well as the horizontal wind components u and v. The bin-averaged measurements are indicated by squares and the $\pm$ one standard deviation range of each bin is shown by error bars. We first notice that the modeled temperature and specific humidity in the free atmosphere agree well with the observations, suggesting realistic forcing tendencies due to radiation and large-scale subsidence. Moreover, the changes of the horizontal velocities u and v in time are close to those observed. Unfortunately, no measurements above 1800 m were collected during the last flight (hour 36).

During the first half of the transition the simulated temperature and humidity profiles in the boundary layer agree well with the observations, with maximum humidity and temperature differences staying within respectively $1\,\mathrm{g\,kg^{-1}}$ and 1 K. Considering the complexity of the case, the diversity of parameterization schemes used in the models and the relatively long simulation time this agreement between the models and observations is very encouraging.

The simulated bulk evolution of the boundary layer profiles shows great similarity with the conceptual model of the vertical structure of decoupled boundary layers as proposed by Wood and Bretherton (2004, Figure 1). Starting from a relatively shallow, well-mixed boundary layer, gradually a three-layered structure develops as the boundary layer deepens. Both the subcloud at the bottom of the boundary layer and the stratocumulus layer at the top are relatively well-mixed and connected by a cumulus layer. The bulk of the turbulent transport through this layer is governed by few cumulus updrafts. Without exception, the models reproduce this change of the boundary layer structure very well.

We notice some difference between model results and observations in the strength of the gradients of q_t and θ_l in the inversion layer during hours 8 and 19. This discrepancy could be due to the fact that the observations cover a much larger area including a larger spatial variability in the boundary layer height that

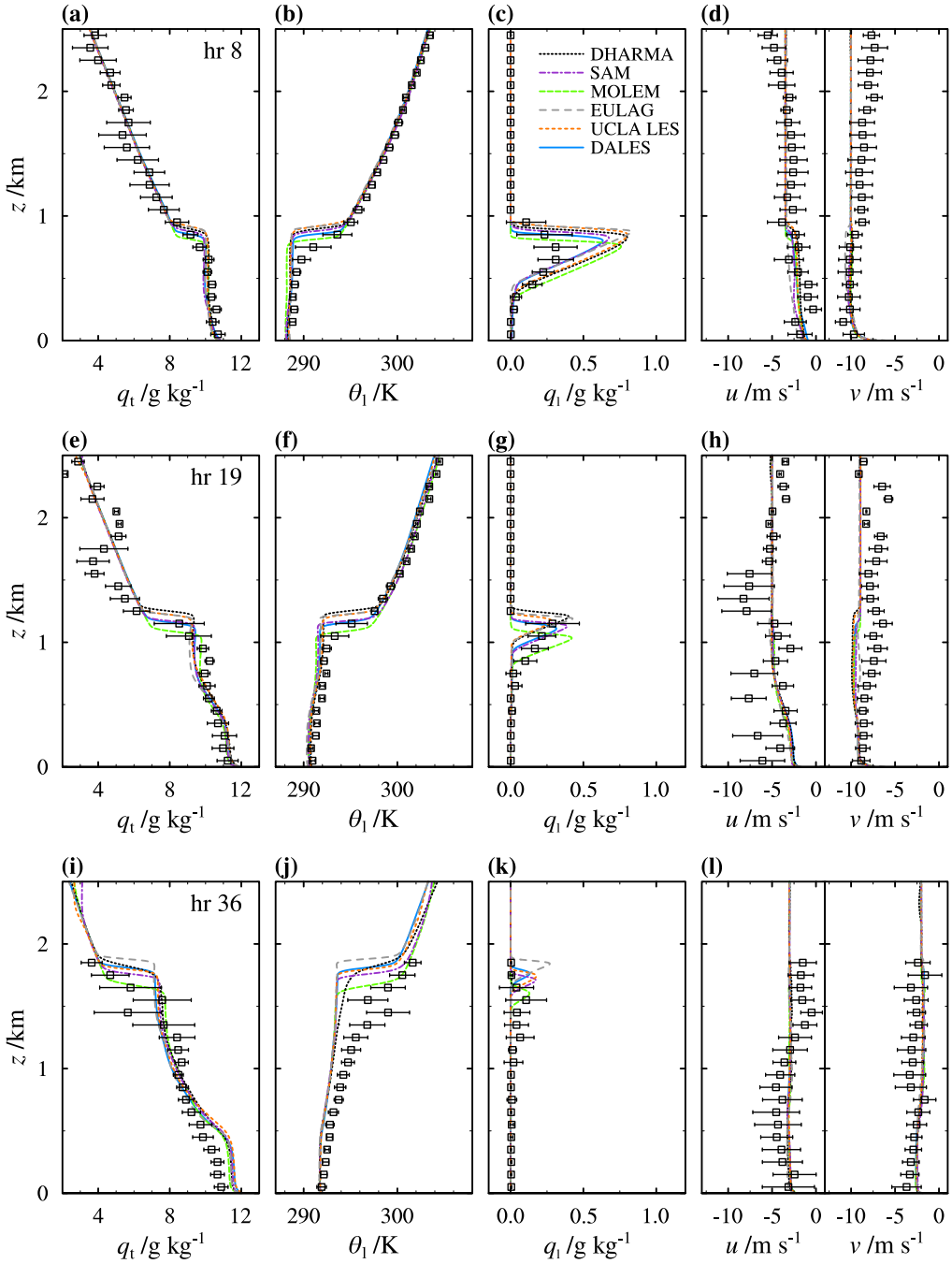

Figure 2.7. The domain averaged vertical profiles of the mean state variables q_t, θ_l, q_l and the horizontal wind components u and v for ASTEX flights 3 (a)-(d), 4 (e)-(h) and 5 (i)-(l). Lines styles and colors according to the legend. The black squares denote bin-averaged observations with the $\pm\sigma$ range indicated by the error bars.

cannot be represented in the rather limited horizontal LES domain. The result is that the simulated liquid water specific humidity profiles in Figures 2.7c and 2.7g have sharper peaks that are located more toward the top of the boundary layer as compared to the observed profiles.

During the last flight the temperature and humidity differences between models and observations are significantly larger than during the first half of the transition. It should be noted that many of the legs during this flight were cloud free and significantly warmer and drier than the cloudy legs. Temperature excursions of the order of 1 K were measured over distances of more than 50 km. This mesoscale variability complicates the comparison of the models with the observations. Note that in the DHARMA model the upper part of the boundary layer becomes warmer after the relatively fast breakup of the stratocumulus layer than in the other LES model results in which a solid stratocumulus cloud layer is maintained much longer. In the latter case longwave radiative loss at the top of the cloud layer causes a cooling tendency, which is significantly reduced when the cloud layer dissipates. Lastly, we note that high cirrus clouds were observed during the last flight. Their presence is neglected in the simulations, because their amount could not be estimated from the observations. However, as cirrus clouds increase the downwelling longwave radiation they actually reduce the cooling rate at the top of the cloud layer, which could partly explain the difference between the modeled and observed temperature.

2.3.3 Turbulence State Vertical Profiles

The horizontal flight legs each with a length of about 60 km were used to calculate the turbulence statistics. Mesoscale fluctuations were filtered out by applying a running average with a length of 3.1 km (De Roode and Duynkerke, 1997). The sampling error in the second order moments is estimated to be about 20 % for flights 3 and 4, and between 10 and 40 % for flight 5.

The turbulence state of the atmosphere during the flights is summarized by the profiles shown in Figure 2.8. It is clear from Figures 2.8a, 2.8d and 2.8h that the observed gradual decrease of the horizontally averaged turbulent kinetic energy e in time is well reproduced by the models. As the transition progresses, the e profiles in both the models and the observations develop a minimum in the middle of the boundary layer. The profiles of the vertical velocity variance $\overline{w'^2}$, which constitutes an important part of the turbulent kinetic energy, show this decreased turbulent mixing in the middle of the boundary layer more clearly, particularly during the second night (see Figure 2.8f). Only during the first night is a single peak in the vertical profile of $\overline{w'^2}$ present, which indicates that the boundary layer remains relatively well-mixed. Models that generate higher precipitation rates, for instance DALES and SAM, also tend to have a lower vertical velocity variance and a more decoupled structure, which was also found by Stevens et al. (1998).

The skewness of the vertical velocity S_w defined as:

$$S_w = \frac{\overline{w'^3}}{\left(\overline{w'^2}\right)^{3/2}}, \tag{2.7}$$

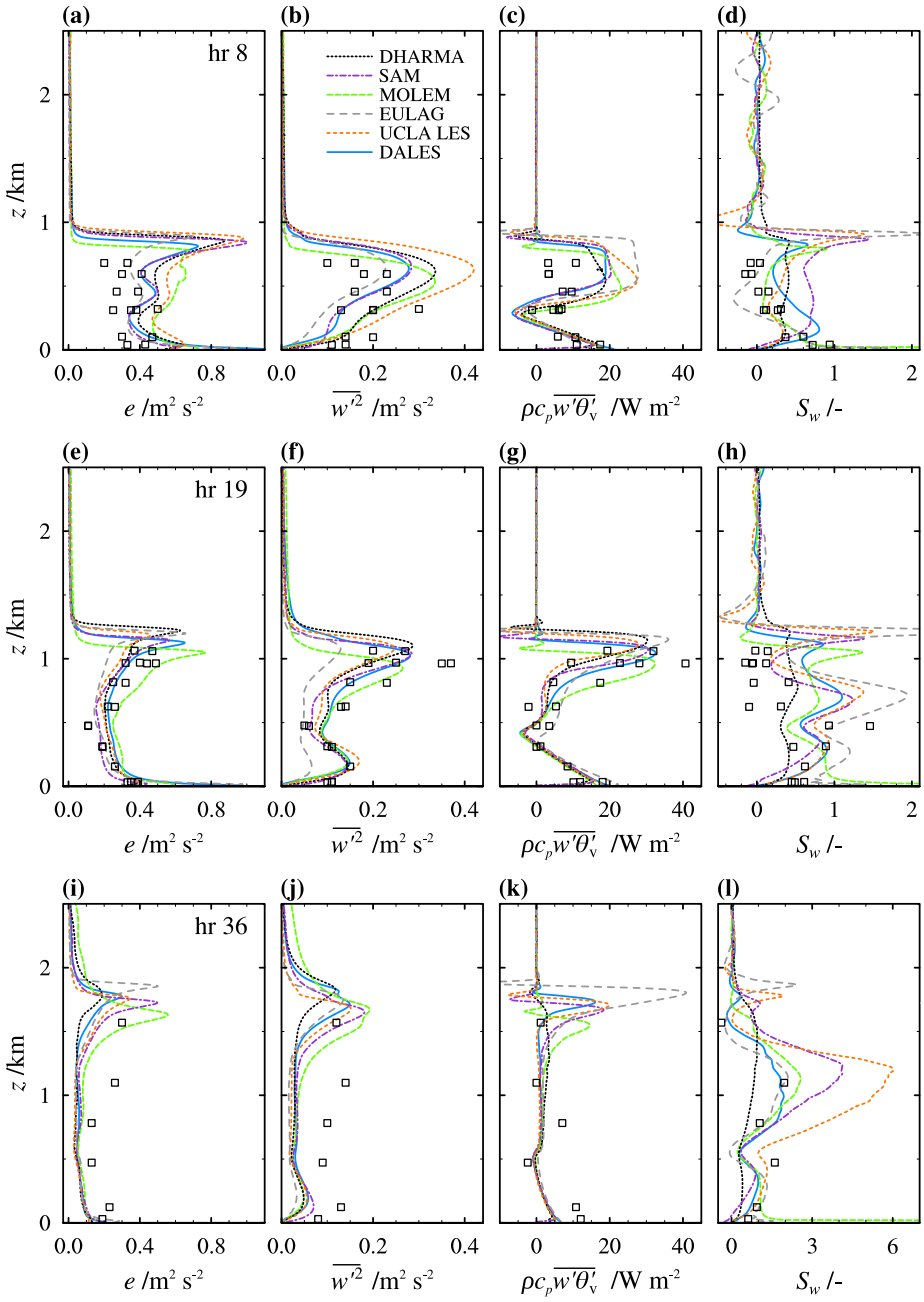

Figure 2.8. Vertical profiles of domain averaged turbulence statistics, the turbulent kinetic energy e, the vertical velocity variance $\overline{w'^2}$, the virtual potential temperature flux $\overline{w'\theta'_v}$ and the vertical velocity skewness S_w, for ASTEX flights 3 (a)-(d), 4 (e)-(h) and 5 (i)-(l). Lines styles and colors according to the legend. The black squares denote observations derived from measurement time series taken during horizontal flight legs. Note the different scale of the horizontal axis in Figure 2.8l.

increases steadily during the simulations. In the first part of the transition (Figure 2.8d), the negative skewness caused by downdrafts originating from the inversion almost completely cancels against the positive effect of updrafts from the surface, resulting in small values for S_w in the middle of the boundary layer. In the model simulations, updrafts seem to be more dominant in comparison to the observations. The large positive values for S_w shown in Figure 2.8l indicate the presence of rising cumulus clouds at the end of the transition. Their high upward velocities constitute the tail of the probability distribution of w which explains some of the intermodel spread in S_w.

Throughout the simulations the virtual potential temperature flux $\overline{w'\theta'_\mathrm{v}}$ is slightly negative at the top of the subcloud layer (see Figures 2.8c, 2.8g and 2.8k). The linear vertical profile of $\overline{w'\theta'_\mathrm{v}}$ and the approximately parabolic $\overline{w'^2}$ profile in the subcloud layer suggest a strong similarity with the dynamic structure of the clear convective boundary layer (Stevens et al., 2001). This subcloud layer structure seems to be very robust in the model results and the agreement with the observations is striking. A negative value for $\overline{w'\theta'_\mathrm{v}}$ indicates that rising thermals have a negative buoyancy that may prohibit them to rise further toward the stratocumulus layer. Nicholls (1984) and Bretherton and Wyant (1997) suggested that a subsequent decrease of vertical moisture transport out of the subcloud layer could result in a rapid thinning of the stratocumulus cloud layer. The results for this transition, however, indicate that stratocumulus clouds can persist for a day or more even when the boundary layer is not well-mixed.

The buoyancy peak is located at the top of the stratocumulus cloud layer, where the virtual potential temperature flux can be written in terms of turbulent fluxes of θ_l and q_t as follows:

$$\overline{w'\theta'_\mathrm{v}}_\mathrm{top} = A_w \overline{w'\theta'_\mathrm{l}}_\mathrm{top} + B_w \overline{w'q'_\mathrm{t}}_\mathrm{top}. \tag{2.8}$$

Here, $A_w \approx 0.5$ and $B_w \approx 1000\,\mathrm{K}$ are thermodynamic coefficients for a saturated environment. The subscripted "top" denotes variables at the top of the boundary layer just below the inversion. The turbulent flux of a conserved variable $\varphi \in \{q_\mathrm{t}, \theta_\mathrm{l}\}$ at the top of the boundary layer due to entrainment only can be approximated using the flux-jump relation (Lilly, 1968),

$$\overline{w'\varphi'}_\mathrm{ent} = -w_\mathrm{e}\Delta\varphi. \tag{2.9}$$

Here, Δ again denotes the difference between a variable just above and just below the inversion layer. Combining Eqs. (2.8) and (2.9) the following can be written:

$$\overline{w'\theta'_\mathrm{v}}_\mathrm{ent} = -w_\mathrm{e}\left(A_w\Delta\theta_\mathrm{l} + B_w\Delta q_\mathrm{t}\right). \tag{2.10}$$

According this equation, the increase of the buoyancy flux between hours 8 and 19 can in the first place be attributed to the strengthening of the inversion jump of q_t from approximately -2 to $-3\,\mathrm{g\,kg^{-1}}$ which is apparent from Figure 2.7. Stevens et al. (1998) furthermore found that precipitation tends to reduce the buoyancy flux. A second cause for the increase of $\overline{w'\theta'_\mathrm{v}}_\mathrm{top}$ is therefore the decrease of the precipitation rate between the mentioned hours.

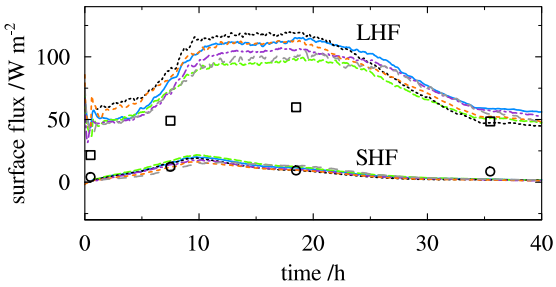

Figure 2.9. The surface fluxes of latent (upper set of lines and squares) and sensible heat (lower set and circles) as a function of time. Legend as in Figure 2.8. The observations are derived from the flight legs flown closest to the surface at approximately 30 m height, except for flight 2 for which the lowest available data was gathered at a height of approximately 160 m.

2.4 Humidity Budget

Following Bretherton et al. (1995), the humidity budget is analyzed next with a particular focus on the surface fluxes of latent heat and drizzle. Some additional sensitivity experiments will furthermore be discussed that have been performed in order to investigate the range of uncertainty resulting from the case setup.

2.4.1 Surface Latent Heat Flux

Figure 2.9 shows time-series of the modeled surface sensible (SHF) as well as the surface latent heat flux (LHF). The observed surface flux values shown in this figure were calculated from the flight legs performed in the surface layer at a height of about 30 m, except for flight 2 for which the lowest available data was gathered at a height of approximately 160 m. The results will be interpreted by means of the following bulk formula:

$$\overline{w'q'_{\mathrm{t}}}|_0 = C_q |\mathbf{u}|_{\mathrm{sl}} \left\{ q_{\mathrm{sat}}(T_{\mathrm{s}}) - q_{\mathrm{t,sl}} \right\} . \tag{2.11}$$

Here, C_q is the bulk transfer coefficient for moisture, $|\mathbf{u}|$ is the magnitude of the horizontal wind vector and $q_{\mathrm{sat}}(T_{\mathrm{s}})$ is the saturation specific humidity for the temperature of the surface (T_{s}). The subscripted "sl" denotes the surface layer. The surface LHF increases to approximately 100 W m^{-2} during the initial 10 hours of the simulation owing to an increase in both the SST and the horizontal wind speed. By contrast, during the second part of the transition the LHF lowers to around 50 W m^{-2} due to a considerable decrease of the total wind speed (see Figure 2.2a).

Despite the fact that close to the surface the modeled humidity and horizontal wind velocity agree well with the observations (Figure 2.7), the modeled surface LHF is much larger than in the observations. The reported uncertainty in the SST is about 0.5 K (Bretherton et al., 1995), which corresponds to a saturation specific humidity uncertainty of 0.45 g kg^{-1} following Clausius-Clapeyron. This

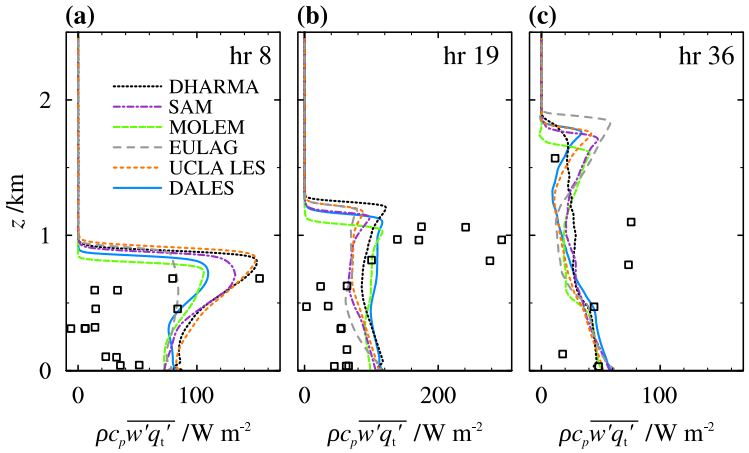

Figure 2.10. Domain averaged profiles of the turbulent humidity flux $\overline{w'q_t'}$ for the hours corresponding to flights 3 (a), 4 (b) and 5 (c). The black squares denote observations. Note the different scale of the horizontal axis in Figure (b).

translates into an uncertainty of only 15 % in the modeled surface flux assuming no other variables are influenced. The remaining variable in Eq. (2.11) is the bulk transfer coefficient for moisture C_q. This transfer coefficient is determined among others from the surface roughness length z_0 which is prescribed to be constant at 0.2 mm. This value is typically used for open sea conditions. However, z_0 is actually determined by the wave height, which in turn is a function of the horizontal wind velocity close to the surface. This effect is described by the Charnock relation,

$$z_0 = \frac{\alpha_c u_*^2}{g}, \tag{2.12}$$

in which u_* is the friction velocity, g is gravitational acceleration and α_c is the Charnock parameter. The value of α_c varies significantly among models: $0.011 \lesssim \alpha_c \lesssim 0.018$ (Renfrew et al., 2002). A test was performed with DALES in which the Charnock relation was used to determine z_0, in order to assess the effect of this variable roughness length on the surface LHF. Using a typical value $\alpha_c = 0.015$ results in $z_0 \approx 0.16$ mm during the first 20 hours of the simulation, which is somewhat lower than the prescribed constant value of 0.2 mm that was used for the reference simulation. In the second half of the transition, z_0 decreases steadily to about 0.03 mm. The lower z_0 causes a decrease of the surface LHF throughout the transition of about 15 % as compared to the reference simulation. However, it has no significant effect on the LWP or on the timing of stratocumulus cloud breakup.

Apart from Charnock's relation, SCMs often use a lower value of the surface roughness length for moisture and heat than for momentum (see also Vickers and Mahrt, 2010, for observational evidence). Therefore, an additional test was performed in which the value of z_0 for humidity and heat was one tenth that for momentum: $z_{0q,\mathrm{h}} = z_{0\mathrm{m}}/10$. Again, a reduction of the LHF of about 10–15 %

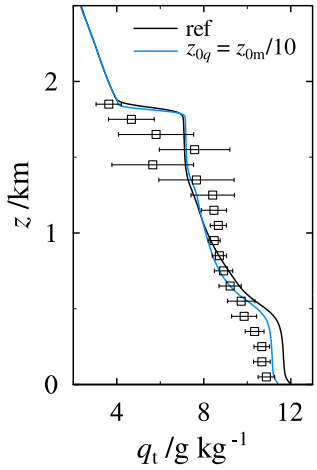

Figure 2.11. Horizontally averaged q_t profiles for the reference simulation (black) as well as the simulation with $(z_{0q}, z_{0h}) = z_{0m}/10 = 0.02\,\text{mm}$ (blue) at hour 36 of the simulation.

was found. In Figure 2.11 the humidity profile of this test is compared with the reference simulation. Clearly, the decrease of the surface roughness length causes the humidity in the subcloud layer to decrease by about $0.5\,\text{g}\,\text{kg}^{-1}$, which is in better agreement with the observations than the results of the reference simulation. The humidity in the cloud layer remains virtually unaffected.

2.4.2 Moisture Flux at Stratocumulus Cloud Base

Figure 2.10 clearly shows that the modeled turbulent humidity fluxes in the subcloud layer are systematically larger than observed. In the cloud layer, the collected high-frequency humidity measurements have a large error (Wang and Lenschow, 1995). More accurate humidity measurements from a different instrument are available, but the sampling frequency of 1 Hz is too low to yield accurate flux estimates. However, an estimate of the magnitude of $\overline{w'q_t'}$ in the stratocumulus layer can be obtained from the observed $\overline{w'\theta_v'}$ and $\overline{w'\theta_l'}$ fluxes using Eq. (2.8). Using for example the observations from flight 4, this method gives a maximum value of about $100\,\text{W}\,\text{m}^{-2}$ at the top of the boundary layer. These estimates therefore suggest that the observations of $\overline{w'q_t'}$ in the cloud layer that are shown in Figure 2.10 are probably too high.

Despite the fact that the buoyancy flux at the top of the subcloud layer is significantly negative throughout the simulations (Figure 2.8), the vertical variations in the simulated turbulent vertical humidity fluxes are very small in the subcloud layer. This indicates that much of the moisture evaporating from the surface is transported to the cloud layer. As such, the modeled flux profiles do not exhibit the strongly decoupled structure with humidity fluxes going to zero at the top of the subcloud layer as suggested in early studies by Nicholls (1984) or Bougeault (1985). To quantify how much moisture actually is transported from the subcloud to the

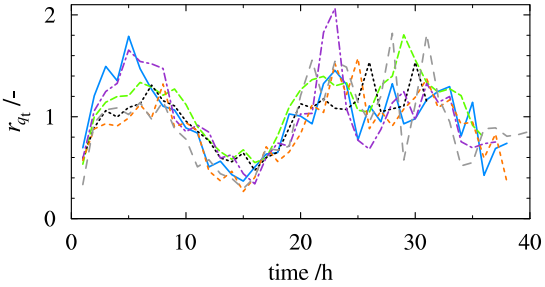

Figure 2.12. The ratio r_{q_t} of the humidity flux at mean cloud base z_b to the surface flux as defined in Eq. (2.13). Legend as in Figure 2.10. The series are cut off as soon as the average cloud cover drops below 0.95.

stratocumulus cloud layer and how this amount relates to the surface evaporation we define the quantity r_{q_t} which gives the ratio of the moisture flux at the mean cloud base z_b over the flux at the surface:

$$r_{q_t} = \frac{\overline{w'q_t'}(z_b)}{\overline{w'q_t'}(0)}. \tag{2.13}$$

A clear diurnal cycle in r_{q_t} is visible in Figure 2.12, with values exceeding unity during the night and a distinct minimum during the first day. This suggests that the decoupling of the boundary layer is much more effective in reducing the upward moisture transport to the stratocumulus cloud layer during the day than for night-time conditions. It is interesting to note that during the first day of the transition the model mean value of r_{q_t} is about 0.95, which suggests a near zero divergence of the moisture flux for the ASTEX subcloud layer.

2.4.3 Precipitation

The surface precipitation flux as a function of time is shown in Figure 2.13b. This flux is relatively large during the first night, with domain averaged values of up to $30\,\mathrm{W\,m^{-2}}$ ($\approx 1\,\mathrm{mm\,d^{-1}}$). Surface precipitation rates rapidly drop to zero as the cloud layer thins during the day. The observed and modeled precipitation rates are significantly different, particularly at hours 8 and 19, which raises questions about the observations, as we will now show. For comparison we also calculated the precipitation rate at cloud base from a relation between the LWP and the cloud droplet number density N_c based on observations (Comstock et al., 2004),

$$\rho L_v P(z_b) = 10.8 \left(\frac{\mathrm{LWP}}{N_c}\right)^{1.75}. \tag{2.14}$$

Here, $(\rho L_v P)$, LWP and N_c are in $\mathrm{W\,m^{-2}}$, $\mathrm{g\,m^{-2}}$ and $\mathrm{cm^{-3}}$ respectively. Geoffroy et al. (2008) give a thorough overview of drizzle parameterizations, which includes a similar relation by vanZanten et al. (2005). That relation is found to give almost identical results as the one from Comstock et al. (2004) presented in Figure 2.13a.

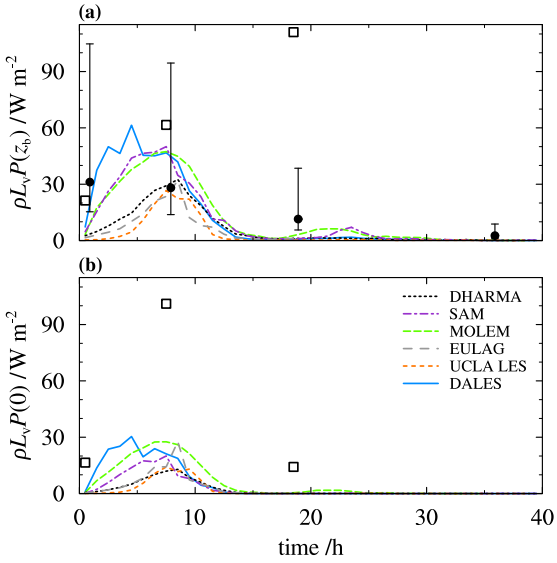

Figure 2.13. The precipitation rate P in units of W m^{-2} at mean cloud base height z_b (a) and at the surface (b) for the models denoted in the legend. Squares denote average precipitation rates obtained from the flight legs that were flown closest to the mentioned levels. The black dots show parameterized precipitation rates at z_b calculated using Eq. (2.14) with a cloud droplet number concentration $N_c = 100\,\mathrm{cm}^{-3}$, while the error bars indicate the range of precipitation rates spanned using $N_c = 50$ and $150\,\mathrm{cm}^{-3}$.

The model results and direct observations (squares) are also shown in this figure. The error bars span the range of observed droplet number densities $N_c = 50$ to 150 cm^{-3} (respectively the upper and lower bounds) as reported by Bretherton and Pincus (1995). The results calculated using the parameterization of Eq. (2.14) show a trend that is consistent with the LES results and hint at an overestimation of the precipitation rates as diagnosed from the observations.

During the first hours of the simulations there are significant intermodel differences in the precipitation rates. Models that are less prone to produce rain allow the LWP to grow during the first night (compare Figure 2.5). These models also start producing rain as the LWP increases. All models eventually have similar precipitation rates around hour 10, but at different values of the LWP.

Figure 2.14 shows a clear correlation between the precipitation rate at stratocumulus cloud base and the LWP, both of which are averages of the model results during the first 12 hours of the simulation. Additional simulations were performed with DALES, using $N_c = 60$, 100 (reference) and $200\,\mathrm{cm}^{-3}$. These cases were run using two microphysics schemes: the scheme by Khairoutdinov and Kogan (2000, KK00 hereafter), which was used for the reference simulation, and the scheme of Seifert and Beheng (2001, SB01). The top axis of the Figure 2.14 shows a rough indication of the LWP tendency due to the removal of liquid water by precipitation

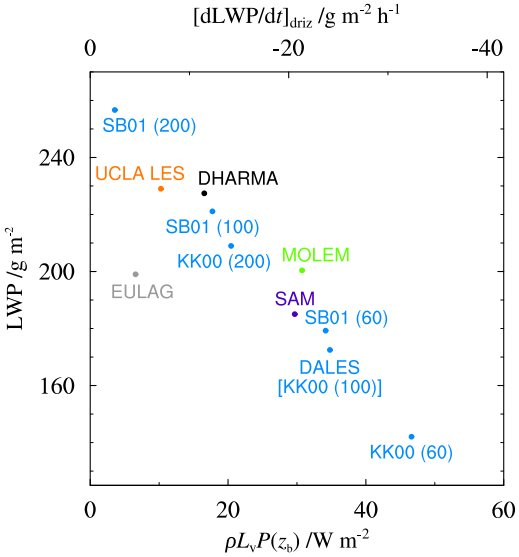

Figure 2.14. Scatter plot of the time averaged LWP as a function of time averaged precipitation rate at stratocumulus cloud base, both of which are averages of the model results during the first 12 hours of the transition. The top axis shows the precipitation rate in terms of a LWP tendency in $\mathrm{g\,m^{-2}\,h^{-1}}$ as given by Eq. (2.15). The labels indicate the model or the microphysics scheme (in DALES) used, while the numbers between the parentheses indicate the cloud droplet number density in $\mathrm{cm^{-3}}$.

only:

$$\left[\frac{\mathrm{d\,LWP}}{\mathrm{d}t}\right]_{\mathrm{driz}} = -\frac{P(z_{\mathrm{b}})}{L_{\mathrm{v}}} \tag{2.15}$$

in units of $\mathrm{g\,m^{-2}\,h^{-1}}$ (Van der Dussen et al., 2014). Note that the effect of evaporation of precipitation below cloud base is neglected in this tendency. The estimated LWP difference between for instance the UCLA LES and DALES results over the 12 hour period is approximately $250\,\mathrm{g\,m^{-2}}$.

A secondary effect of a higher precipitation rate is a decrease of the entrainment rate as was already shown by Nicholls (1984) and Chen and Cotton (1987) among others. Ackerman et al. (2004) therefore argue that the LWP response to increased precipitation is the result of the competition between the increased removal of liquid water from the boundary layer and the reduced drying due to the lower entrainment rate. The free atmosphere was relatively moist during ASTEX, such that the former response is dominant.

Figure 2.15 shows that the average entrainment rate indeed decreases with increased precipitation rate. It is striking to see that the model results exhibit this strong correlation between the precipitation rate at cloud base and the entrainment rate considering the multitude of processes through which microphysics impact on the boundary layer dynamics (Ackerman et al., 2009). The scatter plots shown in Figure 2.14 and 2.15 furthermore suggest that the significant spread noted

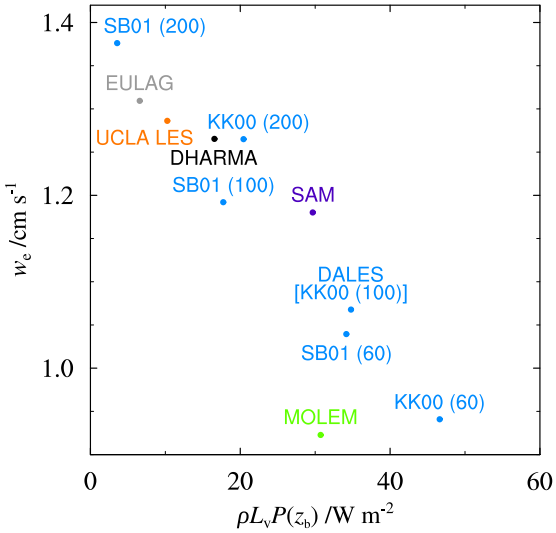

Figure 2.15. As Figure 2.14, but here for the entrainment rate w_e.

in the modeled LWP and entrainment rates during the first 12 hours is mainly attributable to the differences among the microphysics parameterization schemes.

The simulation results nevertheless indicate that the pace of the transition is hardly related to the microphysical details of the models. SAM, MOLEM, UCLA LES and DALES all predict the breakup of the stratocumulus cloud layer at approximately the same time (see Figure 2.4), despite their strongly varying precipitation rates. This is basically due to the strong decrease of the LWP during the first day. The thin veil of stratocumulus cloud at the top of the boundary layer that remains after this first day does not support significant amounts of precipitation, such that the LWP and entrainment differences among the models stay relatively small for the remainder of the transition.

2.5 Discussion and Conclusions

In this study the stratocumulus transition as observed during the ASTEX field experiment is simulated by six different LES models. Despite the complexity of the case, including multiple time-varying boundary conditions, a diurnally varying interactive radiative forcing, the inclusion of parameterized microphysical processes and the long simulation time of 40 hours, the model results agree remarkably well with the aircraft observations. In particular, the models are able to closely reproduce the evolution of a vertically well-mixed stratocumulus-topped boundary layer to a much deeper decoupled boundary layer with shallow cumulus clouds penetrating stratocumulus above. Particular features of the observed turbulence structure, such as the strong increase of the buoyancy flux at the top of the boundary layer and the development of a double-peaked vertical velocity variance profile, are also well captured by the models.

The ratio of the turbulent humidity flux at the stratocumulus cloud base to the surface evaporation flux is shown to exhibit a distinct diurnal cycle. It exceeds unity during the night implying a net drying of the subcloud layer and moistening during the day. This also indicates that during the night the cumulus clouds are much more efficient in feeding the stratocumulus cloud layer with moisture from the subcloud layer than during daytime (Martin et al., 1995; Chung et al., 2012).

The largest source of spread among the models is arguably due to the parameterization of microphysical processes. In particular, additional sensitivity simulations using DALES indicate that the precipitation flux is reduced by about 50 % if the microphysics scheme is changed from the one proposed by Khairoutdinov and Kogan (2000) to Seifert and Beheng (2001). The substantial differences in LWP (exceeding $100\,\mathrm{g\,m^{-2}}$) and entrainment rate (about $0.3\,\mathrm{cm\,s^{-1}}$) among the models during the first night are shown to be strongly related to the magnitude of the precipitation flux at stratocumulus cloud base. Unfortunately, the uncertainty in the precipitation rates derived from the observations is too large to conclude which microphysics scheme should be preferred over another. Specifically, a comparison of the ASTEX observed drizzle rates with results from a parameterization based on a careful analysis of more recent field observations by Comstock et al. (2004) shows that the former are much larger. The differences that emerge in the modeled LWPs during the first night are diminished during daytime because clouds with a high LWP tend to absorb more radiation and therefore evaporate more liquid water. During the subsequent night the cloud layer is too thin to maintain significant drizzle rates.

As the values for the surface roughness length for scalars like moisture and heat used by the LES models are higher than the typical values used in climate and weather forecast models, a sensitivity test was performed using DALES. This simulation shows that a reduction of the roughness length for scalars by a factor of 10 results in a reduction of the surface latent heat flux by about 15 %, which however does not significantly affect the timing of cloud breakup. The subcloud humidity at the end of the transition is approximately $0.5\,\mathrm{g\,kg^{-1}}$ lower than for the reference simulation and is in better agreement with the observations. This result therefore suggests that for this study a smaller value of the surface roughness length for scalars would be more appropriate for LES models than the value that was originally proposed.

At the end of the transition the observed temperature in the stratocumulus cloud layer is significantly higher than in the simulations. The cold bias in the modeling results might be partly due to the observed appearance of cirrus clouds. Their effect on the longwave radiative cooling at the stratocumulus cloud top has been neglected in the simulations, because the precise amount of these high clouds could not be derived from the aircraft observations. The LES models furthermore used a rather small horizontal domain such that mesoscale organization of clouds could not be captured. Careful inspection of the aircraft observations shows significant mesoscale fluctuations, with lower temperatures in the stratocumulus-topped cloud layers as compared to the surrounding clear areas.

The results of this research show that much progress has been made in the modeling of stratocumulus transitions since the previous intercomparison cases based on ASTEX (Duynkerke et al., 1999; Bretherton et al., 1999a). This progress is

mainly attributable to the availability of sufficient computational power to perform the required multi-day simulations using a three-dimensional LES model at high resolution instead of one- or two-dimensional turbulence models. Other important improvements are the incorporation of advanced parameterization schemes for radiation and precipitation as well as the use of prescribed SSTs instead of the prescribed surface flux forcing used in the previous LES intercomparison studies based on flights 2 and 3 of the first Lagrangian.

In contrast to the aircraft observations, the LES model results now provide a continuous and internally consistent representation of the stratocumulus transition that took place during the ASTEX first Lagrangian. Furthermore, the LESs give the opportunity to evaluate the performance of specific parameterization schemes by providing detailed information such as mass flux statistics that is difficult to obtain from observations. This makes these results valuable as a benchmark for the evaluation and further development of parameterizations schemes of SCMs within the GCSS strategy (Randall et al., 2003).

Acknowledgements

The research leading to these results has received funding from the European Union, Seventh Framework Programme (FP7/2007-2013) under grant agreement n° 244067. ECMWF ERA-Interim data used in this project have been obtained from the ECMWF data server. The work was sponsered by the National Computing Facilities Foundation (NCF) for the use of supercomputer facilities. We kindly thank Coen Hennipman and Arjan van Leeuwen for providing analysis used in this paper and Gunilla Svensson for helpful suggestions regarding the set-up of the case. We also thank two anonymous reviewers whose comments helped to improve the quality of the manuscript.

3

Factors Controlling Rapid Stratocumulus Cloud Thinning

The relationship between the inversion stability and the liquid water path (LWP) tendency of a vertically well-mixed, adiabatic stratocumulus cloud layer is investigated in this study through the analysis of the budget equation for the LWP. The LWP budget is mainly determined by the turbulent fluxes of heat and moisture at the top and the base of the cloud layer as well as by the source terms due to radiation and precipitation. Through substitution of the inversion stability parameter κ into the budget equation, it immediately follows that the LWP tendency will become negative for increasing values of κ due to the entrainment of increasingly dry air. Large κ values are therefore associated with strong cloud thinning. Using the steady state solution for the LWP, an equilibrium value κ_{eq} is formulated, beyond which the stratocumulus cloud will thin. The DYCOMS-II stratocumulus case is used to illustrate that, depending mainly on the magnitude of the moisture flux at cloud base, stratocumulus clouds can persist well within the buoyancy reversal regime.

Published in *J. Atmos. Sci.* (2014) with S.R. de Roode and A.P. Siebesma.

3.1 Introduction

Buoyancy reversal at the top of a stratocumulus layer has often been suggested as a major stratocumulus cloud dissolving mechanism. Lilly (1968) hypothesized that under certain inversion conditions, parcels that are entrained from above the inversion can become negatively buoyant by mixing with saturated air inside the cloud layer. As these parcels sink, turbulence kinetic energy is generated such that additional entrainment is promoted. Such runaway entrainment would rapidly warm and dry the cloud layer, leading to its breakup.

Randall (1980) and Deardorff (1980a) formulated a criterion for this process to occur by determining the minimum buoyancy of entrained parcels. This criterion can be expressed in terms of an inversion stability parameter κ, which is a function of the ratio of the inversion jumps of total specific humidity and liquid water potential temperature (Δq_t and $\Delta\theta_\mathrm{l}$ respectively):

$$\kappa \equiv 1 + \frac{c_p}{L_\mathrm{v}} \frac{\Delta\theta_\mathrm{l}}{\Delta q_\mathrm{t}}. \tag{3.1}$$

Here, c_p is the specific heat of air and L_v is the latent heat of vaporization of water. Siems et al. (1990) showed that using Eq. (3.1) the Randall and Deardorff criterion can conveniently be written as $\kappa > \kappa_\mathrm{BR}$, where $\kappa_\mathrm{BR} = 0.23$. Similar criteria have been suggested by among others MacVean and Mason (1990), Siems et al. (1990) and Duynkerke (1993) (see for an overview Yamaguchi and Randall, 2008).

However, Kuo and Schubert (1988) found that most of the available stratocumulus observations lie within the buoyancy reversal regime. Siems et al. (1990) furthermore performed laboratory experiments from which they concluded that a positive entrainment feedback due to buoyancy reversal does not occur under realistic stratocumulus conditions. Similar conclusions are drawn from recent high resolution large-eddy simulation (LES) results by Yamaguchi and Randall (2008), who find that spontaneous entrainment as a result of evaporative cooling indeed exists, but the effect is weak and does not lead to runaway entrainment. Mellado et al. (2009) furthermore conclude from linear stability and numerical analyses that evaporative cooling of entrained parcels does enhance the turbulence generation slightly below the inversion, but the entrainment velocity is not affected.

Nevertheless, the LES results of Moeng (2000) and more recently of Lock (2009) strongly suggest that cloud cover in stably stratified boundary layers tends to decrease rapidly beyond a certain critical value for κ. Similarly, Noda et al. (2013) show from LESs of transient stratocumulus-topped boundary layers that for larger values of κ the LWP tendency is more negative and the cloud layer tends to break up earlier.

The κ dependency of cloud cover is particularly interesting in connection to climate perturbation studies. The value of κ will typically increase in climate warming scenarios, as $\Delta\theta_\mathrm{l}$ remains approximately constant while the magnitude of the humidity jump increases as a result of Clausius-Clapeyron scaling (Bretherton et al., 2013; Bretherton and Blossey, 2014). A thorough understanding of how this will affect the low cloud cover is important for determining the magnitude of the cloud-climate feedback (Stephens, 2005).

Stratocumulus-to-cumulus transitions that are often observed over subtropical oceans provide further motivation for the research presented in this article. As stratocumulus cloud fields are advected toward the equator, the magnitude of the humidity jump over the capping inversion Δq_t typically increases due to the deepening of the boundary layer in combination with the negative humidity gradient in the free atmosphere, and the increase of the surface saturation specific humidity as the sea surface temperature increases. The temperature jump $\Delta\theta_l$ typically changes less rapidly as the sea surface temperature increase counteracts the stabilizing effect of boundary layer deepening. The increase of the magnitude of Δq_t therefore dominates the change in κ, causing it to increase. Eventually the stratocumulus cloud breaks up and a transition to cumulus clouds is observed.

Four stratocumulus transitions have been simulated as a model intercomparison of the combined GASS[1] and EUCLIPSE[2] projects. These cases mainly differ in the magnitude of the initial temperature and humidity jumps. For a detailed description of the three composite cases see Sandu and Stevens (2011). The setup of the transition based on the Atlantic Stratocumulus Transition EXperiment (ASTEX; Albrecht et al., 1995) is described by Van der Dussen et al. (2014). Two-hourly averaged values of the cloud fraction as a function of κ for these four cases, obtained using the Dutch Atmospheric LES (DALES), are shown in Figure 3.1. Sandu and Stevens (2011) presented in a similar figure the results of the composite transition cases obtained using the University of California, Los Angeles (UCLA) LES model. These results also indicate that the cloud fraction σ decreases rapidly beyond some critical κ.

For the ASTEX transition, this critical κ value is clearly lower than for the composite transition cases. This apparent lack of an universal critical value for κ has also been found by Xiao et al. (2011), who concluded that decoupling of the boundary layer causes stratocumulus breakup to occur at lower κ values. The study thus shows that the critical value for κ depends on the moisture supply at the stratocumulus cloud base. These examples can not be sufficiently explained by the existing κ criteria that are based on buoyancy reversal argumentation.

In the following section, we will derive an equation for the tendency of the liquid water path (LWP) of adiabatic stratocumulus cloud layers. This equation is then rewritten in terms of κ, which shows that for sufficiently large values of κ the cloud thinning tendency due to entrainment drying and warming becomes so large that it cannot be compensated anymore by cloud building processes. In Section 3.3, a simple entrainment relation is assumed that allows for the derivation of an equilibrium value of κ for which the LWP is constant in time. The results are furthermore linked to the Klein and Hartmann (1993) relation, which describes the cloud cover as a function of the bulk stability of the boundary layer. The final section contains a short summary of the conclusions.

3.2 Theory

Randall (1984) derived an equation for the tendency of q_l^t, the liquid water specific

[1] Global Atmosperic System Study
[2] European Union CLoud Intercomparison, Process Study & Evaluation

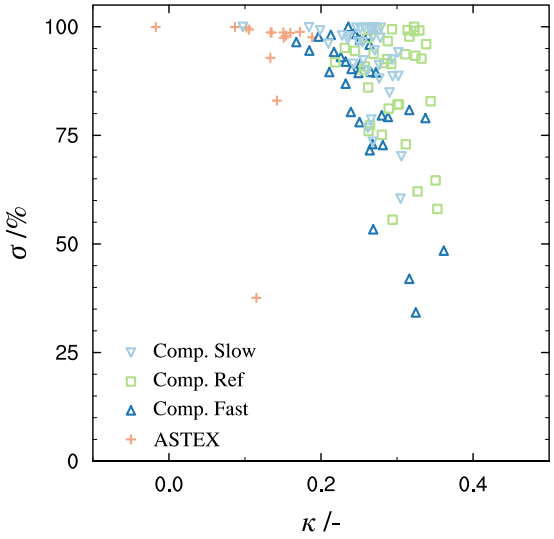

Figure 3.1. Two-hourly averaged cloud cover σ as a function of κ for the four GASS/EUCLIPSE model intercomparison cases, as indicated by the legend. The simulations where performed using the Dutch Atmospheric LES (DALES, Heus et al., 2010).

humidity at the top of a well-mixed stratocumulus-topped boundary layer, in order to investigate the effect of entrainment on the cloud layer. For such boundary layers, q_l^t is a function of q_t and θ_l in the cloud layer as well as of the inversion height z_i, such that the following can be written:

$$\frac{\partial q_\mathrm{l}^\mathrm{t}}{\partial t} = \frac{\partial q_\mathrm{l}^\mathrm{t}}{\partial q_\mathrm{t}}\frac{\partial q_\mathrm{t}}{\partial t} + \frac{\partial q_\mathrm{l}^\mathrm{t}}{\partial \theta_\mathrm{l}}\frac{\partial \theta_\mathrm{l}}{\partial t} + \frac{\partial q_\mathrm{l}^\mathrm{t}}{\partial z_\mathrm{i}}\frac{\partial z_\mathrm{i}}{\partial t}. \tag{3.2}$$

Note that the partial derivatives imply that all but the variable of interest are kept constant.

Using the trapezoidal rule, q_l^t can be related to the LWP, giving

$$\mathrm{LWP} = \int_{z=0}^{\infty} \rho q_\mathrm{l} \mathrm{d}z \approx \frac{1}{2}\rho h q_\mathrm{l}^\mathrm{t}. \tag{3.3}$$

Here, ρ is the total density of air and h is the thickness of the cloud layer. This relation assumes that q_l varies approximately linearly with height in the cloud layer,

$$\frac{\partial q_\mathrm{l}}{\partial z} = -\Gamma_{q_\mathrm{l}}, \tag{3.4}$$

in which Γ_{q_l} is the lapse rate of the liquid water specific humidity. We assume that the cloud layer is vertically well mixed as a result of the destabilizing effect of longwave radiative cooling at cloud top and accordingly the q_l lapse rate is adiabatic. Following the conceptual model for stratocumulus-topped boundary layers of Park et al. (2004) and Wood and Bretherton (2004), the stratocumulus

cloud layer is allowed to have a different θ_l and q_t than the subcloud layer. Both layers are then connected by a conditionally unstable layer in which cumuli are responsible for the transport of moisture to the stratocumulus layer (e.g. Wang and Lenschow, 1995). In other words, the stratocumulus layer is well-mixed even though the boundary layer as a whole is possibly decoupled.

Integration of Eq. (3.4) shows that $q_\mathrm{l}^\mathrm{t} = \Gamma_{q_\mathrm{l}} h$, such that the LWP tendency can be written as follows:

$$\begin{aligned}\frac{\partial \mathrm{LWP}}{\partial t} =& \frac{1}{2}\frac{\partial}{\partial t}\left(\rho \Gamma_{q_\mathrm{l}} h^2\right) \approx \\ & \rho h \frac{\partial}{\partial t}\left(\Gamma_{q_\mathrm{l}} h\right) = \rho h \frac{\partial q_\mathrm{l}^\mathrm{t}}{\partial t}.\end{aligned} \tag{3.5}$$

This equation shows that the LWP tendency is linearly related to the tendency of q_l^t to q_t and θ_l in Eq. (3.2).

Expressions for the partial derivatives of q_l^t in Eq. (3.2) are derived in the Appendix:

$$\frac{\partial q_\mathrm{l}^\mathrm{t}}{\partial q_\mathrm{t}} = \quad \eta \tag{3.6a}$$

$$\frac{\partial q_\mathrm{l}^\mathrm{t}}{\partial \theta_\mathrm{l}} = -\Pi\gamma\eta \tag{3.6b}$$

where the variable

$$\eta = \left(1 + \frac{L_\mathrm{v}\gamma}{c_p}\right)^{-1} \tag{3.7}$$

accounts for the latent heat release (uptake) associated with the condensation (evaporation) of liquid water. The value of η depends mainly on temperature. For subtropical stratocumulus clouds $\eta \approx 0.4$. Furthermore, Π is the Exner function and $\gamma = \partial q_\mathrm{s}/\partial T$ is the change of the saturation specific humidity q_s with temperature T as described by the Clausius-Clapeyron relation.

The entrainment rate and the large-scale vertical velocity $\overline{w}$ together determine the rate of change of the inversion height with time:

$$\frac{\partial z_\mathrm{i}}{\partial t} = w_\mathrm{e} + \overline{w}(z_\mathrm{i}). \tag{3.8}$$

Through substitution of Eqs. (3.5), (3.6) and (3.8), Eq. (3.2) becomes:

$$\frac{1}{\rho h}\frac{\partial \mathrm{LWP}}{\partial t} = \eta\frac{\partial q_\mathrm{t}}{\partial t} - \Pi\gamma\eta\frac{\partial \theta_\mathrm{l}}{\partial t} - \Gamma_{q_\mathrm{l}}\left[w_\mathrm{e} + \overline{w}(z_\mathrm{i})\right]. \tag{3.9}$$

The tendencies of q_t and θ_l in this equation are governed by their respective Reynolds-averaged budget equations:

$$\frac{\partial q_\mathrm{t}}{\partial t} = -\frac{\partial \overline{w'q_\mathrm{t}'}}{\partial z} - \frac{\partial P}{\partial z}, \tag{3.10a}$$

$$\frac{\partial \theta_\mathrm{l}}{\partial t} = -\frac{\partial \overline{w'\theta_\mathrm{l}'}}{\partial z} - \frac{1}{\Pi}\frac{\partial F_\mathrm{rad}}{\partial z} + \frac{L_\mathrm{v}}{c_p\Pi}\frac{\partial P}{\partial z}, \tag{3.10b}$$

which include the effects of the precipitation (P in $\mathrm{m\,s^{-1}}$) and net radiative fluxes (F_{rad} in $\mathrm{K\,m\,s^{-1}}$). The overbars have been omitted for notational convenience, except for the turbulent fluxes. Variations of the Exner function throughout the cloud layer are assumed to be negligibly small.

By assuming a well-mixed stratocumulus cloud layer as before, Eqs. (3.10) can straightforwardly be integrated from cloud base, denoted by a superscript "b", up to cloud top, which results in:

$$h\frac{\partial q_{\mathrm{t}}}{\partial t} = w_{\mathrm{e}}\Delta q_{\mathrm{t}} + \overline{w'q'_{\mathrm{t}}}^{\,\mathrm{b}} - \delta P, \tag{3.11a}$$

$$h\frac{\partial \theta_{\mathrm{l}}}{\partial t} = w_{\mathrm{e}}\Delta \theta_{\mathrm{l}} + \overline{w'\theta'_{\mathrm{l}}}^{\,\mathrm{b}} - \frac{\delta F_{\mathrm{rad}}}{\Pi} + \frac{L_{\mathrm{v}}}{c_p\Pi}\delta P. \tag{3.11b}$$

The inversion jumps and the entrainment rate w_{e} entered this equation through the use of the flux-jump relation: $\overline{w'\varphi'}^{\,\mathrm{t}} = -w_{\mathrm{e}}\Delta\varphi$ (Lilly, 1968). The δ indicates a difference between cloud top and base, such that for longwave cooling: $\delta F_{\mathrm{rad}} > 0$. As the precipitation flux is defined negative downwards and no precipitation enters the cloud layer at the top: $\delta P > 0$.

When Eqs. (3.11) are used in Eq. (3.9), an equation is acquired for the total LWP tendency. This equation can conveniently be split into the contributions of the five relevant processes: turbulent fluxes at cloud base ('Base'), entrainment ('Ent'), radiation ('Rad'), precipitation ('Prec') and subsidence ('Subs'):

$$\frac{\partial \mathrm{LWP}}{\partial t} = \mathrm{Ent} + \mathrm{Base} + \mathrm{Rad} + \mathrm{Prec} + \mathrm{Subs},$$

in which

$$\mathrm{Ent} = \rho w_{\mathrm{e}}\left(\eta\Delta q_{\mathrm{t}} - \Pi\gamma\eta\Delta\theta_{\mathrm{l}} - h\Gamma_{q_{\mathrm{l}}}\right), \tag{3.12a}$$

$$\mathrm{Base} = \rho\eta\left(\overline{w'q'_{\mathrm{t}}}^{\,\mathrm{b}} - \Pi\gamma\overline{w'\theta'_{\mathrm{l}}}^{\,\mathrm{b}}\right), \tag{3.12b}$$

$$\mathrm{Rad} = \rho\eta\gamma\delta F_{\mathrm{rad}}, \tag{3.12c}$$

$$\mathrm{Prec} = -\rho\delta P, \tag{3.12d}$$

$$\mathrm{Subs} = -\rho h\Gamma_{q_{\mathrm{l}}}\overline{w}(z_{\mathrm{i}}). \tag{3.12e}$$

Equations (3.12a)–(3.12e) allow for the evaluation of the relative contribution of each of the processes to the LWP tendency. Inserting typical values indicates for instance that the magnitude of the LWP tendency due to subsidence (about $5\,\mathrm{g\,m^{-2}\,h^{-1}}$) is about 9 times as small as that due to radiation. Table 3.1 gives an overview of the LWP tendencies induced by an increase of $1\,\mathrm{W\,m^{-2}}$ in the cloud base turbulent and entrainment fluxes as well as in the precipitation and radiation fluxes.

The entrainment term in Eq. (3.12a) is typically of similar magnitude as the radiative cooling term. The first two terms between the parentheses in Eq. (3.12a) represent cloud thinning tendencies due to entrainment drying and warming. The third term describes cloud thickening due to entrainment. Randall (1984) found that entrainment can result in net cloud thickening despite its cloud drying and warming effect. This "cloud deepening through entrainment" occurs only for deep

Table 3.1. Overview of the LWP tendency induced by a $1\,\mathrm{W\,m^{-2}}$ increase in the denoted variables.

Variable	$\partial\mathrm{LWP}/\partial t$ $(\mathrm{g\,m^{-2}\,h^{-1}})$
$\rho L_\mathrm{v}\overline{w'q_\mathrm{t}'}^\mathrm{b}$; $\rho L_\mathrm{v} w_\mathrm{e}\Delta q_\mathrm{t}$	0.60
$\rho c_p\overline{w'\theta_\mathrm{l}'}^\mathrm{b}$; $\rho c_p w_\mathrm{e}\Delta\theta_\mathrm{l}$; $-\rho c_p \delta F_\mathrm{rad}/\Pi$	-0.82
$\rho L_v \delta P$	-1.44

Table 3.2. An overview of the parameters and variables described in the text with the values used. These values are based on the DYCOMS-II case setup (Stevens et al., 2005b). The variables η and Γ_{q_l} are derived in the Appendix.

Parameters		
p^s	1017.8	hPa
T	283	K
h	200	m
z_i	800	m
$\rho c_p \delta F_\mathrm{rad}$	48	$\mathrm{W\,m^{-2}}$
$\rho L_\mathrm{v}\delta P$	0	$\mathrm{W\,m^{-2}}$
$\overline{w'\theta_\mathrm{l}'}^\mathrm{b}$	0	$\mathrm{K\,m\,s^{-1}}$
$\overline{w}(z_\mathrm{i})$	-3.0	$\mathrm{mm\,s^{-1}}$
A	1.3	

Derived variables		
ρ	1.13	$\mathrm{kg\,m^{-3}}$
q_s	8.2	$\mathrm{g\,kg^{-1}}$
$\gamma \equiv \dfrac{\partial q_\mathrm{s}}{\partial T} = \dfrac{L_\mathrm{v} q_\mathrm{s}}{R_\mathrm{v} T^2}$	0.55	$\mathrm{g\,kg^{-1}\,K^{-1}}$
$\eta \equiv \left(1 + \dfrac{L_\mathrm{v}\gamma}{c_p}\right)^{-1}$	0.42	
$\Gamma_{q_\mathrm{l}} = g\eta\left(\dfrac{q_\mathrm{s}}{R_\mathrm{d} T} - \dfrac{\gamma}{c_p}\right)$	-1.86	$\mathrm{g\,kg^{-1}\,km^{-1}}$

cloud layers (large h) and/or small inversion jumps $\Delta\theta_\mathrm{l}$ and $|\Delta q_\mathrm{t}|$. He introduced a variable X, which is similar to the term between parentheses in Eq. (3.12a), but only valid for a well-mixed boundary layer as it assumes that the entrainment drying and warming is spread over the entire depth of the boundary layer.

In order to assess how the LWP tendency due to entrainment depends on the inversion stability parameter κ, the definition in Eq. (3.1) is used to substitute the

humidity inversion jump Δq_t out of Eq. (3.12a), which gives:

$$\left.\frac{\partial \mathrm{LWP}}{\partial t}\right|_{\mathrm{Ent}} = \rho\eta w_e \left(\frac{c_p}{L_v}\frac{\Delta\theta_l}{\kappa - 1} - \Pi\gamma\Delta\theta_l - \frac{h\Gamma_{q_l}}{\eta}\right). \tag{3.13}$$

It is clear from this equation that the cloud thinning tendency due to entrainment becomes increasingly large as κ increases toward one. The magnitude of the two major cloud thickening processes: radiative cooling (Eq. 3.12c) and input of moisture at cloud base by turbulent fluxes (Eq. 3.12b), are limited by respectively the radiative divergence over the cloud layer $\delta F_{\mathrm{rad}} \lesssim 60\,\mathrm{W\,m^{-2}}$ and the surface latent heat flux, which is typically between 50 and $150\,\mathrm{W\,m^{-2}}$. The thinning tendency due to entrainment will therefore dominate the LWP tendency for large enough values of κ, such that the cloud layer will inevitably thin.

3.3 Discussion

3.3.1 LWP Tendency due to Entrainment

In order to arrive at a zero-order estimate of the LWP tendency due to entrainment, a qualitative relation for the entrainment rate is used (Stevens et al., 2005b):

$$w_e = A\frac{\delta F_{\mathrm{rad}}}{\Delta\theta_l}, \tag{3.14}$$

in which the entrainment efficiency A is of order unity. Typically, microphysical processes, the magnitude of the humidity inversion jump, surface turbulent fluxes and wind shear over the inversion have important effects on the entrainment efficiency via the buoyancy flux profile (Stevens, 2002). The value of A is therefore expected to vary significantly in space and time. Nevertheless, for illustrative purposes A is here treated as a constant.

Substitution of Eq. (3.14) into Eq. (3.13) gives:

$$\left.\frac{\partial \mathrm{LWP}}{\partial t}\right|_{\mathrm{Ent}} = \rho\eta A\delta F_{\mathrm{rad}} \left(\frac{c_p}{L_v}\frac{1}{\kappa - 1} - \Pi\gamma - \frac{h\Gamma_{q_l}}{\eta\Delta\theta_l}\right). \tag{3.15}$$

The inverse proportionality of the entrainment rate to the θ_l jump over the inversion causes the LWP tendency due to entrainment to be almost independent of $\Delta\theta_l$, as the third term on the rhs of Eq. (3.15) is relatively small compared to the other two.

Figure 3.2 shows the LWP tendency due to entrainment described by Eq. (3.15) as a function of κ for several values of $\Delta\theta_l$. Table 3.2 shows the parameters that were used for this plot. These parameters were chosen to match as closely as possible the setup of the second Dynamics and Chemistry of Marine Stratocumulus (DYCOMS-II) case (Stevens et al., 2003a, 2005b). This case is particularly interesting as it lies well within the original buoyancy reversal regime, yet the stratocumulus cloud layer is persistent in the observations (Stevens et al., 2003b). From the figure it is clear that the cloud thinning tendency due to entrainment increases rapidly with κ. For DYCOMS-II, $\kappa \approx 0.55$, such that this thinning tendency exceeds $-120\,\mathrm{g\,m^{-2}\,h^{-1}}$.

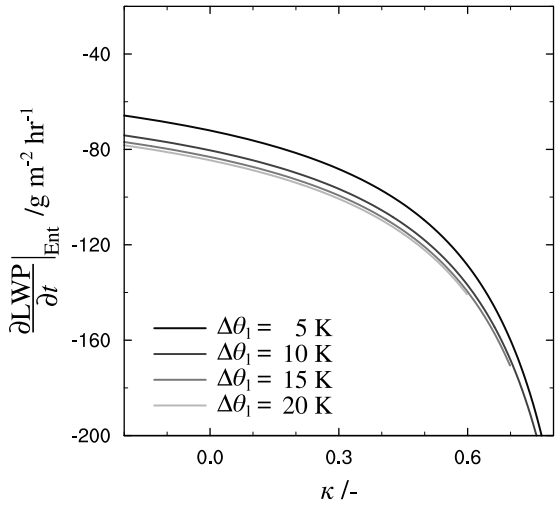

Figure 3.2. The contribution of entrainment to the LWP tendency as a function of κ, as given by Eq. (3.15) for a set of parameters chosen on the basis of the DYCOMS-II case (Stevens et al., 2005b).

This indicates that entrainment alone can dissolve the stratocumulus cloud in a matter of hours.

Note that the plot indeed shows that there is hardly any explicit dependence of the cloud thinning tendency on $\Delta\theta_\mathrm{l}$. Furthermore, the entrainment efficiency A and the radiative divergence over the cloud layer are simply coefficients to the tendency in Eq. (3.12a). Larger values will result in a stronger cloud thinning tendency and will shift the lines in Figure 3.2 downwards.

So far, only entrainment has been considered. In the next section, source terms for the LWP will also be considered in order to find the conditions for which a stratocumulus cloud layer will thin.

3.3.2 LWP Source Terms

A stratocumulus cloud layer can be maintained even under conditions with a strong thinning tendency due to entrainment, provided that the opposing cloud thickening processes are strong enough. In terms of Eqs. (3.12), the total LWP tendency is zero when

$$\mathrm{Ent} + \mathrm{Base} + \mathrm{Rad} + \mathrm{Prec} + \mathrm{Subs} = 0. \tag{3.16}$$

Straightforward substitution of all terms results in:

$$\begin{aligned} w_\mathrm{e}\left(\Delta q_\mathrm{t} - \Pi\gamma\Delta\theta_\mathrm{l}\right) + \overline{w'q'_\mathrm{t}}^{\,\mathrm{b}} - \Pi\gamma\overline{w'\theta'_\mathrm{l}}^{\,\mathrm{b}} + \\ \gamma\delta F_\mathrm{rad} - \frac{\delta P}{\eta} - \frac{h\Gamma_{q_\mathrm{l}}}{\eta}\left[w_\mathrm{e} + \overline{w}(z_\mathrm{i})\right] = 0. \end{aligned} \tag{3.17}$$

This equation can then easily be solved for Δq_t to give:

$$\Delta q_{\mathrm{t,eq}} = \Big[\gamma(\Pi A - 1)\delta F_\mathrm{rad} - \overline{w'q'_\mathrm{t}}^{\,\mathrm{b}} + \Pi\gamma\overline{w'\theta'_\mathrm{l}}^{\,\mathrm{b}} + \frac{\delta P}{\eta} + \frac{h\Gamma_{q_\mathrm{l}}}{\eta}\overline{w}(z_\mathrm{i})\Big]\frac{\Delta\theta_{\mathrm{l,eq}}}{A\delta F_\mathrm{rad}} + \frac{h\Gamma_{q_\mathrm{l}}}{\eta}, \tag{3.18}$$

where the entrainment relation of Eq. (3.14) has again been substituted. Equation (3.18) defines a pair of critical inversion jumps $\Delta q_{\mathrm{t,eq}}$ and $\Delta\theta_{\mathrm{l,eq}}$ for which the LWP of the stratocumulus layer is constant in time due to a balance of the sources and sinks. Figure 3.3 shows these pairs as a function of the latent heat flux at cloud base, again using the parameters in Table 3.2. Note that the precipitation rate is zero as it was not included in the original DYCOMS-II simulations. Furthermore $\overline{w'\theta'_\mathrm{l}}^{\,\mathrm{b}}$ is typically small and has therefore been neglected. For the area to the left of the equilibrium lines, the cloud layer is thinning due to additional entrainment drying and warming.

Figure 3.3 shows that, for a cloud base latent heat flux of $100\,\mathrm{W\,m^{-2}}$, the equilibrium condition given by Eq. (3.18) is similar to the buoyancy reversal criterion of Randall (1980) and Deardorff (1980a), which is shown in blue. However, Eq. (3.18) allows for the persistence of stratocumulus clouds beyond the original buoyancy reversal criterion line, depending on the magnitude of the source terms and is therefore in accord with the observations summarized by Kuo and Schubert (1988).

The black triangle marks the location of the DYCOMS-II case in the phase space. The latent heat flux for this case is almost constant with height at about $115\,\mathrm{W\,m^{-2}}$. According to this analysis, the cloud layer is thinning slowly. The rate at which it thins can be calculated using Eq. (3.12) and is about $-19\,\mathrm{g\,m^{-2}\,h^{-1}}$. The results shown in Figure 3.3, however, are significantly influenced by the entrainment efficiency parameter A. For a slightly lower value $A \approx 1.1$ (corresponding to a reduction of the entrainment velocity of only $1\,\mathrm{mm\,s^{-1}}$) the cloud layer would even be thickening. Similarly, a higher cloud base latent heat flux of about $150\,\mathrm{W\,m^{-2}}$ would provide enough moisture to the cloud layer to keep it from thinning.

In that respect, it is important to note that the analysis presented here is based on the instantaneous state of the cloud layer, which means that interactions among processes are not accounted for. As the LWP of the cloud layer changes as a result of a net tendency, radiative fluxes, precipitation and entrainment will change accordingly on a relatively short time scale. On a longer time scale the humidity flux at cloud base and the inversion jumps Δq_t and $\Delta\theta_\mathrm{l}$ will be affected. The goal of this discussion is therefore not to describe the temporal evolution of a stratocumulus cloud layer, but rather to show how the stratocumulus cloud thinning for sufficiently high values of κ can reasonably be expected from mere budget arguments.

To that end, the definition of κ in Eq. (3.1) is now used to substitute out $\Delta q_{T,\mathrm{eq}}$ from Eq. (3.18). This gives us an equilibrium κ value, beyond which the

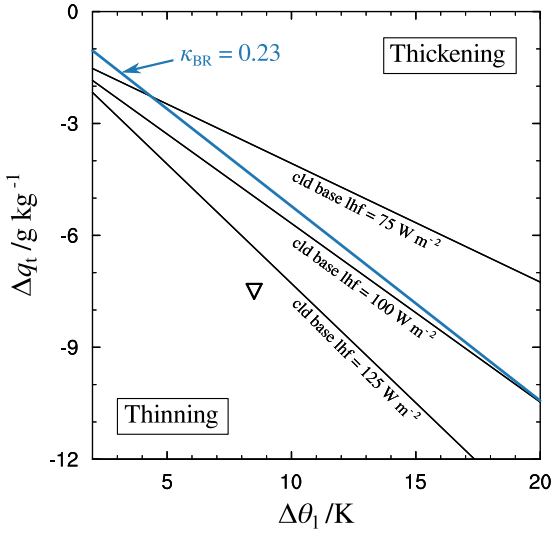

Figure 3.3. Plots of the equilibrium lines defined by Eq. 3.18, for three values of the surface latent heat fluxes: 75, 100 and 125 W m^{-2}. The blue line indicates the buoyancy reversal criterion formulated by Randall (1980) and Deardorff (1980a), $\kappa_{\mathrm{BR}} = 0.23$. The triangle marks the location in phase space of the DYCOMS-II case, for which the surface latent heat flux is about 115 W m^{-2}.

cloud layer is expected to thin. This κ_{eq} can be written as follows:

$$\kappa_{\mathrm{eq}} = 1 + \frac{c_p \delta F_{\mathrm{rad}} A}{L_{\mathrm{v}}} \left[\gamma(\Pi A - 1)\delta F_{\mathrm{rad}} - \overline{w'q_{\mathrm{t}}'}^{\,\mathrm{b}} + \Pi\gamma\overline{w'\theta_{\mathrm{l}}'}^{\,\mathrm{b}} + \frac{\delta P}{\eta} + \frac{h\Gamma_{q_{\mathrm{l}}}}{\eta}\left(\overline{w}(z_{\mathrm{i}}) + \frac{A\delta F_{\mathrm{rad}}}{\Delta\theta_{\mathrm{l}}}\right)\right]^{-1}. \tag{3.19}$$

In Figure 3.4, κ_{eq} is shown as a function of $\Delta\theta_{\mathrm{l}}$ for three different values of the cloud base latent heat flux. Clearly, κ_{eq} is higher for larger cloud base latent heat flux, while it is only a weak function of $\Delta\theta_{\mathrm{l}}$. This is in good agreement with the results of the LES experiments performed by Xiao et al. (2011), who found that for well-mixed boundary layers and hence a maximum moisture supply from the surface, the cloud layer breaks up at larger values of κ as compared to decoupled cases. It is also in qualitative agreement with the LES results of the stratocumulus transitions presented in Figure 3.1. The stratocumulus cloud layer in the ASTEX case breaks up for significantly smaller κ values than in the composite cases. The LWP budget analysis shows that this can reasonably be expected on the basis of the surface latent heat flux, which is on average about a factor of two smaller for ASTEX.

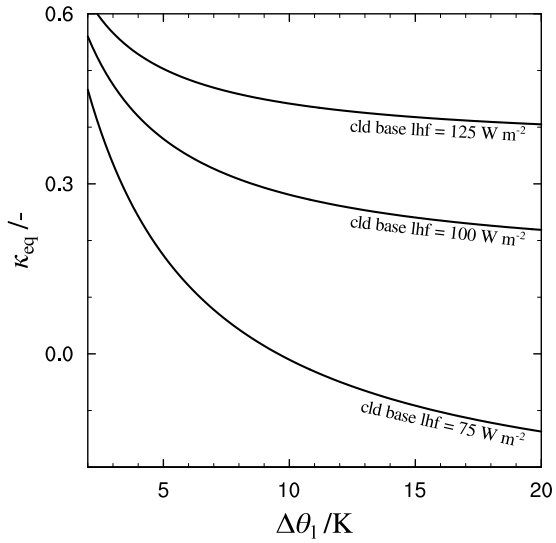

Figure 3.4. The equilibrium inversion stability parameter κ_{eq}, given by Eq. 3.19 for three values of the latent heat flux at cloud base: 75 W m^{-2}, 100 W m^{-2} and 125 W m^{-2}.

3.3.3 The Klein and Hartmann Line

From observations Klein and Hartmann (1993) found a strong correlation between the seasonally averaged lower tropospheric stability (LTS) and cloud cover in the main subtropical stratocumulus regions. The linear fit through the data points has become known as the Klein and Hartmann line and is described by:

$$\sigma = a\mathrm{LTS} + b, \tag{3.20}$$

in which σ is the cloud cover and $a = 5.7\,\mathrm{K}^{-1}$ and $b = -55.73$ are fitting constants. Chung et al. (2012) later qualitatively derived this relationship from a steady state, large-scale θ_l budget. Here, we express Eq. (3.20) as a function of κ in order to show some analogy with the results derived from LESs by Moeng (2000) and Lock (2009).

Assuming a constant θ lapse rate in the free atmosphere Γ_θ, the LTS can be related to the inversion jump of θ_l as follows:

$$\mathrm{LTS} = \Delta\theta_l - (z_{700} - z_i)\Gamma_\theta. \tag{3.21}$$

Here, $z_{700} \approx 3000\,\mathrm{m}$ is the height of the 700 hPa isobar. Substitution of Eqs. (3.1) and (3.21) into Eq. (3.20) results in the following relation between the cloud fraction σ and κ:

$$\sigma = \frac{aL_v}{c_p}(\kappa - 1)\Delta q_t - a\Gamma_\theta(z_{700} - z_i) + b. \tag{3.22}$$

Figure 3.5 shows σ as a function of κ, using $\Gamma_\theta = -6\,\mathrm{K\,km}^{-1}$ and $z_i = 800\,\mathrm{m}$. This figure shows that the seasonally averaged cloud cover decreases linearly with κ.

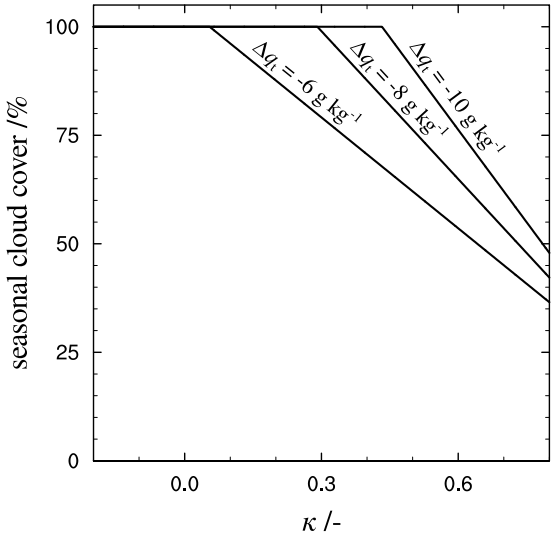

Figure 3.5. Seasonal cloud cover as a function of the inversion stability parameter κ based on the Klein and Hartmann line as described by Eq. (3.22), using $z_\mathrm{i} = 800\,\mathrm{m}$ and $\Gamma_\theta = -6\,\mathrm{K\,km^{-1}}$. The function is capped at $\sigma = 100\,\%$.

Interestingly, the cloud cover is qualitatively similar to those found from the LES process studies depicted in Figure 3.1 and by Lock (2009), despite the fact that the Klein and Hartmann line describes a fit through large area and seasonally averaged observations. However, whereas the Klein and Hartmann line describes the cloud cover as a function of the LTS only, the κ-analysis suggests that additionally the humidity jump Δq_t and the latent heat flux should be taken into account. An analysis of the correlation between the relative humidity in the free atmosphere and the cloud fraction from observations would therefore be very insightful.

3.4 Conclusions

In this article it is argued that the breakup of the subtropical marine stratocumulus clouds for high values of the inversion stability parameter κ can be satisfactorily explained using simple cloud layer budget arguments.

A budget equation was derived for the LWP of an adiabatic stratocumulus cloud layer, such that the contributions of the different physical mechanisms could be separately analyzed. Using a phenomenological entrainment relation, it is shown that the cloud thinning tendency due to entrainment increases rapidly with κ making cloud breakup inevitable for sufficiently large values of κ.

The conditions for which the cloud layer is neither thickening nor thinning could be found using the LWP tendency equation. This allowed us to define an equilibrium value of κ beyond which the cloud layer will thin. The value of κ_eq is mainly determined by the turbulence humidity flux at cloud base and the

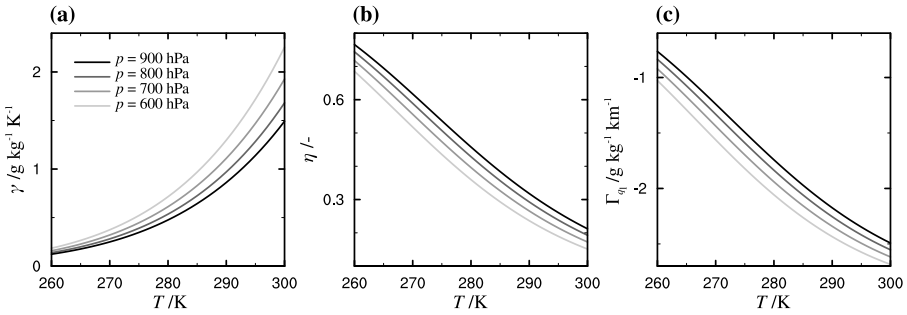

Figure 3.6. (a) The Clausius-Clapeyron relation γ, (b) η and (c) the liquid water specific humidity lapse rate Γ_{q_l} as a function of temperature for the pressures specified in the legend.

entrainment efficiency parameter A. The results are in a qualitative agreement with the findings of Xiao et al. (2011), who show that the κ value for which clouds start to break up are lower for decoupled as compared to well-mixed boundary layers.

Finally, it was shown that the linear relationship between the LTS and the cloud cover, found from observations by Klein and Hartmann (1993), also describes a cloud cover that decreases with κ.

Acknowledgements

The investigations were done as part of the European Union CLoud Intercomparison, Process Study & Evaluation (EUCLIPSE) project, funded under Framework Program 7 of the European Union. The work was sponsored by the National Computing Facilities Foundation (NCF) for the use of supercomputer facilities. We kindly thank Roel Neggers for stimulating discussions as well as Steef Böing and three anonymous reviewers for helpful comments on the manuscript.

Appendix 3.A Partial Derivatives of the Liquid Water Specific Humidity

Equation (3.2) contains partial derivatives of q_l with respect to q_t, θ_l and z_i. Below, expressions for each of these derivatives are derived.

3.A.1 Total Humidity

Firstly, the definition of θ_l is written in an incremental form:

$$\mathrm{d}\theta_\mathrm{l} = \mathrm{d}\theta - \frac{L_\mathrm{v}}{\Pi c_p}\mathrm{d}q_\mathrm{l}. \tag{3.23}$$

Now, because θ_l is kept constant, the lhs of Eq. (3.23) is zero, such that:

$$\mathrm{d}T = \frac{L_\mathrm{v}}{c_p}\mathrm{d}q_\mathrm{l}. \tag{3.24}$$

In a saturated environment, q_t can be written as the sum of the saturation specific humidity q_s and q_l, or, in its incremental form:

$$\mathrm{d}q_\mathrm{t} = \mathrm{d}q_\mathrm{s} + \mathrm{d}q_\mathrm{l}. \tag{3.25}$$

Equation (3.24) can now be used to substitute $\mathrm{d}q_\mathrm{l}$ out of this equation, giving:

$$\mathrm{d}q_\mathrm{t} = \mathrm{d}q_\mathrm{s} + \frac{c_p}{L_\mathrm{v}}\mathrm{d}T = \left(1 + \frac{c_p}{L_\mathrm{v}\gamma}\right)\mathrm{d}q_\mathrm{s}, \tag{3.26}$$

where γ is defined as:

$$\gamma \equiv \frac{\partial q_\mathrm{s}}{\partial T} = \frac{L_\mathrm{v} q_\mathrm{s}}{R_\mathrm{v} T^2}. \tag{3.27}$$

The second equality in Eq. (3.27) is given by the Clausius-Clapeyron relation. Figure 3.6a shows γ for a range of relevant temperatures and pressures. Using this expression to eliminate $\mathrm{d}q_\mathrm{s}$ in Eq. (3.25) and rearranging the terms gives:

$$\mathrm{d}q_\mathrm{t} = \left(\frac{L_\mathrm{v}\gamma}{c_p + L_\mathrm{v}\gamma}\right)\mathrm{d}q_\mathrm{t} + \mathrm{d}q_\mathrm{l}, \tag{3.28}$$

which can be solved for $\mathrm{d}q_\mathrm{t}$. The partial derivative can then be written as:

$$\frac{\partial q_\mathrm{l}}{\partial q_\mathrm{t}} = \eta, \tag{3.29}$$

in which:

$$\eta \equiv \left(1 + \frac{L_\mathrm{v}\gamma}{c_p}\right)^{-1}. \tag{3.30}$$

This η can be interpreted as an efficiency at which increments in q_t are converted to q_l. Figure 3.6b shows η as a function of temperature for different pressures.

3.A.2 Liquid Water Potential Temperature

For increments of θ, the following can be written:

$$\mathrm{d}\theta = \frac{\mathrm{d}T}{\Pi} = \frac{1}{\Pi}\frac{\partial T}{\partial q_\mathrm{s}}\mathrm{d}q_\mathrm{s}. \tag{3.31}$$

Furthermore, in a saturated environment at constant q_t:

$$\mathrm{d}q_\mathrm{s} = -\mathrm{d}q_\mathrm{l}. \tag{3.32}$$

Equations (3.31) and (3.32) can be used in Eq. (3.23) to give:

$$\mathrm{d}\theta_\mathrm{l} = -\frac{1}{\Pi}\left(\frac{1}{\gamma} + \frac{L_\mathrm{v}}{c_p}\right)\mathrm{d}q_\mathrm{l}. \tag{3.33}$$

The partial derivative of q_l with respect to θ_l can then be written as follows:

$$\frac{\partial q_\mathrm{l}}{\partial \theta_\mathrm{l}} = -\Pi\gamma\eta, \tag{3.34}$$

with η as defined by Eq. (3.30).

3.A.3 Inversion Height

In the cloud layer the following can be written for the lapse rate of the liquid water specific humidity Γ_{q_l}:

$$\Gamma_{q_\mathrm{l}} = -\frac{\partial q_\mathrm{l}}{\partial z} = \frac{\partial q_\mathrm{s}}{\partial z}. \tag{3.35}$$

Since $q_\mathrm{s} = f(T, p)$, partial differentiation can be used to write:

$$\Gamma_{q_\mathrm{l}} = \frac{\partial q_\mathrm{s}}{\partial z} = \frac{\partial q_\mathrm{s}}{\partial T}\frac{\partial T}{\partial z} + \frac{\partial q_\mathrm{s}}{\partial p}\frac{\partial p}{\partial z}. \tag{3.36}$$

Rewriting the first term gives:

$$\frac{\partial q_\mathrm{s}}{\partial T}\frac{\partial T}{\partial z} = -\gamma\Gamma_T \tag{3.37}$$

where Γ_T is the lapse rate of temperature. Since Eq. (3.36) should be evaluated incloud, Γ_T is equal to the saturated adiabatic lapse rate:

$$\Gamma_{T,\mathrm{s}} \approx \frac{g}{c_p} + \frac{L_\mathrm{v}}{c_p}\frac{\partial q_\mathrm{s}}{\partial z}, \tag{3.38}$$

in which q_v in the partial derivative has been replaced by q_s.
In order to rewrite the second term on the right hand side, q_s is approximated as follows (e.g. Stull, 1988):

$$q_\mathrm{s} \approx \frac{\varepsilon e_\mathrm{s}}{p}. \tag{3.39}$$

Here, e_s is the saturation pressure and $\varepsilon = R_\mathrm{d}/R_\mathrm{v} \approx 0.622$ is the ratio of the gas constant of dry air to that of water vapor. Differentiating this equation with respect to p results in:

$$\frac{\partial q_\mathrm{s}}{\partial p} = -\frac{q_\mathrm{s}}{p}. \tag{3.40}$$

The atmosphere is furthermore assumed to be in hydrostatic equilibrium:

$$\frac{\partial p}{\partial z} = -\rho g \approx -\frac{pg}{R_\mathrm{d}T}. \tag{3.41}$$

Substitution of Eqs. (3.37)-(3.41) into Eq. (3.36) gives:

$$\left(1 + \frac{\gamma L_\mathrm{v}}{c_p}\right)\frac{\partial q_\mathrm{s}}{\partial z} = -\frac{g\gamma}{c_p} + \frac{gq_\mathrm{s}}{R_\mathrm{d}T}, \tag{3.42}$$

such that after rewriting:

$$\Gamma_{q_\mathrm{l}} = g\eta\left(\frac{q_\mathrm{s}}{R_\mathrm{d}T} - \frac{\gamma}{c_p}\right). \tag{3.43}$$

The lapse rate is approximately $-1.8\,\mathrm{g\,kg^{-1}\,km^{-1}}$ in the relevant temperature and pressure range (see Figure 3.6c). As a result of mainly precipitation, stratocumulus clouds are typically subadiabatic (Wood, 2005). Equation (3.43) therefore gives an upper limit for magnitude of the lapse rate, which can in practice be up to 40 % smaller.

4

An LES model study of the influence of the free troposphere on the stratocumulus response to a climate perturbation

Twenty-five large-eddy simulations are performed to study how free tropospheric thermodynamic conditions control equilibrium state solutions of stratocumulus-topped marine boundary layers. In particular, we systematically vary the lower tropospheric stability (LTS) and a similar measure for the bulk humidity difference between the 700-hPa level and the surface, ΔQ. For all simulations, a completely overcast boundary layer is obtained in which the turbulence is mainly driven by cloud-top radiative cooling. The steady-state liquid water path (LWP) is rather insensitive to the LTS, but increases significantly and almost linearly with the free tropospheric humidity. In a second suite of runs, the response of the stratocumulus layer to an idealized global warming scenario is assessed by applying a uniform warming of 2 K to the initial temperature profile including the sea surface while the initial relative humidity profile is kept identical to the control case. The warming of the sea surface acts to increase the latent heat flux, which invigorates turbulence in the boundary layer. The steady-state inversion height therefore increases, despite the competing effect of a more humid free troposphere that increases the downwelling radiative flux and hence tends to decrease the entrainment rate. The stratocumulus layer nevertheless thins for all free tropospheric conditions as cloud base rises more than cloud top. This implies a positive stratocumulus cloud-climate feedback for this scenario as thinner clouds reflect less shortwave radiation back to space. The cloud thinning response to the climate perturbation is found to be mostly controlled by the change of ΔQ.

Published in *J. Adv. Model. Earth Syst.* (2015), with S.R. de Roode, S.Dal Gesso and A.P. Siebesma.

4.1 Introduction

Marine low clouds have a net cooling effect on the planet as they reflect more of the incoming solar radiation than the underlying sea surface, while their warming effect due to thermal radiation is small (Randall et al., 1984). This net cooling effect is strongest for stratocumulus clouds, because of their large cloud cover. Changes in the reflectivity and occurrence of stratocumulus as a result of climate change can therefore amplify or weaken global warming, which makes their accurate representation in climate models essential. However, the presence of stratocumulus clouds depends crucially on turbulence processes. Climate models use coarse resolutions and rely heavily on parameterization schemes to represent such turbulence processes. Therefore, they often fail to properly represent stratocumulus clouds (Williams and Webb, 2009; Nam et al., 2012; Teixeira et al., 2011). As a consequence, changes of their reflectivity and occurrence remain a major source of uncertainty in future climate projections (Bony and Dufresne, 2005; Soden and Held, 2006; Vial et al., 2013).

The response of low clouds to idealized climate perturbations has recently been investigated using large-eddy simulation (LES) models (e.g. Xu et al., 2010; Rieck et al., 2012; Bretherton and Blossey, 2014). Most of the turbulent transport in the atmospheric boundary layer is explicitly resolved in such models, making them suitable for the accurate representation of low clouds. A particularly relevant LES study was performed as part of the CGILS (Cloud Feedback Model Intercomparison Project/Global Atmospheric System Study Intercomparison of Large-Eddy and Single-Column Models) project. Idealized cases were designed for the simulation of three low cloud types that are climatologically prevailing over subtropical oceans, namely stratocumulus, cumulus-under-stratocumulus and trade cumulus (Blossey et al., 2013). To determine the cloud response to an idealized climate perturbation, the initial temperature was uniformly increased by 2 K. The total specific humidity was furthermore increased, assuming that large-scale processes act to keep the initial relative humidity profile the same as for the control case. This perturbation caused a decrease of the domain averaged LWP for the stratocumulus case. In a second experiment, the large-scale subsidence velocity was decreased in addition to the warming perturbation to mimic a weakening of the Hadley circulation. The cloud thickening effect due to the decreased subsidence velocity overcompensated the decrease of the LWP in most LES models, resulting in a small net increase of the LWP (Blossey et al., 2013; Bretherton et al., 2013). The simulations were also run with several single-column model (SCM) versions of climate models. The cloud responses found from the SCMs strongly varied and both positive and negative cloud feedbacks were found (Zhang et al., 2013).

Dal Gesso et al. (2014b, hereafter DG14a) extended the CGILS cumulus-under-stratocumulus case by considering a phase space spanned by a range of lower-tropospheric stabilities (LTSs) and free-tropospheric humidities. This setup was motivated by among others Klein and Hartmann (1993), who showed that there is a strong correlation between the observed seasonally averaged LTS and low cloud amount, as well as by the strong dependence of the entrainment rate and the LWP of stratocumulus clouds on the free tropospheric humidity (e.g. Chlond and Wolkau, 2000; Ackerman et al., 2004; Lock, 2009). Using a mixed-layer

model (MLM), DG14a showed that the LWP in a steady state increases as the humidity in the free troposphere decreases or as the LTS decreases. Analogous to the CGILS experiment, a second set of simulations was performed for which the temperature was increased while the initial relative humidity profile was kept constant. The large-scale subsidence velocity was not perturbed to allow for a more straightforward interpretation of the results. The cloud layer thinned in response to this perturbation for virtually all cases and the thinning was found to be strongest for dry and relatively warm free tropospheric conditions. The thinning response was caused by the combination of, in the first place, an increased cloud base height caused by the warming of the boundary layer and in the second place, a decreased cloud top height, which could be explained by a smaller entrainment rate as a result of a reduced forcing in terms of the longwave radiative cooling near the cloud top. The latter is due to a larger free tropospheric specific humidity which will tend to increase the atmospheric emissivity, thereby diminishing the longwave radiative jump across the cloud top.

The cases described by DG14a were run with a SCM version of EC-Earth (Hazeleger et al., 2010) in a follow-up study by Dal Gesso et al. (2014a, hereafter DG14b) to evaluate how accurately the stratocumulus steady states are represented by the parameterization schemes used in this model. Besides stratocumulus, shallow cumulus solutions were found for low LTS and for a relatively dry free troposphere. When averaged over all cases, a positive cloud-climate feedback was found from the SCM results, which is in accord with the MLM study by DG14a. However, the magnitude and even the sign of the cloud feedback changed irregularly from case to case, thereby emphasizing the importance of the phase space setup. This lack of coherence among the SCM simulations prohibited a careful analysis of the mechanisms responsible for the positive cloud response.

In MLMs and SCMs, turbulent transport is calculated from parameterization schemes. By contrast, LES models do not suffer from this limitation as they explicitly resolve the eddies that perform the bulk of the turbulent transport. Furthermore, the effects of processes like latent heat release and longwave radiative cooling on the entrainment rate are typically much better represented. Since the entrainment rate is key to the equilibrium state solutions of the stratocumulus-topped boundary layer (De Roode et al., 2014), this has motivated us to repeat the experiments performed by DG14a and DG14b with an LES model. The present study discusses how equilibrium states of the stratocumulus-topped boundary layer are affected by the free tropospheric conditions, and how the stratocumulus cloud amount changes under an idealized global warming scenario. In a companion paper by Dal Gesso et al. (2015) the results of an SCM intercomparison are discussed and compared to the LES model results in detail. Although the use of LES constitutes an important step forward from MLMs and SCMs, it should be noted that entrainment is governed by mixing processes at scales much smaller than the LES grid spacing (e.g. Mellado et al., 2013). Hence, higher resolution LES or even direct numerical simulation is required to explicitly resolve this mixing, which is currently beyond the reach of the available computational resources.

The following section describes the most relevant aspects of the case setup and the climate perturbation that was applied. The results of the control climate simulations are described in Section 4.3, while the response to the idealized climate

perturbation is discussed in Section 4.4. Section 4.5 contains some discussion and a summary of the main conclusions is given in Section 4.6.

4.2 Setup

4.2.1 Case Specifications

DG14a developed a framework based on stratocumulus conditions in the North-East Pacific, within which the liquid water potential temperature θ_l and the total water specific humidity q_t in the free troposphere were varied to investigate their effect on the boundary layer structure in a steady state. Each case is identified by the LTS in combination with a similar variable, ΔQ, that measures the difference between the free tropospheric specific humidity and the saturation specific humidity q_s at the surface:

$$\mathrm{LTS} = \theta_{\mathrm{l,ft}} - \theta_\mathrm{l}(T_0, p_0), \tag{4.1}$$

$$\Delta Q = q_{\mathrm{t,ft}} - q_\mathrm{s}(T_0, p_0). \tag{4.2}$$

Here, the subscripted 'ft' denotes the value of a variable at the 700 hPa level, which corresponds to a height of approximately 3 km. The subscripted '0' indicates the value at the surface. The sea surface temperature T_0 and pressure p_0 are constant, while $\theta_{\mathrm{l,ft}}$ and $q_{\mathrm{t,ft}}$ are nudged toward their initial values. The LTS and ΔQ are therefore constant in time for every simulation.

In the current work a set of 25 LESs is performed that includes all combinations of

$$\begin{aligned} \mathrm{LTS} \in &\quad \{18.1, 20.1, 22.1, 24.1, 26.1\} \quad \mathrm{K}, \\ \Delta Q \in &\{-9.8, -8.8, -7.8, -6.8, -5.8\} \quad \mathrm{g\,kg^{-1}}. \end{aligned}$$

All simulations are run for ten days to an approximate steady state, which is only achieved when for a conserved variable $\varphi \in \{q_\mathrm{t}, \theta_\mathrm{l}\}$ the following budget equation is satisfied:

$$-\overline{u}_j \frac{\partial \overline{\varphi}}{\partial x_j} - \frac{\partial \overline{w'\varphi'}}{\partial z} - \overline{w}\frac{\partial \overline{\varphi}}{\partial z} + \overline{S}_\varphi = 0. \tag{4.3}$$

Here, $\overline{u}_j$ denotes the large-scale horizontal wind components, z is the height, $\overline{w'\varphi'}$ is the vertical turbulent flux of φ and $\overline{S}_\varphi$ accounts for the diabatic sources and sinks due to precipitation and radiation. Furthermore, $\partial\overline{\varphi}/\partial x_j$ denotes the large-scale horizontal gradients of φ, which are assumed to be zero in this study. The large-scale horizontal advection term therefore does not contribute to the heat and moisture budgets, despite the non-zero mean horizontal wind velocity. More specifically, the y-coordinate of the domain is aligned with the mean wind, which is constant with height at an initial velocity of $-6.74\,\mathrm{m\,s^{-1}}$ and is equal to the geostrophic wind. For notational convenience the overbars indicating horizontal averaging are omitted for all variables except for turbulent fluxes and the subsidence velocity $\overline{w}$ in the remainder of the article.

In the quiescent free troposphere, turbulent fluxes are negligibly small hence Eq. (4.3) can be simplified as:

$$\overline{w}\frac{\partial \varphi}{\partial z} = S_{\varphi}. \tag{4.4}$$

DG14b assumed the temperature lapse rate in the free troposphere to follow the moist adiabat, which determines the vertical gradient of θ_l. The subsidence profile

$$\overline{w}(z) = w_0 \left(1 - e^{-z/z_w}\right), \tag{4.5}$$

is chosen such that the diabatic cooling due to radiation approximately balances subsidence warming (Bellon and Stevens, 2012). Here, $w_0 = -3.5\,\mathrm{mm\,s^{-1}}$ is the value to which $\overline{w}$ saturates at heights that are large with respect to the scale height $z_w = 500\,\mathrm{m}$. For q_t on the other hand, in the absence of horizontal advection there are no diabatic terms in the free troposphere. Equation (4.4) can therefore only be satisfied if the subsidence term is zero, which is achieved by setting q_t constant with height up to 3 km. For CGILS, q_t decreased with height above 2 km. The ΔQ values of the CGILS cases are therefore quite large as compared to the range considered here, at (LTS, ΔQ) = (22.4 K, $-11\,\mathrm{g\,kg^{-1}}$) and (25.4 K, $-9.5\,\mathrm{g\,kg^{-1}}$) for the cumulus-under-stratocumulus and the stratocumulus case, respectively (Blossey et al., 2013).

All other boundary conditions and forcings, such as the surface temperature and pressure of the control simulations as well as the diurnally averaged solar zenith angle (52°) and the downwelling solar radiative flux at the top of the atmosphere ($765.84\,\mathrm{W\,m^{-2}}$) are equal to those prescribed for the S11 case (Blossey et al., 2013). The information and initial profiles required to perform the simulations are available online (http://www.euclipse.nl/wp3/SteadyStates/main.shtml).

4.2.2 Idealized Climate Perturbation

In addition to the control climate simulations, a second set of simulations is performed in which the temperature of the atmospheric column as well as the sea surface temperature are uniformly increased by 2 K, thereby keeping the LTS the same as in the control climate. The total specific humidity is furthermore increased to keep the initial relative humidity profile identical to that of the control case. As the saturation specific humidity q_s is a convex function of the temperature, the increase of q_t at the surface is typically larger than in the cooler free troposphere. The assumption of a constant relative humidity $\mathcal{H} = q_t/q_s$ in a perturbed climate therefore imposes a change in the bulk jump of the total specific humidity ΔQ, whose magnitude can be derived by first writing the increase of q_t with temperature at any height as follows

$$\frac{\partial q_t}{\partial T} = \mathcal{H}\frac{\partial q_s}{\partial T} = \mathcal{H}\frac{L_v q_s}{R_v T^2}. \tag{4.6}$$

Here, R_v is the specific gas constant for water vapor and L_v is the latent heat of vaporization. Using this equation with Eq. (4.2) gives

$$\frac{\partial}{\partial T}(\Delta Q) = \frac{L_v}{R_v}\left\{\mathcal{H}_{ft}\frac{q_s(T_{ft}, p_{ft})}{T_{ft}^2} - \frac{q_s(T_0, p_0)}{T_0^2}\right\}, \tag{4.7}$$

from which it can be shown that ΔQ changes throughout the phase space by between $-0.4\,\mathrm{g\,kg^{-1}\,K^{-1}}$ for humid and $-0.7\,\mathrm{g\,kg^{-1}\,K^{-1}}$ for relatively dry free tropospheric conditions.

4.2.3 Model Configuration

The Dutch Atmospheric Large-Eddy Simulation (DALES 4.0, Heus et al., 2010; Böing et al., 2012) model is used in a Boussinesq mode by specifying a base state density that is constant with height in the momentum equations. A hybrid of a fifth-order upwind scheme (e.g. Wicker and Skamarock, 2002) and a fifth-order weighted essentially non-oscillatory advection scheme (Jiang and Shu, 1996; Blossey and Durran, 2008) is used for the advection of scalars in order to avoid spurious overshoots at the inversion. These overshoots were hypothesized to influence the magnitude of the response of the LWP to the warming perturbation in the LES model intercomparison of the CGILS S12 stratocumulus case (Blossey et al., 2013).

The warm-rain microphysics model of Kogan (2013) is used for the parameterization of autoconversion, accretion, self-collection and evaporation processes as well as to determine the sedimentation velocities of rain water specific humidity q_r and rain droplet number concentration N_r. A piecewise-linear semi-Lagrangian advection scheme is used for the sedimentation of q_r and N_r (Juang and Hong, 2009). The cloud droplet number concentration is set to a constant value of $100\,\mathrm{cm^{-3}}$ wherever the liquid water specific humidity $q_\mathrm{l} > 0$ and the effect of cloud droplet sedimentation is accounted for using the parameterization of Ackerman et al. (2009).

Longwave and shortwave radiative fluxes are parameterized using the Rapid Radiative Transfer Model for General Circulation Models (RRTMG, Iacono et al., 2008), for which a convenient interface was provided by Peter Blossey (Blossey et al., 2013). The radiation calculations are performed once every 120 seconds. Following Ackerman et al. (2009), the effects of having a non-monodisperse cloud droplet size distribution are accounted for in the calculation of the effective radius, which is the ratio of the third to the second moment of the droplet size distribution.

Surface fluxes of θ_l and q_t are calculated interactively, using a constant surface roughness length $z_0 = 0.2\,\mathrm{mm}$. With the exception of the surface scheme, the model configuration is identical to that used for the second phase of the CGILS experiment. Preliminary inspection of the results shows that all participating models respond similarly to the climate perturbations (Peter Blossey, personal communication, 2014). It is therefore likely that the results from the simulations presented below are representative for the general behavior of LES models, although the quantitative results may differ.

4.2.4 Domain Specifications

The vertical spacing of the numerical grid is 10 m up to a height of 1.8 km, above which it is increased by 5 % per level. The 3 km high domain is therefore made up of a total of 219 levels. At the top of the domain θ_l and q_t are relaxed toward their initial values to mimic the nudging toward the initial conditions that was used above 3 km height for the SCM simulations performed by DG14b.

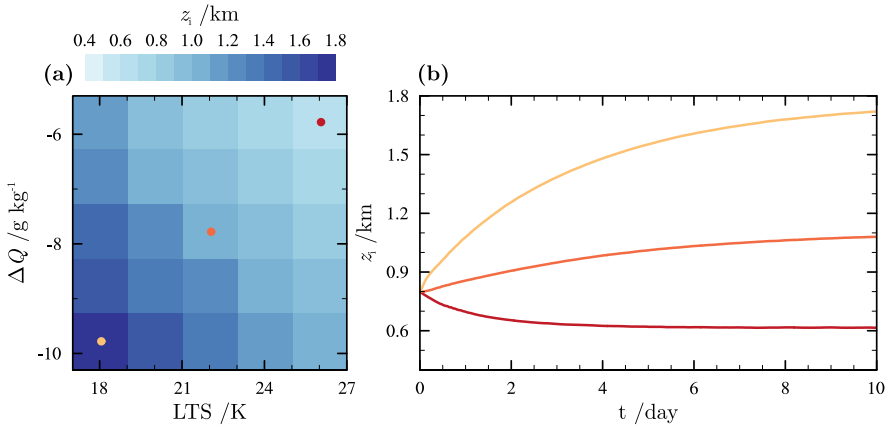

Figure 4.1. (a) The inversion height z_i in km averaged over the tenth day for 25 simulations in a phase space spanned by the LTS $= \theta_{l,ft} - \theta_{l,0}$ and by $\Delta Q = q_{t,ft} - q_{s,0}$. (b) Time series of the inversion height for the three selected simulations that are indicated by the colored circles in (a).

Note that the vertical resolution is coarser than the ≤ 5 m resolutions that are recommended to properly resolve the small scale mixing in the inversion layer of stratocumulus-topped boundary layers (e.g. Bretherton et al., 1999b; Stevens et al., 1999; Yamaguchi and Randall, 2012). However, the long integration time of ten days and the large number of simulations that are performed make the study presented here computationally demanding. Using a coarser vertical resolution of 10 m decreases the computational cost by approximately a factor of four as compared to a 5 m resolution. The sensitivity tests described in Appendix 4.A indicate that the use of finer resolutions will yield very similar results in terms of for instance the inversion height. The LWP, on the other hand, can be expected to increase by about 25 % when the resolution is increased from 10 to 5 m.

In both horizontal directions, the domain consists of 120 grid points that are spaced 50 m apart. This results in a horizontal domain size of 6×6 km^2, which is comparable to or somewhat larger than the domains used in other recent stratocumulus studies (Ackerman et al., 2009; Chung et al., 2012; Van der Dussen et al., 2013; Blossey et al., 2013). Sandu and Stevens (2011) performed several simulations of stratocumulus transitions on a domain of approximately 9×9 km^2 and found that among others cloud cover and albedo differed by less than 5 % from smaller 4.5×4.5 km^2 simulations for weakly precipitating cases. Based on these considerations, the domain used is assumed to be sufficiently large for the purposes of the present study.

4.3 Control Climate

4.3.1 Inversion Height

Figure 4.1a shows the inversion height z_i as a function of ΔQ and LTS. The results in this plot and in the remainder of this study are averages over the tenth day of the simulations, unless stated otherwise. Note that the data presented in this and the following section is included in NetCDF format as supplementary material S1 and S2 for the control and the perturbed climate simulations respectively. For all free tropospheric conditions, a cloud cover of unity is maintained for the entire duration of the simulations. Figure 4.1b shows timeseries of z_i for the three simulations indicated by the colored circles in Figure 4.1a, from which it is clear that the boundary layer height is close to a steady state at the end of the ten-day integration time. Note that z_i is a proxy for the entrainment rate w_e, as in a steady state

$$w_e = -\overline{w}(z_i). \tag{4.8}$$

The entrainment rate can be expected to increase as the stability of the inversion as measured by $\Delta\theta_v$, the jump of the virtual potential temperature over the inversion, decreases. The virtual potential temperature can be written as:

$$\theta_v = \theta(1 + \epsilon_I q_v - q_l), \tag{4.9}$$

in which q_v is the water vapor specific humidity and θ is the potential temperature. Furthermore, the constant $\epsilon_I = R_v/R_d - 1 \approx 0.61$, where R_d is the specific gas constant for dry air. In the free troposphere, the air is subsaturated, such that

$$\theta_{v,ft} = \theta_{l,ft}(1 + \epsilon_I q_{t,ft}). \tag{4.10}$$

According to this equation, a decrease of $\theta_{l,ft}$ (or similarly of the LTS) of 1 K results in an decrease of $\theta_{v,ft}$ of approximately 1 K. Such a decrease weakens the inversion stability and hence causes an increase of the inversion height, which is also obvious in Figure 4.1a.

From Eq. (4.10) it can furthermore be seen that the presence of humidity in the free troposphere decreases $\theta_{v,ft}$ and hence weakens the inversion. A drying of the free troposphere by 1 g kg^{-1} causes a decrease of $\theta_{v,ft}$ of approximately 0.2 K. Figure 4.1a indeed shows that z_i increases for drier free tropospheric conditions as measured by more negative values of the bulk humidity jump ΔQ, whose variations are solely due to the variation of $q_{t,ft}$ as the sea surface temperature is identical for all simulations. However, the z_i increase due to a ΔQ change of 1 g kg^{-1} is approximately as large as that due to an LTS decrease of 2 K, which is much larger than is expected on the virtual effect of water vapor alone. The z_i sensitivity to $q_{t,ft}$ found from the simulations is therefore about ten times stronger than expected on the basis of the virtual effect of water vapor alone.

This strong dependency of z_i on the free tropospheric humidity can be explained as follows. In the first place, for drier free tropospheric conditions the effect of cloud droplet evaporative cooling due to entrainment and the subsequent mixing of free tropospheric air into the cloud layer will be stronger. A drier free troposphere therefore effectively weakens the inversion stability, which supports

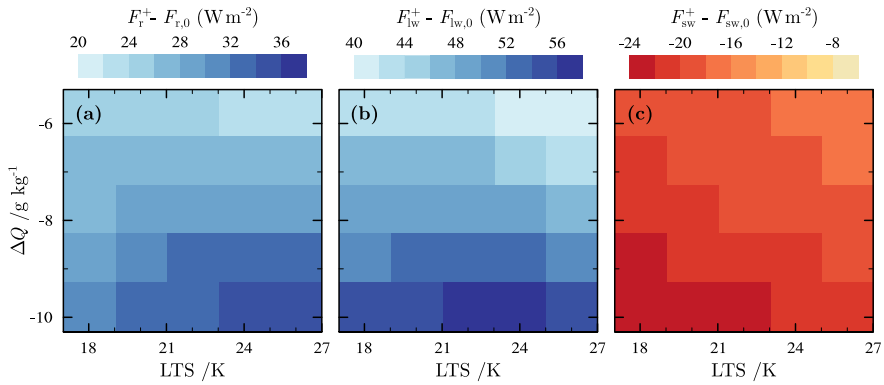

Figure 4.2. As Figure 4.1a, but for (a) the total radiative flux divergence over the boundary layer, $F_r^+ - F_{r,0}$, that is split into contributions from (b) longwave F_{lw} and (c) shortwave radiation F_{sw}. Blue and red colors indicate cooling and warming tendencies of the boundary layer, respectively.

larger entrainment rates for larger values of ΔQ (e.g. Nicholls and Turton, 1986; Chlond and Wolkau, 2000; Yamaguchi and Randall, 2008).

Second, a moister free troposphere generally emits more longwave radiation. More specifically, it is found that the downwelling longwave radiation increases logarithmically with the water vapor path W (e.g. Zhang et al., 2001):

$$W = \int_{z=0}^{\infty} \rho_a q_v \mathrm{d}z', \tag{4.11}$$

where ρ_a is the density of air. The stratocumulus cloud absorbs this downwelling radiation, which partly offsets the cooling tendency that is due to the longwave radiation it emits.

Figure 4.2a shows the difference between the net radiative flux F_r directly above the inversion, indicated by a '+', and at the surface. This total flux is divided into its longwave and shortwave contributions as shown in Figures 4.2b and 4.2c, respectively. The sign convention is such that downwelling fluxes are negative. The positive values in Figure 4.2a indicate a net cooling of the boundary layer by radiative processes, because

$$\rho_a c_p \frac{\partial \theta_{l,bl}}{\partial t}\bigg|_{rad} = -\frac{F_r^+ - F_{r,0}}{z_i}. \tag{4.12}$$

Here, c_p is the specific heat of air at constant pressure and $\theta_{l,bl}$ denotes the boundary layer averaged value of θ_l. It is clear from Figure 4.2a that the net cooling in the boundary layer indeed increases as the free troposphere becomes drier. The longwave radiative cooling is predominantly confined to the top of the stratocumulus layer, which destabilizes this layer and promotes the production of turbulence. As a consequence a larger difference between F_r^+ and $F_{r,0}$ tends to increase the entrainment rate (Moeng, 2000; Christensen et al., 2013).

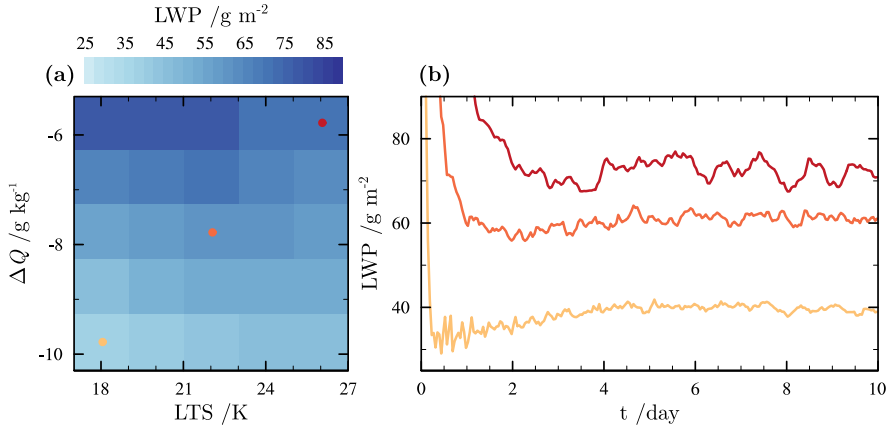

Figure 4.3. As Figure 4.1, but for the LWP in $\mathrm{g\,m^{-2}}$. The boundary layer is initialized with well-mixed q_t and θ_l profiles, resulting in a relatively large initial LWP of about $300\,\mathrm{g\,m^{-2}}$.

Note that in the current setup q_t is constant with height in the lower part of the free troposphere. Given the fact that the downwelling longwave radiation received at the top of the cloud layer increases for larger water vapor paths aloft it can therefore be expected that the dependency of z_i on the free tropospheric humidity may be somewhat weaker if the specific humidity in the free troposphere decreases with height.

The steady-state inversion height in Figure 4.1a varies between 0.4 and 1.8 km. The MLM results of DG14a show a similar range and dependency on the free tropospheric thermodynamic conditions. This indicates that the Nicholls and Turton (1986) entrainment parameterization that was used in the MLM of DG14a realistically represents the dependency of the entrainment velocity on the inversion strength, evaporative cooling and the downwelling longwave radiative flux at the inversion. The SCM used by DG14b, on the other hand, is too insensitive to variations in the free tropospheric conditions and as a consequence it underestimates the inversion height by up to 1000 m for the warm and dry free troposphere regime.

From MLM simulations, De Roode et al. (2014) found stratocumulus cloud deepening in combination with an increased entrainment rate in the relatively moist and cold free troposphere regime. This so-called cloud deepening through entrainment (Randall, 1984) is not found to take place in the LES results, which is likely due to the decoupling of the boundary layer that is discussed below.

4.3.2 Liquid Water Path

Figure 4.3a shows the steady-state LWP, which ranges between approximately 40 and $80\,\mathrm{g\,m^{-2}}$. The timeseries of the LWP in Figure 4.3b show that a steady state is achieved after only a few days, which is somewhat faster than for the inversion height (Figure 4.1b). Similar results are found from LESs by Bretherton et al. (2010). They argued that this is a manifestation of the separation of the short

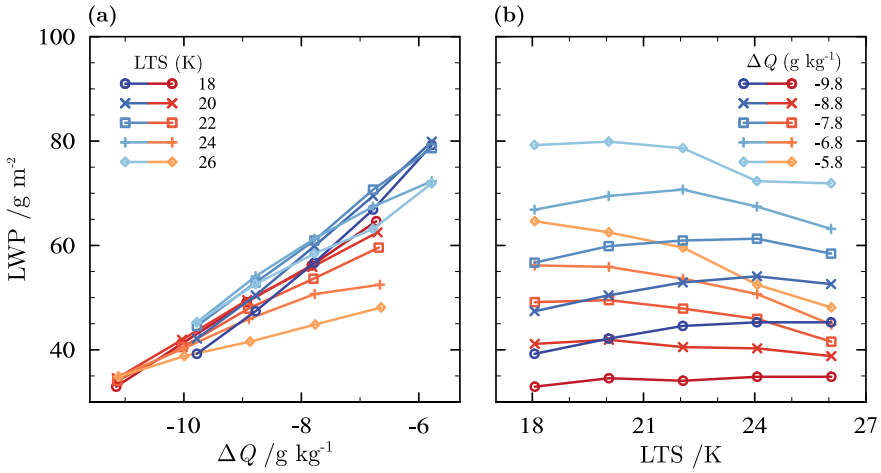

Figure 4.4. The LWP in $\mathrm{g\,m^{-2}}$ as a function of (a) the total specific humidity difference between the free troposphere and the surface ΔQ and (b) the lower tropospheric stability LTS. Blue and red colors indicate the control and the perturbed climate simulations respectively and the symbols indicate the different values of (a) the LTS and (b) ΔQ as shown in the legends.

thermodynamic time scale, which is of the order of a day, and the much longer dynamical timescale that is related to the large-scale subsidence velocity and can be up to four days (see e.g. Schubert et al., 1979; Jones et al., 2014). Once a thermodynamic quasi-steady state is achieved, changes to the inversion height are accompanied by almost equal changes of stratocumulus base height. The slow evolution of z_i in the second half of the simulations therefore hardly influences the LWP.

The LWP variations around the steady state are typically less than $5\,\mathrm{g\,m^{-2}}$, which is small as compared to the LWP differences among the cases, indicating that the spread in the LWP that is visible in Figure 4.3a is significant.

The LWP is too low to support significant rain formation. The precipitation rates are therefore low at $< 0.2\,\mathrm{W\,m^{-2}}$ for all cases, so that the effect of precipitation on the budgets of q_t and θ_l is negligible.

From Figure 4.3a it can be seen that the LWP is predominantly controlled by ΔQ and to a much lesser extent by the LTS. This is more clearly shown in Figures 4.4a and 4.4b, which show the steady-state LWP as a function of ΔQ and LTS, respectively. This sensitivity of the stratocumulus LWP to variations of the free tropospheric humidity has been recognized before (Chlond and Wolkau, 2000; Ackerman et al., 2004; Lock, 2009; Van der Dussen et al., 2014).

Figures 4.5a and 4.5b show that in roughly the top half of the boundary layer q_t is almost constant with height as a result of the mixing induced by the net radiative cooling at the top of the stratocumulus layer. This mixing causes the profiles of q_l to be close to adiabatic, as is shown in Figure 4.5c. Interestingly, the actual stratocumulus layer is thin as compared to the depth of the well-mixed

upper part of the boundary layer. For instance, the stratocumulus layer is about 250 m thick for the deepest case depicted by the yellow lines, while q_t is well mixed over a depth of over 1000 m. Figure 4.5d shows that the cloud fraction below the stratocumulus layer is zero and hence there is no sign of cumulus updrafts that often occur underneath stratocumulus clouds in relatively deep marine boundary layers (Bretherton and Pincus, 1995; Wood, 2012).

For the deepest cases, the stratocumulus layer is significantly drier than the surface layer, a feature which is commonly found from observations (Nicholls and Leighton, 1986; Albrecht et al., 1995; Park et al., 2004; Wood and Bretherton, 2004) and is referred to as decoupling. This two-layer structure can obviously not be represented by an MLM. If the stratocumulus-topped boundary layer deviates from a well-mixed situation, the stratocumulus layer will typically have a higher θ_l and a lower q_t than the subcloud layer, which both act to reduce the cloud liquid water content. DG14a showed that in the MLM a decrease of the free tropospheric specific humidity causes the stratocumulus layer to thicken, which due to an increase of the steady-state inversion height. The enhanced drying accompanying the increase entrainment rate is uniformly spread over the boundary layer and is therefore relatively small in the cloud layer. From the LES results we find a thinning of the stratocumulus layer when the free tropospheric specific humidity decreases, which is opposite to the response of the MLM. This is likely the result of the decoupling of the boundary layer, which causes the enhanced drying accompanying an increased entrainment rate to be mostly confined to the stratocumulus layer. Therefore, the cloud thinning due to enhanced entrainment drying dominates the response of the decoupled stratocumulus-topped boundary layer to a reduction of the free tropospheric humidity in the LES results.

The SCM results of DG14b also indicate an increase of the LWP for larger ΔQ values for those cases that are completely overcast. In the previous section it was noted that the boundary layer in the SCM results was too shallow in general and that the inversion height was less sensitive to changes in the free tropospheric conditions as compared to the LES results. The boundary layers in the SCM simulations are therefore rather well mixed. Similar to the MLM results, this likely explains the discrepancy between the LES and SCM in terms of dependence of the LWP on the free tropospheric humidity.

4.3.3 Surface Fluxes

Figure 4.6a shows the buoyancy flux $\overline{w'\theta_v'}$ at the surface, which is found to be small at, on average, $1\,\mathrm{W\,m^{-2}}$. Negative surface buoyancy fluxes are found for relatively humid and warm free tropospheric conditions.

In the subcloud layer, the virtual potential temperature flux can be expressed as a linear combination of the fluxes of θ_l and q_t as follows:

$$\overline{w'\theta_v'} = (1 + \epsilon_I q_t)\,\overline{w'\theta_l'} + \epsilon_I \theta \overline{w'q_t'}. \tag{4.13}$$

Figure 4.6b shows that the sensible heat flux is negative for all free tropospheric conditions, which is the main cause of the low surface buoyancy flux. From Eq. (4.13) it can be seen that the contribution of the surface latent heat flux to the surface buoyancy flux is small. Furthermore, the surface latent heat flux is found

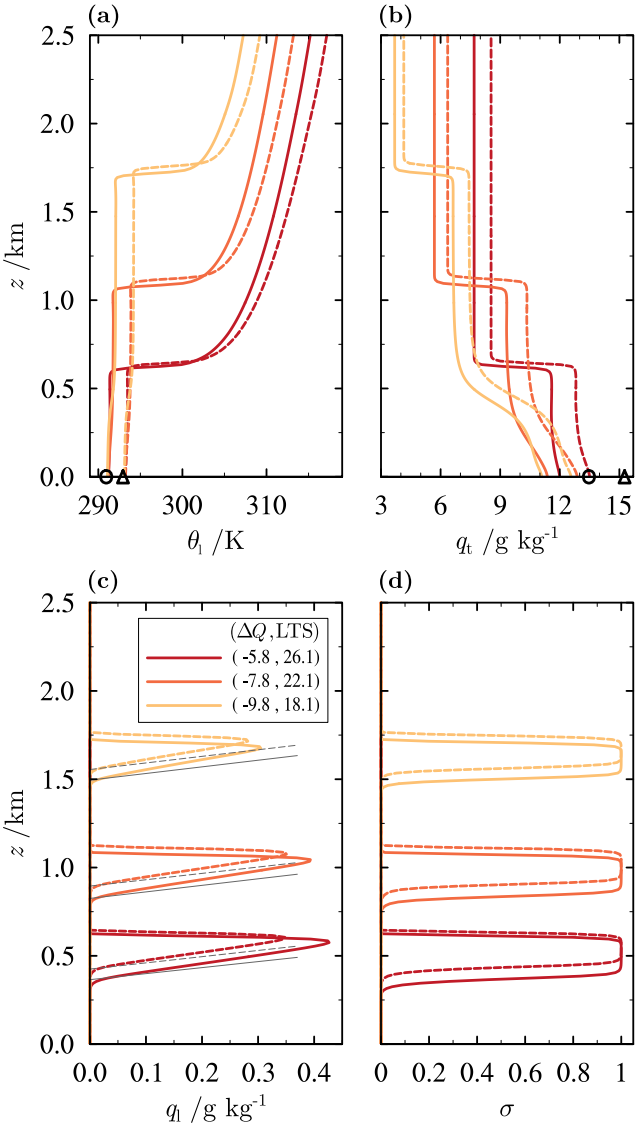

Figure 4.5. Vertical profiles of (a) liquid water potential temperature θ_l, (b) total specific humidity q_t, (c) liquid water specific humidity q_l and (d) cloud fraction σ averaged over the tenth day of the simulations. The legend indicates the values of ΔQ and the LTS for each of the cases and the locations in the phase space are indicated by the correspondingly colored dots in Figures 4.1a and 4.3a. The solid and dashed lines show the control and perturbed climate simulations respectively. The markers in (a) and (b) denote θ_l and q_s at the sea surface for the control (circles) and the perturbed climate (triangles). The black lines in (c) denote the adiabatic q_l profiles.

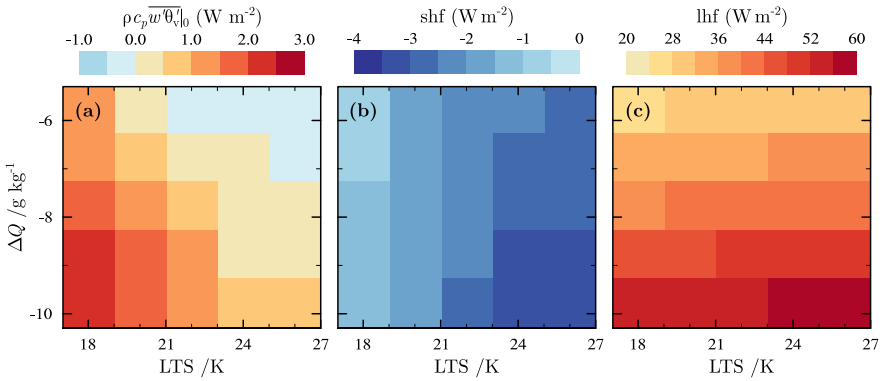

Figure 4.6. As Figure 4.1a, but for (a) the turbulent flux of the virtual potential temperature at the surface $\rho c_p \overline{w'\theta_v'}|_0$, (b) the surface sensible heat flux $\rho c_p \overline{w'\theta_l'}|_0$ and (c) the surface latent heat flux $\rho L_v \overline{w'q_t'}|_0$.

to range between 25 and 60 W m^{-2} as can be seen from Figure 4.6c, which is low as compared to typical maritime subtropical boundary layers (e.g. Bretherton and Pincus, 1995; Stevens et al., 2005b). For these reasons, the surface latent heat flux contributes only a few W m^{-2} to the surface buoyancy flux.

Low or negative values for the buoyancy flux in the subcloud layer will hardly produce or even dampen turbulence. The transport of moisture from the subcloud layer to the cloud layer is therefore inhibited, which in turn limits the surface latent heat flux as can be seen from its bulk formulation,

$$\overline{w'q_t'}|_0 = C_D |U| \left(q_{s,0} - q_{t,sl}\right). \tag{4.14}$$

Here, $|U|$ is the magnitude of the horizontal wind velocity, C_D is a drag coefficient and 'sl' in the subscript denotes the surface layer. The range and variation of the surface latent heat flux within the phase space are remarkably similar to those reported by DG14b for the SCM results.

4.4 Perturbed Climate

To investigate the response of the cloud layer to a warming of the climate, a uniform temperature increase of 2 K is applied to the initial profiles, while the initial relative humidity profile is kept the same as for the control case. Such a perturbation does not affect the LTS, but causes the magnitude of ΔQ to increase as is described in Section 4.2.2. We define the response of quantities to this perturbation by the difference between the perturbed and the control climate results divided by a temperature change of 2 K. This difference is denoted by a 'd'. It is important to keep in mind that, following DG14a and DG14b, the response is plotted against the ΔQ values of the control climate cases.

4.4.1 Response of the Surface Fluxes

A robust feature of climate warming scenarios is that the surface latent heat flux increases (Xu et al., 2010; Webb et al., 2013; Bretherton et al., 2013). Figure 4.7a shows that this is also the case for the LESs considered here. The increase is similar to that found from the MLM results by DG14a.

Rieck et al. (2012) argued that in response to a warming, the surface latent heat flux over the ocean increases such as to maintain a constant relative humidity $\mathcal{H}$. Using Eq. (4.14) the change of the surface humidity flux due to a temperature change $\mathrm{d}T$ can be expressed as

$$\mathrm{d}(\overline{w'q'_\mathrm{t}}|_0) = C_\mathrm{D}|U|(1-\mathcal{H}_\mathrm{sl})\left[q_\mathrm{s}(T_0+\mathrm{d}T,p_0)-q_\mathrm{s}(T_0,p_0)\right], \tag{4.15}$$

assuming that the wind speed does not change. Using the Clausius-Clapeyron relation to evaluate the change of the saturation specific humidity with temperature in Eq. (4.15), it can be readily shown that for typical subtropical conditions the surface humidity flux increases by about $7\,\%\,\mathrm{K}^{-1}$ given a constant $\mathcal{H}_\mathrm{sl}$ (Held and Soden, 2000). For the LES results, the relative increase of the surface evaporation varies from about $6\,\%\,\mathrm{K}^{-1}$ at high to $8\,\%\,\mathrm{K}^{-1}$ at low LTS, which indicates that $\mathcal{H}_\mathrm{sl}$ changes little with respect to the control case.

The response of the surface sensible heat flux to the climate perturbation is shown in Figure 4.7b. On average, this flux decreases by approximately $0.1\,\mathrm{W\,m^{-2}\,K^{-1}}$.

Figure 4.7c shows that the divergence of longwave radiation and hence the cooling of the boundary layer by the net emission of longwave radiation decreases. The warming due to absorption of shortwave radiation also decreases (Figure 4.7d), but less strongly. Hence, the net cooling of the boundary layer due to radiation decreases. The net decrease is on average $-0.4\,\mathrm{W\,m^{-2}\,K^{-1}}$. Assuming that the entrainment flux of θ_l does not change significantly, the weakened radiative cooling is likely the cause for the small decrease of the surface sensible heat flux.

4.4.2 Response of the Stratocumulus Layer

Figure 4.8a shows the change of the shortwave cloud radiative effect ($\mathrm{dCRE_{sw}}$) at the top of the atmosphere. It is defined as the difference between the net shortwave radiative flux at the top of the atmosphere for the actual atmospheric profile and for the clear sky, where the radiative flux is defined positive downward (Cess et al., 1989). The change of $\mathrm{CRE_{sw}}$ is used here as an indicator for the sign and magnitude of the cloud feedback. For low clouds $\mathrm{CRE_{sw}}$ is negative, which implies a net cooling of the atmosphere by clouds as a result of their strong ability to reflect shortwave radiation back to space. It can be seen from Figure 4.8a that the overall increase of $\mathrm{CRE_{sw}}$ varies between 4 and $12\,\mathrm{W\,m^{-2}\,K^{-1}}$, i.e. the cooling effect due to the stratocumulus clouds decreases and hence the cloud-climate feedback is positive for this idealized climate change scenario. Quantitatively similar changes were found from the SCM results (DG14b) as well as from the CGILS stratocumulus cases for the warming perturbation at constant relative humidity (Bretherton et al., 2013). The change of the longwave cloud radiative effect $\mathrm{CRE_{lw}}$ is negligibly small at less than $0.1\,\mathrm{W\,m^{-2}\,K^{-1}}$ and is therefore not shown.

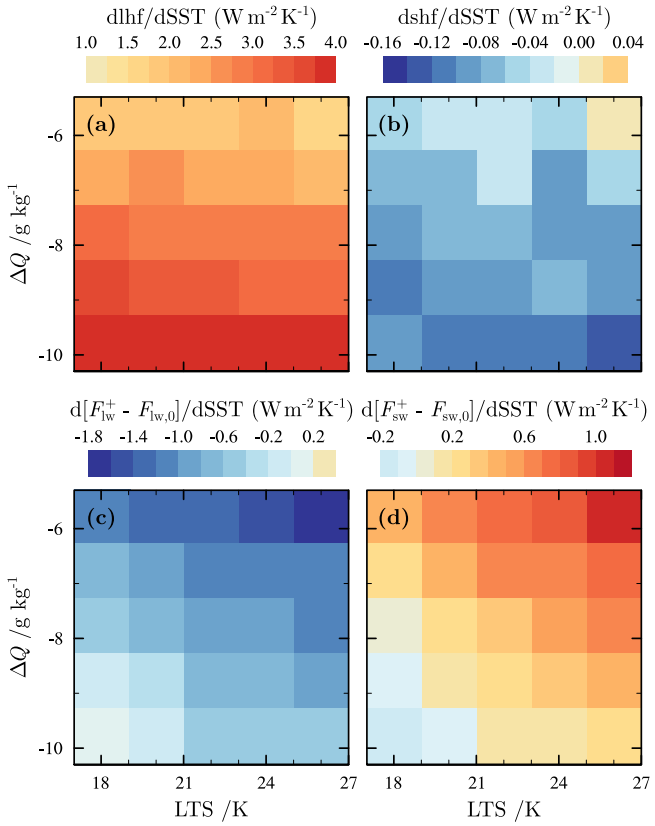

Figure 4.7. The response to the idealized climate perturbation that is described in Section 4.2.2 for (a) the surface latent heat flux $\rho L_v \overline{w'q'_t}|_0$, (b) the surface sensible heat flux $\rho c_p \overline{w'\theta'_l}|_0$ and for the radiative flux divergence over the boundary layer of (c) longwave and (d) shortwave radiation. The results are shown as a function of the ΔQ values of the control cases.

DG14a determined from ERA-Interim data the frequency of night-time occurrence of the LTS-ΔQ combinations in the months June, July and August in the area just off the Californian coast. Their results suggested that the frequency of occurrence increases diagonally toward the low LTS and dry free troposphere regime. From the LES results, the change of the cloud radiative effect is smallest in this regime. Hence, on average $\mathrm{dCRE_{sw}} \lesssim 8\,\mathrm{W\,m^{-2}\,K^{-1}}$ when weighted by frequency of occurrence. Furthermore, $\mathrm{dCRE_{sw}} > 4\,\mathrm{W\,m^{-2}\,K^{-1}}$ for LTS $> 18\,\mathrm{K}$ and for the wide range of ΔQ considered.

Medeiros et al. (2014) diagnosed the change of the CRE in response to a 4 K increase of the sea surface temperature from results of several climate models. For the high sensitivity models they showed that dCRE ranges between 2.5 and $5.5\,\mathrm{W\,m^{-2}\,K^{-1}}$ in the stratocumulus regime, which was identified by the presence of subsidence and by LTS $> 18\,\mathrm{K}$. The LES results therefore suggest that the thinning of stratocumulus clouds in response to a warming of the climate is of

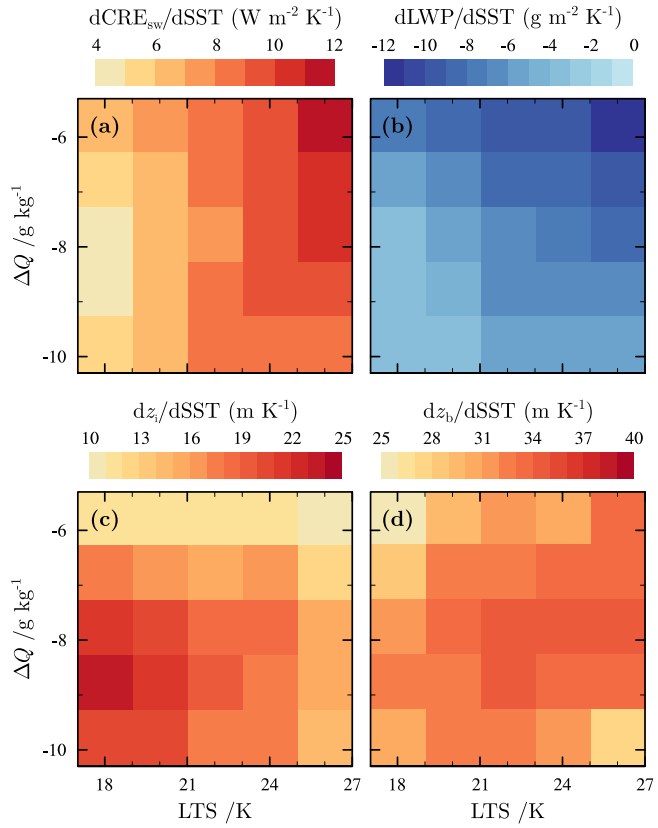

Figure 4.8. The response to the idealized climate perturbation described in Section 4.2.2 of (a) the shortwave cloud radiative effect at the top of the atmosphere $\mathrm{CRE_{sw}}$, (b) the liquid water path LWP, (c) the inversion height z_i and (d) the stratocumulus cloud base height z_b.

comparable magnitude as the response diagnosed from the current generation of climate models.

Since the boundary layer remains completely overcast for all perturbed climate simulations, the response of $\mathrm{CRE_{sw}}$ can be mainly attributed to a decrease of the LWP. Figure 4.8b shows that the LWP exhibits a maximum decrease of about $-12\,\mathrm{g\,m^{-2}\,K^{-1}}$ in the high LTS and moist free troposphere regime. The LWP decrease is, at about $-3\,\mathrm{g\,m^{-2}\,K^{-1}}$, considerably weaker for the driest and warmest free tropospheric conditions considered in this study.

Adiabatic Lapse Rate

It can be shown from thermodynamic arguments that $\partial q_\mathrm{l}/\partial z$ should increase with temperature (Paltridge, 1980). For the LES results, the effect of this increase on the LWP response can be quantified by first approximating the LWP of a

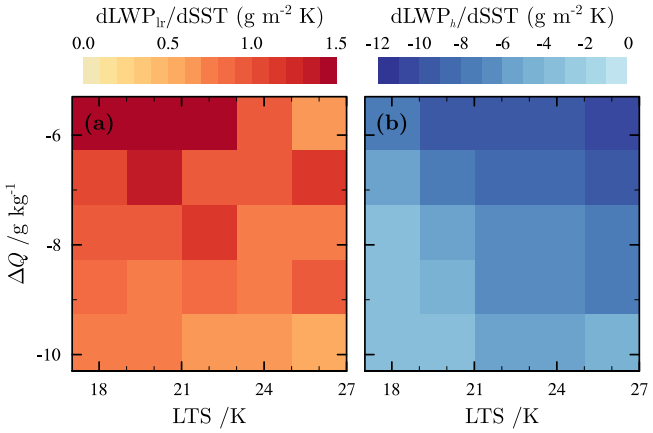

Figure 4.9. The normalized LWP response (a) due to the change of the lapse rate of liquid water specific humidity q_l and (b) due to the change of the geometrical cloud thickness h according to Eq. (4.18).

stratocumulus cloud layer as

$$\mathrm{LWP} = -\frac{1}{2}\rho_a \Gamma_{q_l} h^2, \tag{4.16}$$

in which

$$\Gamma_{q_l} = -\frac{\partial q_l}{\partial z} \tag{4.17}$$

is the lapse rate of the liquid water specific humidity and $h = z_i - z_b$ is the geometrical cloud thickness of the stratocumulus layer. In response to a climate perturbation, the LWP may change due to a change in Γ_{q_l} or in h as follows:

$$\mathrm{dLWP} = \underbrace{-\frac{1}{2}\rho_a h^2 \mathrm{d}\Gamma_{q_l}}_{\mathrm{dLWP_{lr}}} \underbrace{-\frac{1}{2}\rho_a \Gamma_{q_l} \mathrm{d}\left(h^2\right)}_{\mathrm{dLWP}_h}, \tag{4.18}$$

where it is assumed that the cloud cover does not change.

As temperature increases, $\mathrm{d}\Gamma_{q_l} < 0$, so the first term of Eq. (4.18) will cause an increase of the LWP in a warmer climate. The magnitude of the LWP response as a result of this lapse rate effect depends on temperature and on the depth of the cloud layer and is between 1 and 1.5 g m^{-2} K^{-1} for the current setup as can be seen from Figure 4.9a. From LESs of cumulus-topped boundary layers, Rieck et al. (2012) also found this increase of the in-cloud liquid water content. Nevertheless, the domain-averaged LWP decreased in their case mainly due to a decrease of the cloud cover, which was attributed to a decrease of $\mathcal{H}$. Therefore, the sign of the cloud feedback was positive.

For the stratocumulus cases considered here the LWP decreases as well, which is due to a decrease of the geometrical thickness h of the stratocumulus layer. This effect is described by the second term on the right hand side of Eq. (4.18). Figure

4.9b shows that the decrease of the LWP due to the decrease of h is much stronger than the LWP increase due to the change in Γ_{q_l}. The decrease of h is the result of an increase of stratocumulus cloud base height z_b relative to the inversion height z_i. Below, the responses of z_i and z_b are discussed individually.

Inversion Height

An increase of the inversion height in the perturbed climate can be expected as a result of the increased surface latent heat flux that invigorates the turbulence in the boundary layer (Bretherton and Wyant, 1997; Bretherton and Blossey, 2014). This effect has been found in several cumulus studies (Xu et al., 2010; Nuijens and Stevens, 2011; Rieck et al., 2012). However, as a result of the assumption that the initial relative humidity in the free troposphere is not affected by the climate perturbation, the total specific humidity in the free troposphere is increased. Since this causes the downwelling longwave radiative flux at the top of the stratocumulus layer to increase and consequently the radiatively induced cloud-top cooling to decrease, the latter effect will act to reduce the entrainment rate.

In their MLM study, DG14a separated these mechanisms by first applying a warming perturbation of 2 K to the sea surface and the atmosphere at constant initial relative humidity, without changing the prescribed net radiative cooling rate of the boundary layer. Under that assumption, the inversion height increased significantly for all free tropospheric conditions. The radiative flux divergence over the boundary layer was decreased by $1.5\,\mathrm{W\,m^{-2}\,K^{-1}}$ in a second set of simulations, in addition to the climate warming perturbation. In this experiment, z_i decreased for all cases. In the LES results, the response of the net radiative flux divergence over the boundary layer is weaker than that imposed in the MLM experiments of DG14a, at approximately $0.5\,\mathrm{W\,m^{-2}\,K^{-1}}$ as was deduced from Figures 4.7c and 4.7d. This modest radiative response causes the increase of the inversion height due to the increased latent heat fluxes to be the dominating mechanism and hence z_i increases by between 10 and $25\,\mathrm{m\,K^{-1}}$ as can be seen from Figure 4.8c. In contrast, a z_i decrease was found from the LES results of the CGILS S12 stratocumulus case for those simulations in which the subsidence velocity was not perturbed (Bretherton et al., 2013). Almost all LES models that participated in the CGILS intercomparison study agree on this response (Blossey et al., 2013). The response of the net radiative flux divergence was evaluated at -1.0 to -1.5 $\mathrm{W\,m^{-2}\,K^{-1}}$, which is at least two times as large as for the present simulations. Therefore, it is possible that for the CGILS S12 case, the z_i response due to the change of the net radiative flux divergence dominates the total response of the inversion height, causing it to decrease.

Admittedly, the z_i increases that were found are not large compared to the vertical grid spacing of 10 m. The response is significant however, as the differences are persistent during the entire ten-day simulation period.

Stratocumulus Cloud Base Height

Figure 4.8d shows that the increase of cloud base height z_b is approximately twice as large as that of z_i. Hence, the stratocumulus layer thins for all free tropospheric conditions. The increase of z_b is related to a decrease of the relative humidity

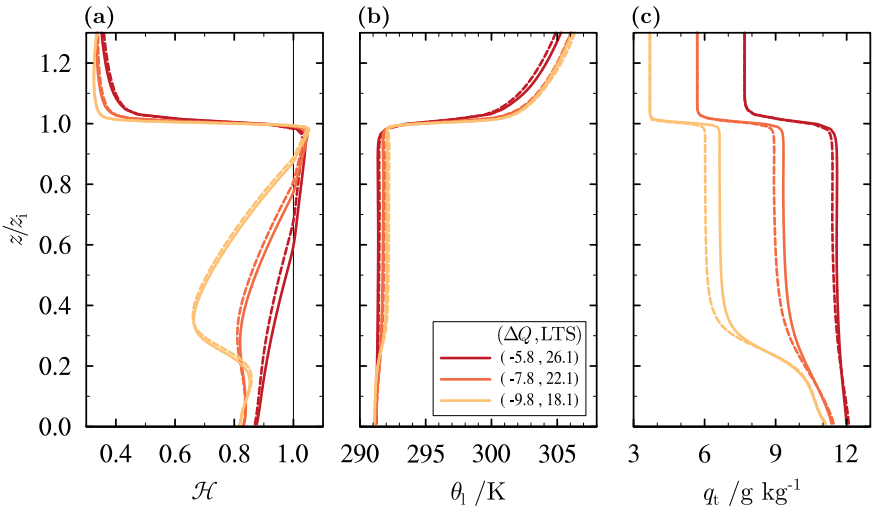

Figure 4.10. (a) The relative humidity $\mathcal{H}$, (b) the liquid water potential temperature θ_l and (c) the total specific humidity q_t as a function of dimensionless height z/z_i. Solid and dashed lines show the control and the perturbed climate results, respectively. The initial perturbations have been subtracted from the perturbed climate results in (b) and (c). The black line in (a) indicates the saturation level, $\mathcal{H} = 1$.

$\mathcal{H}$, vertical profiles of which are shown in Figure 4.10a. The vertical coordinate has been non-dimensionalized by dividing by z_i, to simplify the comparison of the boundary layer structure between the perturbed and the control climate results. Near the surface $\mathcal{H}$ changes little, as was already deduced from the analysis of the surface latent heat flux response. Throughout the upper part of the boundary layer, $\mathcal{H}$ decreases slightly, with the largest decrease located in the middle of the boundary layer. For the cumulus simulations of Rieck et al. (2012) $\mathcal{H}$ decreased as well, affecting the LWP mainly through a decrease of the cloud fraction. For the stratocumulus layers considered here the $\mathcal{H}$ response causes an LWP decrease through an increase of the stratocumulus cloud base height.

To assess the effect of the response of θ_l and q_t on the decrease of the relative humidity in the cloud layer, Figures 4.10b and 4.10c show their vertical profiles as a function of the normalized height z/z_i. To simplify the comparison with the control case (indicated by solid lines), the initial perturbations of θ_l and q_t have been subtracted from the steady-state results of the perturbed climate simulations (dashed lines). Clearly, the shape of the θ_l profile is hardly affected by the climate perturbation. The profiles of q_t on the other hand are more decoupled in the perturbed simulations, suggesting that the decrease of the relative humidity is mainly due to a drying of the upper part of the boundary layer.

4.4.3 Inversion Properties

Figure 4.11 shows a scatter plot of the initial inversion jumps of Δq_t and $\Delta\theta_l$ in light numbers for the control (black) and the perturbed climate simulations (blue). The solid lines connect the initial and steady-state inversion jumps. The base and the top of the inversion layer are determined by finding the layer in which the variance of θ_l exceeds 5 % of its peak value (Yamaguchi et al., 2011), and the inversion jump is defined as the difference of a variable across this layer. To provide a reference within the Δq_t and $\Delta\theta_l$ phase space, the buoyancy reversal criterion line as derived by Randall (1980) and Deardorff (1980a) is also shown in Figure 4.11. It was suggested in these studies that solid stratocumulus cloud decks could not persist at the left side of this line as a result of a runaway entrainment mechanism, which would dry and warm the stratocumulus layer thereby causing it to rapidly break up. However, stable stratocumulus layers have often been observed for such conditions (e.g. Kuo and Schubert, 1988; Stevens et al., 2003b). It was furthermore argued by Van der Dussen et al. (2014) that stratocumulus clouds can persist far into the buoyancy reversal regime if the cloud building processes, such as the humidity flux from the surface, are sufficiently strong.

The initial value of Δq_t can be related to the bulk tropospheric jump ΔQ

$$\Delta q_t = q_{t,ft} - q_{t,bl} = \Delta Q - (q_{s,0} - q_{t,bl}), \tag{4.19}$$

in which $q_{t,bl}$ is the initial boundary-layer value of q_t. Because we assume that the initial relative humidity does not change in a perturbed climate, the increase of q_t in the boundary layer is larger than in the colder free troposphere, explaining the larger initial value of Δq_t for the perturbed climate simulations. However, the initial differences of Δq_t between the control and the perturbed climate cases have been reduced significantly at the end of the simulations. These reductions can only be caused by a stronger drying of the stratocumulus cloud layer in the perturbed relative to the control climate, since q_t is constant with height and time in the lower part of the free troposphere. Much of the drying is due to entrainment, which can be expressed as the product of the entrainment rate and the inversion jump of humidity (Lilly, 1968)

$$\overline{w'q_t'}|_{ent} = -w_e \Delta q_t. \tag{4.20}$$

Hence a larger inversion jump of q_t increases the potential to dry the boundary layer by entrainment.

The steady-state inversion jumps collapse remarkably well onto a line in the phase space in Figure 4.11. The imaginary line onto which the perturbed climate results approximately collapse is shifted to the lower left hand corner in Figure 4.11 with respect to the control climate. For the perturbed climate simulations $\Delta\theta_l$ is up to 1 K smaller. This decrease of $\Delta\theta_l$ is mainly due to enhanced radiative cooling of the lower free troposphere as a result of the increase in the specific humidity. Van der Dussen et al. (2014) showed that a colder and a drier free troposphere (i.e. a smaller value of $\Delta\theta_l$ and a larger value of Δq_t, respectively) are typically associated with a stronger cloud thinning tendency due to entrainment. For the current set of simulations, the stronger entrainment drying tendency is to a large

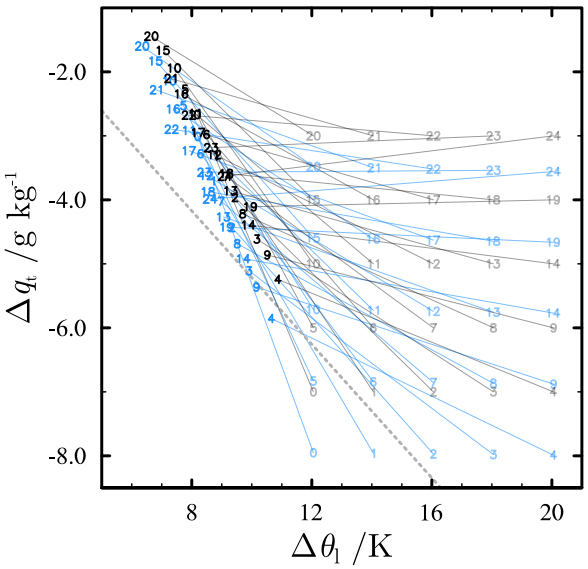

Figure 4.11. Scatter plot of $\Delta\theta_l$ and Δq_t for each of the control (black) and the perturbed climate simulations (blue). The experiments are numbered consecutively starting from the simulation with the lowest LTS and the most negative value of ΔQ. The initial conditions are indicated by the numbers in regular font, while the bold-faced numbers indicate the inversion jumps averaged over the tenth day of the simulations. The initial and final states of the simulations are connected by solid lines and the grey dotted line denotes the $\kappa = 0.23$ buoyancy reversal criterion (Kuo and Schubert, 1988) as a reference.

extent balanced by an increase of the surface latent heat flux such that the LWP can reach a new equilibrium state.

4.5 Discussion

4.5.1 Correlation Between Change of ΔQ and LWP Response

The response of the stratocumulus layer to the idealized climate perturbation can be summarized as follows. In the first place, the stratocumulus base height increases due to a drying of the upper part of the boundary layer, that is mostly related to the increase of the magnitude of ΔQ. Second, the inversion height increases, which is related to the competition between the increase of the surface latent heat flux and the increase of the downwelling longwave radiation. This competition is qualitatively accounted for in the change of the value of ΔQ as it is defined as the difference between $q_{t,ft}$ and $q_{s,0}$.

The important mechanisms determining the response of the stratocumulus layer can therefore mostly be correlated with changes in ΔQ. Figure 4.4a shows the LWP as a function of the actual value of ΔQ for the control (blue shades) as well as for the perturbed climate simulations (red shades). The increase of the magnitude of

ΔQ as a result of the climate perturbation shifts the location of each simulation in the plot to the left with respect to the control simulations. The perturbed climate cases, with the exception of the high LTS ones, fall approximately on the line that can be fitted through the control climate results. This suggests that much of the LWP decrease can indeed be attributed to the change of ΔQ.

4.5.2 Radiation Versus Surface-driven Boundary Layers

It was shown that for most cases considered in this research, the surface buoyancy flux is rather small (Figure 4.6c). Furthermore, the vertical profiles of the total specific humidity show that the boundary layer structure is decoupled for the cases with the deepest boundary layers. Figure 4.12a and 4.12b show profiles of the buoyancy flux and of the vertical velocity variance $\overline{w'^2}$ respectively. The buoyancy flux is small or negative in the subcloud layer, but large in the stratocumulus layer as a result of net radiative cooling. This causes $\overline{w'^2}$, which constitutes an important part of the turbulence kinetic energy, to be much larger in the stratocumulus layer than at the surface. Figure 4.12c furthermore shows that the vertical velocity skewness

$$S_w = \frac{\overline{w'^3}}{\left(\overline{w'^2}\right)^{3/2}}, \tag{4.21}$$

is mostly negative throughout the boundary layer, apart from the spike close to the top of the boundary layer that is often found for stratocumulus clouds (Moeng and Rotunno, 1990). A negative value for S_w indicates that the turbulence in the boundary layer is determined mostly by downdrafts and that the boundary layer dynamics are predominantly radiatively driven.

The results of an SCM intercomparison study will be discussed in a companion paper (Dal Gesso et al., 2015), which includes a detailed comparison with the LES results discussed here. In many SCMs, the vertical transport is parameterized in terms of updrafts forced from the surface. As the current setup results in predominantly top-driven boundary layers it can be expected to be particularly challenging for such SCMs. This is illustrated by the results of the EC-Earth SCM used by DG14b, which, among others, show much less dependence of the steady-state inversion height on the free tropospheric conditions as compared to the LES results.

The MLM results of DG14a indicated that for well-mixed boundary layers, the sign of the stratocumulus cloud feedback is positive. The present study shows that in the other extreme, namely a decoupled situation with weak surface forcing, the sign is positive as well. Similarly, Bretherton et al. (2013) found that the sign of the feedback for both well-mixed and decoupled stratocumulus cases is positive. The sign of the cloud-climate feedback therefore does not seem to depend on the degree of decoupling of the boundary layer. It is reassuring that despite the different setup of CGILS as compared to the present experiments, the sign of the cloud feedback is found to be consistent and that the thinning of stratocumulus clouds is a robust response to a climate warming perturbation at constant initial relative humidity. The magnitude of the response may however be affected by the details of the setup.

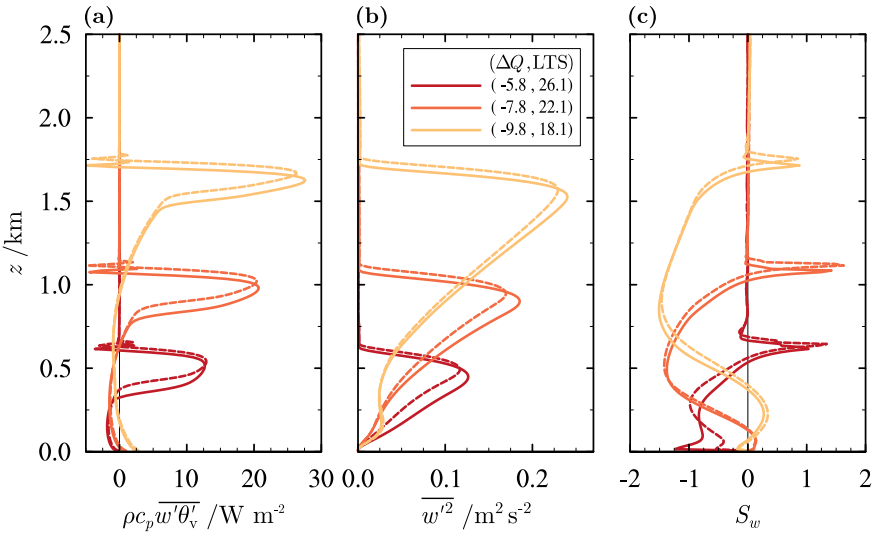

Figure 4.12. As Figure 4.5, but for (a) the turbulent flux of the virtual potential temperature $\rho c_p \overline{w'\theta_v'}$ in $\mathrm{W\,m^{-2}}$ as a proxy for the buoyancy flux, (b) the vertical velocity variance $\overline{w'^2}$ and (c) the skewness of the vertical velocity S_w as defined by Eq. (4.21).

The LES results show an increase of the inversion height in the perturbed climate. In contrast, a decrease is found the CGILS stratocumulus experiments (-30 to $0\,\mathrm{m\,K^{-1}}$) (Blossey et al., 2013) as well as from the MLM experiments by DG14a (-40 to $-10\,\mathrm{m\,K^{-1}}$). A possible cause for this discrepancy is the relatively weak response of the net radiative divergence over the boundary layer for the present simulations as was discussed in Section 4.4.2. Furthermore, the decoupling of the boundary layer may play a role. To investigate the sensitivity of the cloud response to boundary layer decoupling and its effect on the response of the inversion height, the current setup could be adjusted to allow for positive surface sensible and larger surface latent heat fluxes by prescribing cooling and drying tendencies due to horizontal advection in the boundary layer. This was for instance done for the CGILS experiments (Blossey et al., 2013) as well as for the steady state simulations of Chung et al. (2012), both of which have significantly higher surface fluxes and better mixed boundary layers for their stratocumulus simulations. This approach could make the case setup more realistic. The downside of a less idealized setup is that it introduces additional degrees of freedom and potentially complicates the interpretation of the response of the cloud layer.

4.6 Conclusions

The influence of the free tropospheric conditions on the steady states of radiatively-driven stratocumulus-topped boundary layers was investigated by running a set of 25 large-eddy simulations in a phase space spanned by a range of free tropospheric

temperatures and humidities. The response to an idealized climate perturbation was furthermore assessed by uniformly increasing the initial temperature profile of the control simulations by 2 K, while the total specific humidity was increased to keep the initial relative humidity the same as for the control simulations. The results complement an earlier conceptual study with a mixed-layer model (Dal Gesso et al., 2014b) as well as simulations with a single-column model version of the EC-Earth climate model (Dal Gesso et al., 2014a).

4.6.1 Control Climate

The control climate simulations show that the steady-state inversion height increases as the LTS decreases, i.e. as the free troposphere becomes warmer. Furthermore, for a dry free troposphere the downwelling longwave radiative flux absorbed by the stratocumulus layer is relatively low, such that the cloud-top cooling gets enhanced thereby increasing the entrainment rate and the boundary layer depth. The LWP depends mainly on ΔQ and decreases as the free troposphere becomes drier.

For the MLM results by DG14a the opposite was found, which is due to the inability of the MLM to represent a decoupled, two-layer boundary layer structure. The LES results indicate only a weak forcing of turbulence from the surface, causing the dynamics of the boundary layer to be mainly driven by radiative cooling at the cloud top. This results in a building up of moisture in the subcloud layer and a relatively strong drying of the cloud layer by entrainment.

4.6.2 Perturbed Climate

In the perturbed climate simulations, the surface latent heat flux is approximately $7\,\%\,\mathrm{K}^{-1}$ larger than in the control cases, as is expected on the basis of Clausius-Clapeyron scaling. This stronger surface evaporation flux invigorates turbulence in the boundary layer and hence tends to increase the entrainment rate (Rieck et al., 2012). On the other hand, the increased specific humidity in the free troposphere enhances the downwelling longwave radiative flux, which tends to decrease the entrainment rate. The net effect is a small increase of the inversion height of between 10 and $25\,\mathrm{m\,K}^{-1}$.

The drying tendency due to entrainment is shown to increase as a result of the climate perturbation, causing an increase of stratocumulus base height that is greater than the increase of stratocumulus top height. Hence the stratocumulus layer thins, which results in a decrease of the LWP that is largest at $-12\,\mathrm{g\,m}^{-2}\,\mathrm{K}^{-1}$ for high LTS and relatively humid free tropospheric conditions. As a result of the thinning of the cloud layer, the shortwave cloud radiative effect weakens for all free tropospheric conditions by on average $8\,\mathrm{W\,m}^{-2}\,\mathrm{K}^{-1}$ indicating that the sign of the cloud feedback is positive, which is consistent with recent similar studies (Blossey et al., 2013; Bretherton et al., 2013). In comparison, the SCM results of DG14b overall indicated a positive feedback as well, but the sign and the magnitude of the feedback varied irregularly throughout the phase space.

An important finding is that the change of the bulk humidity difference between the free troposphere and the surface in a perturbed climate is key to the change in the stratocumulus cloud amount, in particular since it determines the drying of

Table 4.1. Numerical and domain details for the reference as well as the sensitivity simulations. The aspect ratio of the grid boxes and the domain size are equal for all simulations.

	low res	reference	high res
$\mathrm{d}x, \mathrm{d}y$	75 m	50 m	25 m
$\mathrm{d}z$	15 m	10 m	5 m
grid aspect ratio	5	5	5
N_x, N_y	80	120	240
N_z	136	219	356

the cloud layer through entrainment. This process is responsible for the change of stratocumulus base height. The change of ΔQ furthermore controls the response of the downwelling longwave radiation that is absorbed by the cloud as well as the response of the surface latent heat flux. These processes together determine the change of the inversion height.

Appendix 4.A Sensitivity to Vertical Resolution

In many of the recent intercomparison studies focused on stratocumulus (transitions), grids were employed with fine, often 5 m, vertical resolutions at the inversion in order to make sure that the inversion gradients are well resolved. To reduce computational costs, a vertical resolution of 10 m is chosen for the simulations presented in the current research. Two additional sensitivity runs were conducted to test the dependence of the results on resolution. The case in the middle of the phase space, with (ΔQ, LTS) = ($-5.8\,\mathrm{g\,kg^{-1}}$, 22.1 K) is used for this sensitivity experiment. The simulation details can be found in Table 4.1. For all simulations, the aspect ratio of the grid boxes $\mathrm{d}x : \mathrm{d}z = 5 : 1$ in the part of the domain with uniform vertical grid spacing.

Figure 4.13a shows vertical profiles of θ_l for the three experiments described in Table 4.1, averaged over hours 18 to 24 of the simulations. The effect of a change of the resolution on θ_l is clearly small. At lower resolutions the inversion does tend to be more spread out, but the effect on the entrainment rate is limited as the inversion height varies by only 10 m among the simulations. Figure 4.13b shows that the upper part of the boundary layer is moister at high resolution, leading to a thicker cloud layer as can be seen in Figure 4.13c. The LWP increases considerably from $54\,\mathrm{g\,m^{-2}}$ at 15 m, to $64\,\mathrm{g\,m^{-2}}$ at 10 m, to $80\,\mathrm{g\,m^{-2}}$ at 5 m vertical resolution. The sensible heat flux $\rho L_\mathrm{v} \overline{w'\theta_\mathrm{l}'}$ profiles in Figure 4.13d are very similar for all simulations, but the latent heat flux increases as the resolution is increased (Figure 4.13e). Figure 4.13f shows the resolved vertical velocity variance $\overline{w'^2}$ profiles. The three simulations are all strongly top-driven, judging from the large peak at the top of the boundary layer. The magnitude of this peak is well captured by the reference simulation, although the high-resolution simulation has a higher $\overline{w'^2}$ in the subcloud layer.

Figure 4.14 shows the filtered and the subfilter scale contributions to the virtual potential temperature flux in $\mathrm{W\,m^{-2}}$ as a function of height. The relative

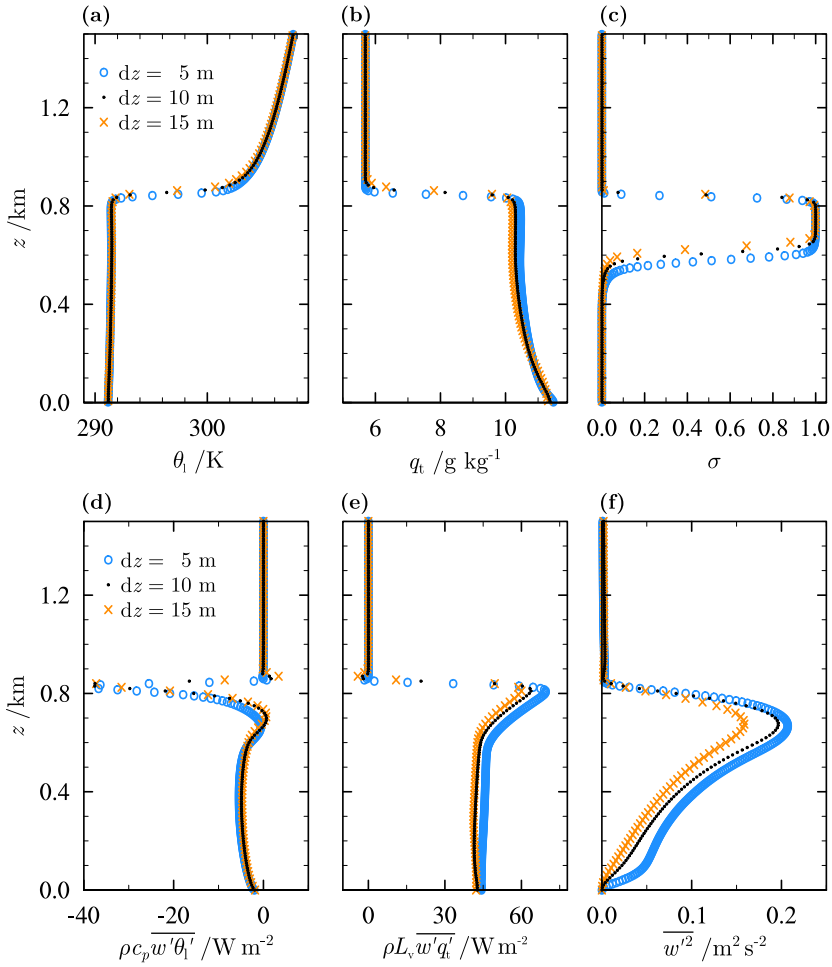

Figure 4.13. Vertical profiles of (a) the liquid water specific humidity θ_l, (b) the total humidity q_t, (c) the cloud fraction σ, the total (resolved + sub-filter scale) turbulent fluxes (d) $\rho c_p \overline{w'\theta_l'}$ and (e) $\rho L_v \overline{w'q_t'}$ and (f) the resolved vertical velocity variance $\overline{w'^2}$ averaged over hours 18 to 24, for the case in the center of the phase space where $\Delta Q = -5.8\,\mathrm{g\,kg^{-1}}$ and the LTS = 22.1 K. Additional information about the simulations can be found in Table 4.1.

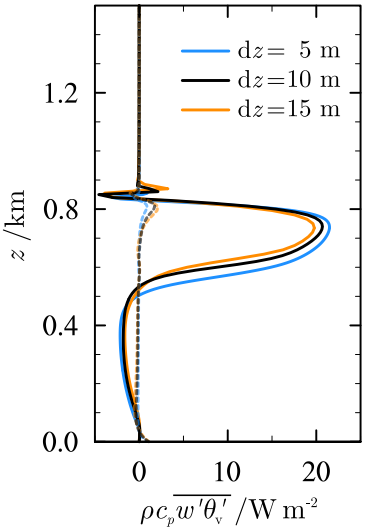

Figure 4.14. As Figure 4.13, but for the resolved (solid lines) and the subfilter-scale contributions (dashed lines) to $\rho c_p \overline{w'\theta_v'}$, the turbulent flux of the virtual potential temperature in $\mathrm{W\,m^{-2}}$.

contribution of sub-filter scales to the total turbulent flux is clearly low for each of the cases and hence most of the turbulence in the simulations is explicitly resolved.

The results shown in Figures 4.13 and 4.14 provide confidence that the steady-state behavior of the simulations with the 10 m is qualitatively comparable to the higher resolution simulations. The main quantitative differences are likely found in the results for the LWP, which was found to increase by as much as 25 % when the vertical resolution was increased from 10 to 5 m.

Acknowledgements

The investigations were done as part of the European Union CLoud Intercomparison, Process Study & Evaluation (EUCLIPSE) project, funded under Framework Program 7 of the European Union. The work was sponsored by the National Computing Facilities Foundation (NCF) for the use of supercomputer facilities. The model output used to generate the figures is included as supplementary material, but can also be obtained from the corresponding author upon request (email: johanvanderdussen@outlook.com). We thank the two anonymous reviewers whose comments helped to improve the manuscript.

5

How Large-scale Subsidence Affects Stratocumulus Transitions

Some climate modeling results suggest that the Hadley circulation might weaken in a future climate, causing a subsequent reduction in the large-scale subsidence velocity in the subtropics. In this study we analyze the cloud liquid water path (LWP) budget from large-eddy simulation (LES) results of three idealized stratocumulus transition cases each with a different subsidence rate. As shown in previous studies a reduced subsidence is found to lead to a deeper stratocumulus-topped boundary layer, an enhanced cloud-top entrainment rate and a delay in the transition of stratocumulus clouds into shallow cumulus clouds during its equatorwards advection by the prevailing trade winds. The effect of a reduction of the subsidence rate can be summarized as follows. The initial deepening of the stratocumulus layer is partly counteracted by an enhanced absorption of solar radiation. After some hours the deepening of the boundary layer is accelerated by an enhancement of the entrainment rate. Because this is accompanied by a change in the cloud-base turbulent fluxes of moisture and heat, the net change in the LWP due to changes in the turbulent flux profiles is negligibly small.

Submitted to *Atmos. Chem. Phys.* (2015), with S.R. de Roode and A.P. Siebesma.

5.1 Introduction

As subtropical marine stratocumulus clouds are advected by the tradewinds over increasingly warm water they are often observed to transition into shallow cumulus clouds. Such transitions involve a rapid decrease of the cloud cover and the cooling effect due to the presence of low clouds is hence diminished. Therefore, a change of the pace of stratocumulus transitions in a future climate could potentially be of importance for the magnitude of the cloud-climate feedback.

Some general circulation model results suggest that the Hadley-Walker cell may weaken as a result of climate warming (e.g. Held and Soden, 2006; Vecchi and Soden, 2007). In the subtropical part of the Hadley cell there is a mean subsiding motion of air. It is therefore reasonable to assume that the large-scale subsidence in subtropical areas will weaken in a future climate. A weakening of the large-scale subsidence caused an increase of the liquid water path (LWP) of stratocumulus layers within a steady-state Eulerian framework (Blossey et al., 2013; Bretherton et al., 2013). As such, reduced subsidence might be one of the few processes to cause additional cloudiness in a future climate scenario (Bretherton and Blossey, 2014). It is therefore of paramount importance to have a thorough understanding of how a weakening of the large-scale subsidence increases the LWP and the life-time of stratocumulus clouds.

Together with the entrainment rate, the subsidence velocity determines the rate of deepening of boundary layers that are capped by an inversion, as follows

$$\frac{\mathrm{d}z_\mathrm{i}}{\mathrm{d}t} = w_\mathrm{e} + \overline{w}(z_\mathrm{i}). \tag{5.1}$$

Here, z_i is the height of the inversion, t is time, w_e is the entrainment velocity and $\overline{w}$ is the large-scale subsidence velocity. A lower subsidence velocity therefore leads to a more rapid deepening of the boundary layer if the entrainment velocity remains unaffected. Such deeper boundary layers are often assumed to be less well mixed than shallow boundary layers (Park et al., 2004; Wood and Bretherton, 2004). It was therefore hypothesized that weaker subsidence could increase the pace of stratocumulus transitions (e.g. Wyant et al., 1997; Bretherton et al., 1999a).

Svensson et al. (2000), however, used a one-dimensional turbulence model to show that the moment of breakup of the stratocumulus layer is actually delayed when the magnitude of the large-scale subsidence velocity is decreased. Later, Sandu and Stevens (2011) corroborated these findings by performing several large-eddy simulations (LESs) of stratocumulus transition cases. Moreover, Myers and Norris (2013) found from observations that low cloud amount in the subtropics tends to decrease as subsidence becomes stronger.

This study investigates the effect of a change in the strength of the Hadley circulation, as quantified by the large-scale subsidence velocity, on the typical time scale of the breakup of stratocumulus and its subsequent transition to broken shallow cumulus. The entrainment rate as well as the subsidence velocity are typically poorly constrained by observations (Bretherton et al., 1995; De Roode and Duynkerke, 1997; Ciesielski et al., 2001; Carman et al., 2012) or by reanalysis products (Duynkerke et al., 1999). For this reason, LES is used here. A budget equation for the tendency of the LWP of the stratocumulus layer as derived by

Van der Dussen et al. (2014) is used to analyze the LES results in order to determine the role of each individual physical processes during stratocumulus transitions. Through this analysis, insight is gained into how subsidence affects the pace of stratocumulus transitions, which helps to determine the robustness of the sign of the response to a weakening subsidence.

In the next section, first the methodology is explained, which is used to assess the relative importance of each physical process that is involved in the evolution of stratocumulus-topped boundary layers. In Section 5.3 the details of the LESs that have been performed are described. The LWP tendency during the ASTEX transition is analyzed in Section 5.4, while several sensitivity studies are discussed in Section 5.5. In the final section, a short summary of the conclusions are presented.

5.2 Methodology

5.2.1 Contributions to the LWP Tendency

The cloud albedo increases for larger values of the LWP, which is defined as

$$\mathrm{LWP} = \int_{z=0}^{\infty} \rho q_\mathrm{l} \mathrm{d}z, \tag{5.2}$$

where q_l is the liquid water specific humidity, which is the sum of the cloud water q_c and rain water specific humidity q_r. Furthermore, ρ is the density of air and z is height. Van der Dussen et al. (2014) extended the LWP budget analysis of Randall et al. (1984) by including the contribution of cloud-base turbulent fluxes, radiation and drizzle, in addition to entrainment. The resulting LWP budget equation allows for the evaluation of the relative contribution of individual physical processes to the LWP tendency, so

$$\frac{\partial \mathrm{LWP}}{\partial t} = \mathrm{Ent} + \mathrm{Base} + \mathrm{Rad} + \mathrm{Prec} + \mathrm{Subs}. \tag{5.3}$$

Here, the abbreviations indicate LWP tendencies as a result of entrainment of free tropospheric air into the boundary layer at the top of the stratocumulus layer (Ent), turbulent fluxes of total specific humidity q_t and liquid water potential temperature θ_l at the base of the stratocumulus layer (Base), divergence of the net radiative flux over the stratocumulus layer (Rad), divergence of the precipitation flux over the stratocumulus layer (Prec) and large-scale subsidence (Subs). We refer to Van der Dussen et al. (2014) for a derivation of these terms. Below, the results are repeated for convenience.

The LWP tendency due to large-scale subsidence can be written as:

$$\mathrm{Subs} = -\rho h \Gamma_{q_\mathrm{l}} \overline{w}(z_\mathrm{i}), \tag{5.4}$$

in which h is the thickness of the stratocumulus cloud layer, $\overline{w}$ is the large-scale vertical velocity and $\Gamma_{q_\mathrm{l}} = -\partial q_\mathrm{l}/\partial z < 0$ is the lapse rate of q_l. The value of Γ_{q_l} is approximated by assuming a moist adiabatic temperature lapse rate. Subsidence acts to decrease the LWP by pushing the stratocumulus cloud top down.

Note that all variables used in the current study are slab-averages unless specifically stated otherwise. The overbar that is commonly used to indicate a slab-averaged variable is omitted for notational convenience, except for the turbulent fluxes and variances.

The entrainment contribution to the LWP tendency is as follows:

$$\mathrm{Ent} = \rho w_\mathrm{e} \left(\eta \Delta q_\mathrm{t} - \Pi \gamma \eta \Delta \theta_\mathrm{l} - h \Gamma_{q_\mathrm{l}}\right), \tag{5.5}$$

where Δq_t and $\Delta \theta_\mathrm{l}$ indicate the inversion jumps of q_t and θ_l respectively, Π is the Exner function and $\gamma = \partial q_\mathrm{s}/\partial T \approx 0.55\,\mathrm{g\,kg^{-1}\,K^{-1}}$ is described by the Clausius-Clapeyron relation. Furthermore, η is a thermodynamic factor that depends mainly on temperature and is given by

$$\eta = \left(1 + \frac{L_\mathrm{v}\gamma}{c_p}\right)^{-1} \approx 0.4,$$

with c_p the specific heat of air at constant pressure and L_v the latent heat of vaporization.

The remaining three terms of Eq. (5.3) are

$$\mathrm{Base} = \quad \rho\eta \left[\overline{w'q_\mathrm{t}'}(z_\mathrm{b}) - \Pi\gamma\overline{w'\theta_\mathrm{l}'}(z_\mathrm{b})\right], \tag{5.6}$$

$$\mathrm{Rad} = \quad \frac{\eta\gamma}{c_p}\left[F_\mathrm{rad}(z_\mathrm{t}) - F_\mathrm{rad}(z_\mathrm{b})\right], \tag{5.7}$$

$$\mathrm{Prec} = -\rho\left[P(z_\mathrm{t}) - P(z_\mathrm{b})\right]. \tag{5.8}$$

Here, $\overline{w'q_\mathrm{t}'}$ and $\overline{w'\theta_\mathrm{l}'}$ are the turbulent fluxes of q_t and θ_l. Furthermore, z_b and z_t are stratocumulus base and top height, respectively. Furthermore, F_rad is the radiation flux in $\mathrm{W\,m^{-2}}$ and P is the precipitation flux in $\mathrm{m\,s^{-1}}$, both of which are defined negative downward.

5.2.2 Evaluation of Cloud Boundaries

The LWP budget equation described in the previous section is used to quantify the relative importance of the individual physical processes to the total LWP tendency. To this end, Eqs. (5.4)-(5.8) will be evaluated using slab-averaged vertical profiles derived from the LES. To accurately evaluate the LWP tendencies with this method, it is important to properly define the top and bottom interfaces of the stratocumulus layer.

The stratocumulus base height is defined as the minimum height where the slab-averaged cloud fraction σ exceeds 0.4,

$$z_\mathrm{b} = \min(z), \quad \text{where} \quad \sigma(z) > 0.4. \tag{5.9}$$

The criterion is chosen such that the cumulus clouds below the stratocumulus layer are ignored. The analysis is quite insensitive to the critical σ value as stratocumulus base height is typically well defined in terms of the cloud fraction profile. Any value between $\sigma \approx 0.2$ and 0.8 can be used.

Some more care is required for the definition of stratocumulus top height z_t. To take into account the vertical undulations in the cloud top and in particular its effect on the horizontal slab mean flux profiles (vanZanten et al., 1999), the budget analysis is performed up to the top of the inversion layer, the height of which is defined as z_i^+. Hence, in Eqs. (5.7)

$$z_t = z_i^+. \tag{5.10}$$

There is practically no cloud water at this level, so that the precipitation flux is negligible, $P(z_t) \approx 0$.

The lower and upper boundaries of the inversion layer are determined on the basis of the profile of the variance of θ_l as follows (Yamaguchi et al., 2011):

$$z_i^+ = z, \quad \text{where} \quad \overline{\theta_l'^2} = 0.05 \cdot \max(\overline{\theta_l'^2}) \quad \text{and} \quad z > z_{max}, \tag{5.11a}$$

$$z_i^- = z, \quad \text{where} \quad \overline{\theta_l'^2} = 0.05 \cdot \max(\overline{\theta_l'^2}) \quad \text{and} \quad z < z_{max}. \tag{5.11b}$$

Here, z_{max} is the height at which the maximum of the $\overline{\theta_l'^2}$ profile is located. Linear interpolation is used between the grid levels to determine z_i^+ and z_i^-. The peak of the slab-averaged $\overline{\theta_l'^2}$ profile is very well defined, such that the values of z_i^+ and z_i^- do not dependent strongly on the rather arbitrary criteria in Eqs. (5.11).

The inversion jump of a conserved variable φ is defined as the difference between the variable at the top and at the base of the inversion layer

$$\Delta\varphi = \varphi(z_i^+) - \varphi(z_i^-). \tag{5.12}$$

5.3 Setup

5.3.1 Forcings and Domain

In Section 5.4 the LWP budget of the Atlantic Stratocumulus Transition EXperiment (ASTEX, Albrecht et al., 1995) case is analyzed, for which the initial conditions and forcings were described by Van der Dussen et al. (2013). The simulation lasts 40 h and features diurnally varying insolation. During the transition, the boundary layer evolves from relatively shallow and well mixed to deep and decoupled with cumulus updrafts underneath a thin broken stratocumulus layer. The results of this case are used here to illustrate how the methodology described in the previous section can help to understand the often complex interaction between processes that together determine the evolution of the stratocumulus layer.

Many of the forcings and boundary conditions for the ASTEX case, such as the subsidence velocity, the solar zenith angle and the geostrophic wind velocities, vary with time. This could make the interpretation of sensitivity experiments unnecessarily complicated. The forcings of the ASTEX case have therefore been idealized for the sensitivity experiments, as follows.

A diurnally averaged solar zenith angle of 68.72° is prescribed, resulting in a constant downwelling shortwave radiative flux of approximately 494 $\mathrm{W\,m^{-2}}$ at the top of the atmosphere. Furthermore, the geostrophic wind velocities are kept constant and equal to the initial horizontal velocities, which are constant with

height at $(u, v) = (5.5, 0)$ m s^{-1}. Hence, the mean wind speed is approximately constant in time. The microphysics parameterization scheme is disabled.

For the sensitivity simulations, the prescribed large-scale subsidence profile is kept constant with time. It is defined as:

$$\overline{w}(z) = \begin{cases} -Dz & \text{for} \quad z \leq z_D \\ -Dz_D & \text{otherwise,} \end{cases}$$

where $z_D = 500$ m and D is the large-scale divergence of horizontal winds. The only boundary condition that varies in time is the SST, which increases linearly from 291 to 297 K over the course of the 60-hour simulations.

The horizontal domain size is 4800×4800 m^2, divided into 192×192 gridpoints that are spaced 25 m apart. In the vertical direction, the resolution is varied from 10 m at the surface to 5 m for z between 500 and 2300 m. Above, the vertical grid spacing is increased by 5 % per level up to a height of 3 km, resulting in a total of 500 levels.

5.3.2 Model Details

The Dutch Atmospheric LES (DALES) model version 4.0 was used to perform the simulations. Compared to version 3.2 that was described by Heus et al. (2010), this version has an anelastic core (Böing et al., 2012). The model settings and parameterization schemes that were used are identical to those described by Van der Dussen et al. (2015).

5.4 ASTEX Transition

The LWP for the ASTEX case is shown in Figure 5.1a as a function of time. The LWP evolution is qualitatively similar to that obtained with DALES version 3.2 (Van der Dussen et al., 2013), despite the fact that different radiation and microphysics parameterization schemes are used in the present study.

The tendency of the LWP is indicated by the thick black line in Figure 5.1b. The thin black line in this figure shows the net LWP tendency diagnosed using Eq. (5.3), which agrees very well with the actual LWP tendency.

Interestingly, the net LWP tendency is small as compared to the contributions from entrainment, radiation and turbulent fluxes at stratocumulus base height. The simulation starts approximately at midnight. During the initial 8 hours, the contribution of the radiation to the LWP tendency is therefore solely due to longwave radiative cooling. This contribution is large and causes the stratocumulus layer to thicken.

The increase of the LWP triggers additional precipitation, so that its thinning contribution increases until it approximately balances the radiative tendency and the net LWP tendency decreases.

After about 8 hours of simulation, the sun rises. The stratocumulus layer absorbs the solar radiation, which causes a warming that partly offsets the longwave radiative cooling so that the net thickening effect due to radiation diminishes during the day. The thinner stratocumulus layer supports only little precipitation, such

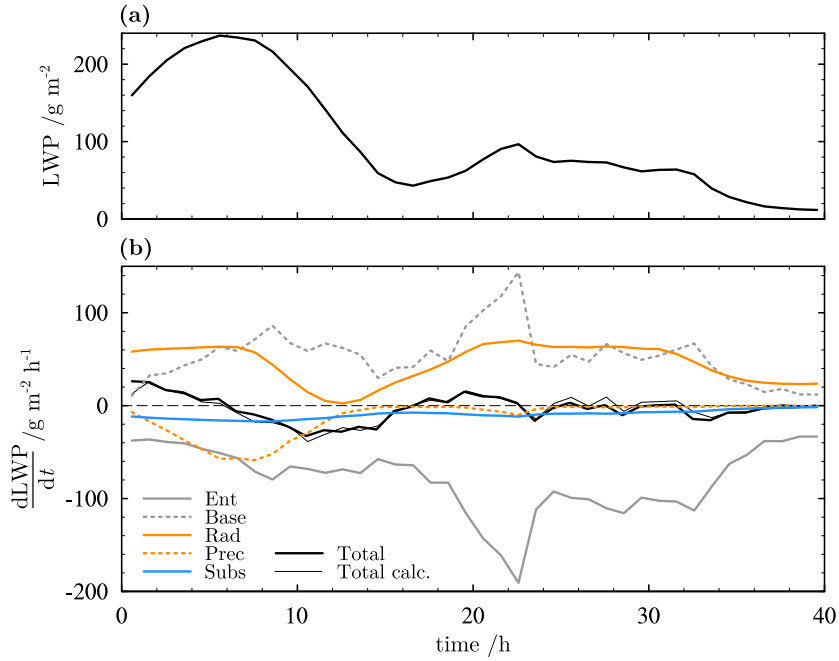

Figure 5.1. (a) The LWP as function of time for the ASTEX transition simulation. (b) The tendency of the LWP as a function of time, split into the contributions from the individual physical processes according to Eq. (5.3). Line colors and styles as denoted by the legend. The horizontal dashed black line indicates the zero tendency level as a reference.

that the thinning tendency due to precipitation reduces to approximately zero. The feedback of the LWP on the generation of precipitation acts as a buffering mechanism, leveling out variations of the LWP on timescales of several hours.

The decrease of the net radiative cooling during the day also diminishes the production of turbulence in the cloud layer, which is reflected by the decrease of the magnitudes of the contributions of the entrainment and of the turbulent fluxes at stratocumulus base. Interestingly, the response of the turbulence intensity to the change of the radiative forcing seems to be delayed somewhat, causing the minimum LWP in Figure 5.1a to occur about two to four hours after midday.

The contribution of the large-scale subsidence to the LWP is relatively small and negative. Its thinning effect decreases as the stratocumulus cloud thins, which is due to the h dependence in Eq. (5.4).

During the second night, after about 20 hours, the thinning due to entrainment is approximately balanced by equal thickening contributions by the radiative cooling and the fluxes at cloud base. Surprisingly, the contributions due to subsidence and precipitation are negligible at this stage. As a result the LWP decreases only very slightly until the cloud layer starts to break up at the beginning of the second day.

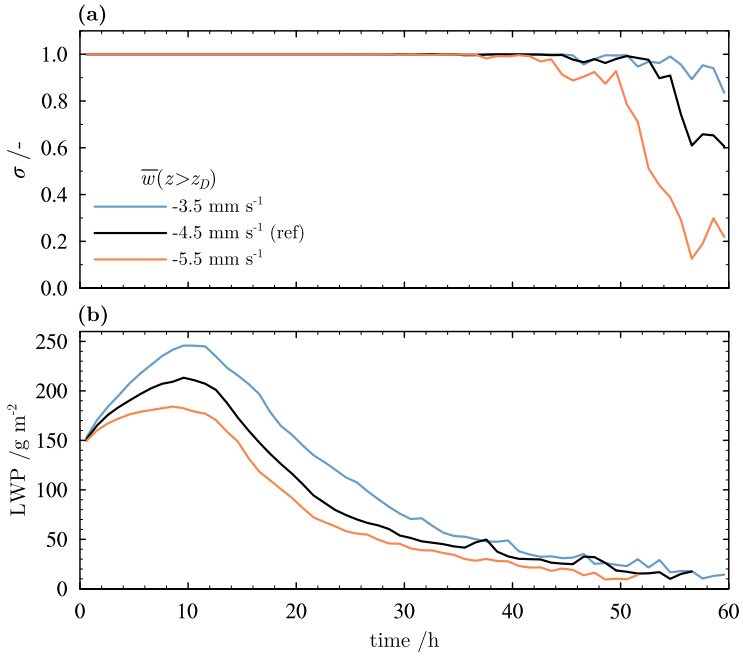

Figure 5.2. (a) The projected cloud cover σ and (b) the LWP as a function of time for the the sensitivity simulations in which the large-scale subsidence velocity is varied as indicated by the legend.

5

5.5 Sensitivity to the Large-scale Subsidence

5.5.1 Effect on Cloud Properties

The projected cloud cover σ is shown in Figure 5.2a for the three sensitivity simulations in which the large-scale subsidence velocity is varied. The results demonstrate clearly that a weakening of the large-scale subsidence extends the lifetime of the stratocumulus layer, thereby corroborating the findings of Svensson et al. (2000) and Sandu and Stevens (2011). Figure 5.2b furthermore shows that a weakening of the subsidence causes the LWP to increase. The large differences among the simulations are somewhat surprising, as it was shown in the previous that the contribution of subsidence to the LWP tendency is relatively small.

Despite the absence of precipitation and a diurnal cycle, the transitions with the idealized forcings are qualitatively similar to the original ASTEX transition (Figure 5.1a). However, the stratocumulus breakup occurs later in the sensitivity experiments. In the second half of the original ASTEX transition, the magnitude of the horizontal wind velocity decreases, which drastically reduces the surface humidity flux and likely causes the transition to accelerate (Van der Dussen et al., 2013). In the sensitivity experiments, on the other hand, the horizontal wind speed is constant in time so that the stratocumulus layer is maintained longer at the end

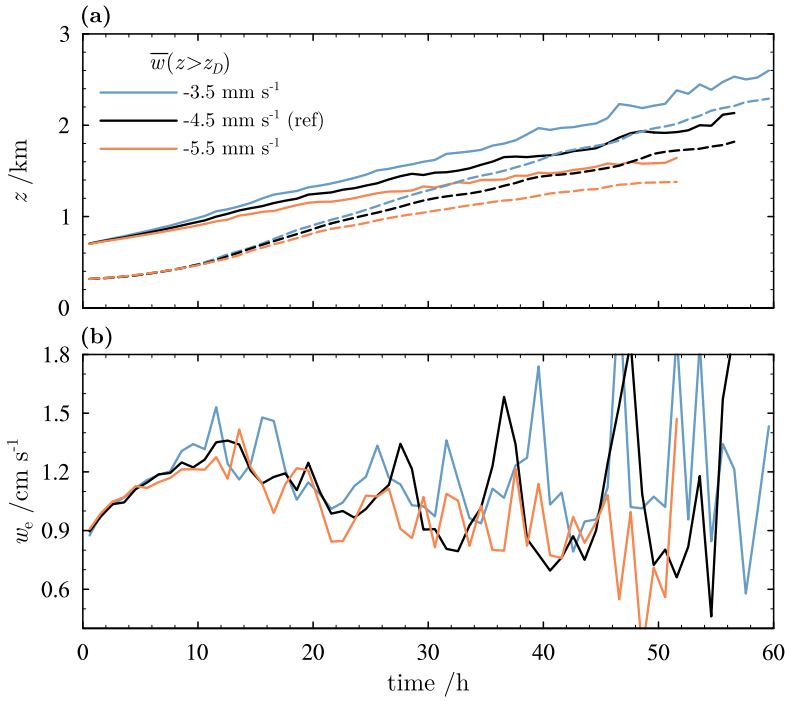

Figure 5.3. (a) The stratocumulus top (solid) and base height (dashed) and (b) the entrainment velocity as a function of time for the subsidence sensitivity simulations.

of the transition.

Figure 5.3a shows the top and base interfaces of the stratocumulus layer as defined in Section 5.2.2. Differences in stratocumulus top height start to occur soon after the start of the simulations. Stratocumulus base height, on the other hand, remains unaffected for roughly 15 hours. This suggests that the difference in the subsidence velocity does not strongly affect the temperature and humidity profiles in the bulk of the boundary layer during this period. Later on in the simulations, differences in the stratocumulus base height also start occurring.

It is interesting to note that the differences of the inversion height among the simulations are roughly a factor of two larger than would be expected on the basis of the difference in the subsidence rate alone. As can be seen in Figure 5.3b, the entrainment rate is found to increase as subsidence weakens. Such an increase was also found by Sandu and Stevens (2011) and it is most likely the result of the larger stratocumulus thickness h, which typically causes the cloud layer to be more energetic eventually leading to enhanced entrainment (e.g. Nicholls and Turton, 1986; Jones et al., 2014).

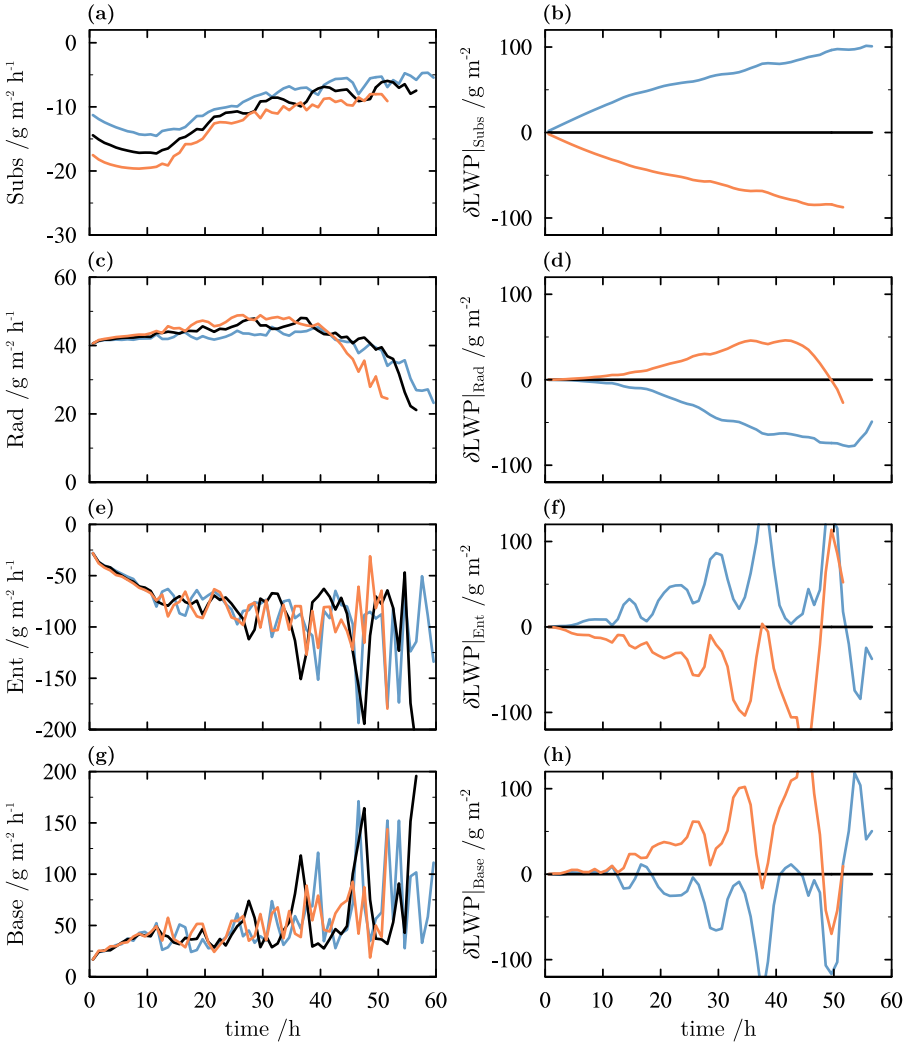

Figure 5.4. The LWP tendencies due to (a) subsidence, (c) radiation, (e) entrainment and (g) cloud base turbulent fluxes as a function of time for each of the sensitivity simulations. The LWP differences with the reference (black) due to each of these processes have been calculated according to Eq. (5.13) and are shown in panels (b), (d), (f) and (h), respectively. Colors according to the legend in Figure 5.3a.

5.5.2 Analysis of LWP Budget

To determine how much each of the physical processes that affect the LWP contribute to the LWP differences among the simulations, the terms of the LWP budget equation are shown individually in the left column of Figure 5.4. Note that the scale of the vertical axis of the subfigures varies significantly.

Figure 5.4a shows the LWP tendency due to subsidence. Evidently, the cloud thinning due to subsidence is less strong for the weaker subsidence cases. The difference among the simulations is about $3\,\mathrm{g\,m^{-2}\,h^{-1}}$ during the first part of the transition and slowly decreases with time. For the LWP tendencies due to radiation, entrainment and cloud base turbulent fluxes, shown in Figures 5.4c, 5.4e and 5.4g respectively, the data do not show a clear trend due to the significant amount of noise.

In order to obtain a clearer picture of how large the LWP differences caused by each of the individual processes are, the following steps are taken. First, the $-Dz_D = -4.5\,\mathrm{mm\,s^{-1}}$ simulation indicated by the black lines in Figures 5.2 and 5.3 is chosen as a reference. Then, the differences with respect to this reference of the LWP tendency due to each process is determined. These differences are integrated in time to give the LWP difference among the simulations that is solely due to that process. So, for the subsidence term

$$\delta\mathrm{LWP}\big|_{\mathrm{Subs}}(t) = \int_0^t \delta\mathrm{Subs}(t')\mathrm{d}t' = \int_0^t \mathrm{Subs}(t') - \mathrm{Subs}^{\mathrm{r}}(t')\mathrm{d}t', \tag{5.13}$$

where δ denotes the difference of a variable with respect to the reference simulation that is denoted by a superscripted 'r'. Similarly, the LWP differences solely due to the Rad, Ent and Base terms in Eq. (5.5) to (5.7) were calculated. The results are shown for each of the processes by the plots in the right hand column of Figure 5.4.

The LWP difference caused solely by subsidence is shown in Figure 5.4b. Consider the simulation indicated by the blue line, which has a weaker subsidence as compared to the reference simulation. The smaller cloud thinning tendency due to subsidence for this case causes a positive contribution to the LWP difference, δLWP, that increases approximately linearly with time up to a value of about $100\,\mathrm{g\,m^{-2}}$.

The absorption of shortwave radiation by a stratocumulus layer increases with the LWP (Van der Dussen et al., 2013). So, as subsidence is weakened and the LWP increases, the absorption of shortwave radiation also increases. The net cloud thickening effect due to radiative cooling is therefore reduced. Hence, the LWP difference with the reference is negative for the weak subsidence simulation (Figure 5.4d) and compensates for much of the LWP difference due to subsidence in the second part of the transition.

The LWP difference as a results of entrainment is less straightforward to understand. In the previous section, it was shown that the entrainment rate is largest for the weakest subsidence simulation. As entrainment causes drying and warming of the stratocumulus layer, this higher entrainment velocity is expected to cause a negative contribution to δLWP. However, Figure 5.4f shows that it is the other way around: for the lowest subsidence case with the highest entrainment rate, the contribution of entrainment to δLWP is positive. This has two main causes. First, the magnitude of the inversion jump of humidity Δq_{t} decreases as subsidence is weakened. This decrease exceeds $0.5\,\mathrm{g\,kg^{-1}}$ or 10 % at the end of the simulations and weakens the drying of the stratocumulus layer due to entrainment. Second, the equation for the contribution of entrainment to the LWP tendency in Eq. (5.5) consists of three terms. The last of these terms accounts for the deepening of the cloud layer due to entrainment. This term increases with the cloud thickness h.

For the weak subsidence simulation, h is greater than for the reference simulation. Together with the smaller Δq_t, this causes the cloud thinning tendency due to entrainment to be less strong for the weak subsidence case, despite the higher entrainment rate.

Figure 5.4h shows the contribution of cloud base turbulent fluxes to δLWP. The boundary layer is deepest for the weak subsidence simulation, which causes a slight reduction of the turbulent transport of humidity to the cloud layer. Hence, the contribution of the cloud base fluxes to δLWP is on average negative for the weak subsidence simulation indicated by the blue line.

From the comparison of Figures 5.4f and 5.4h it is clear that the cloud base turbulent fluxes contribution to δLWP is strongly anticorrelated with that of entrainment. The sum of both contributions is therefore almost zero. In other words, the net effect of these turbulent fluxes to the LWP difference among the cases is very small. The LWP differences in Figure 5.2b are therefore mainly due to the direct effect of large-scale subsidence on the LWP tendency and the subsequent change of the absorption of shortwave radiation.

5.6 Conclusions

Several studies have shown that as a result of warming of the climate the Hadley circulation might weaken, leading to a weakening of the large-scale subsidence in the subtropical stratocumulus areas. Several modeling studies (Svensson et al., 2000; Sandu and Stevens, 2011) and recent observational evidence (Myers and Norris, 2013) suggest that such a decrease can lead to thicker and more persistent stratocumulus clouds.

To investigate how the large-scale subsidence affects stratocumulus layers, a method is applied in the current study to analyze the individual contributions of five different physical processes to the LWP tendency of an adiabatic stratocumulus layer. As an illustration of the use of this method, it was first applied to LES results of the ASTEX stratocumulus transition (Van der Dussen et al., 2013). The results show among others that subsidence tends to reduce the LWP by pushing down the cloud top. Longwave radiative cooling tends to increase the LWP, while the absorption of shortwave radiation during the day diminishes the net radiative effect. Entrainment dries and warms the cloud layer resulting in a strong cloud thinning effect that increases as the transition progresses. The transport of humidity toward the cloud layer by turbulent fluxes counteracts this drying, causing a significant positive effect on the LWP tendency. The results furthermore indicate that the cloud thinning contribution of the large-scale subsidence is small as compared to the other contributions.

Despite this relatively small contribution to the LWP tendency, more idealized sensitivity simulations show that decreasing the subsidence velocity extends the lifetime of the stratocumulus layer. Moreover, it causes the LWP to be significantly higher throughout the entire transition. The thicker stratocumulus layer in the weak subsidence cases tends to absorb more solar radiation, which partly offsets the LWP difference due to subsidence in the second part of the simulations.

It was shown that a weakening of the large-scale subsidence causes enhanced

entrainment that amplifies the differences of the inversion height among the simulations. Counterintuitively, this higher entrainment rate does not result in a stronger cloud thinning tendency with respect to the reference simulation, which is likely due to a reduction of the magnitude of the inversion jumps of q_t and θ_l and the greater cloud thickness.

The cloud thickening contribution of the cloud base turbulent fluxes decreases somewhat for the weaker subsidence cases as a result of the greater boundary layer depth. This decrease is strongly anticorrelated to the LWP increase as a result of entrainment, such that the total contribution of the turbulent fluxes to the LWP difference among the cases is negligible.

The results of the current study suggest that it is likely that a weakening of the large-scale subsidence in the subtropics due to the weakening of the Hadley circulation in a future climate increases the average LWP as well as the occurrence of subtropical stratocumulus clouds.

Acknowledgments

The investigations were done as part of the European Union CLoud Intercomparison, Process Study & Evaluation (EUCLIPSE) project, funded under Framework Program 7 of the European Union. The work was sponsored by the National Computing Facilities Foundation (NCF) for the use of supercomputer facilities.

6

Conclusions and Outlook

6.1 Stratocumulus Transitions

One of the aims of this thesis project was to identify the main mechanisms responsible for the thinning and breaking up of stratocumulus clouds during stratocumulus transitions. To this end, we have used large-eddy simulation (LES) to simulate such stratocumulus transitions.

In chapter 2, an LES model intercomparison study is presented that was based on the observed ASTEX stratocumulus transition case. The aim is to validate the capability of LES models to faithfully capture an observed transition. The results of six different LES models are compared to the observations, showing that many features of the observed transition are well represented in the simulations. These features include the rate at which the boundary layer gradually deepened during the 40-hour transition. After 20 hours of simulation cumulus clouds are present that rise from the top of the subcloud layer into the stratocumulus layer above. The onset of the shallow cumulus convection as well as the observed break up of the stratocumulus cloud layer at the end of the transition are well captured by the LES models. These results prove that LES models are well suited for the realistic simulation of stratocumulus transitions.

Similar to the observations, the deepening of the boundary layer causes a separation of the initially well-mixed boundary layer into a two-layered system with a relatively moist and cool subcloud layer below a warmer and drier stratocumulus cloud layer. The corresponding vertical velocity variance profile was shown to exhibit a clear double-peaked structure with a local minimum approximately half way between the surface and the inversion. The double peak structure indicates that the boundary layer is split into two turbulent layers that only weakly interact with each other. This phenomenon is commonly referred to as decoupling. Decoupling of the boundary layer has been hypothesized to reduce the vertical transport of moisture significantly, leading to the thinning and breaking up of stratocumulus clouds (e.g. Nicholls, 1984; Bougeault, 1985). It is difficult to test this hypothesis on the basis of the aircraft observations as they are available at only a few moments during the transition. The LES results on the other hand are available at high temporal resolution for the entire duration of the transition

and they hence constitute a valuable extension of the observations. From the LES results, the moisture transport from the subcloud layer toward the stratocumulus layer was quantified by determining the ratio of the turbulent humidity flux at the top of the subcloud layer over that at the stratocumulus cloud base. It was found that during the day, the humidity transport out of the subcloud layer was limited causing a moistening of the subcloud layer. During the night however, the humidity transport toward the stratocumulus cloud even exceeded the surface flux of humidity, resulting in a resupply of moisture to the stratocumulus layer. On average about 95 % of the moisture evaporating from the surface reached the stratocumulus layer during the first 24 hours of the transition, which suggests that decoupling does not strongly limit the transport of humidity out of the subcloud layer toward the stratocumulus cloud. De Roode et al. (2012) showed similar results from LES results of the composite transition cases of Sandu and Stevens (2011).

Another mechanism that has been proposed in literature as a cause for the breakup of stratocumulus clouds is Cloud Top Entrainment Instability (CTEI) (Deardorff, 1980a; Randall, 1980). The main idea of CTEI is that if the free troposphere above the stratocumulus cloud is sufficiently cool and dry, the air parcels that are entrained can become negatively buoyant as a result of the cooling induced by the evaporation of cloud water. As the negatively buoyant parcels start to sink, they generate turbulence, which enhances the entrainment rate and the influx of air from the free troposphere above the inversion into the cloud layer. This positive feedback process was believed to cause a rapid thinning and breaking up of the stratocumulus layer, making it a potential key mechanism controlling the breakup of stratocumulus clouds.

A criterion for the occurrence of CTEI can be expressed in terms of an inversion stability parameter κ, which basically is the ratio of the inversion jumps of liquid water potential temperature and total specific humidity. Some LES studies suggest that stratocumulus cloud cover indeed tends to rapidly decrease as the CTEI criterion is exceeded (Moeng, 2000; Lock, 2009), but observations showed that closed stratocumulus decks can be maintained for such conditions (Kuo and Schubert, 1988; Stevens et al., 1998). Results from high-resolution numerical simulations furthermore indicate that the feedback process of buoyancy reversal on the entrainment rate is weak (Yamaguchi and Randall, 2008; Mellado et al., 2009).

In chapter 3, the work of Randall (1984) was used as a starting point to derive a budget equation describing the rate of change of the stratocumulus liquid water path (LWP) in terms of all relevant physical processes. Besides entrainment, these processes include radiation, the turbulent fluxes of humidity and heat at the stratocumulus cloud base, precipitation and subsidence. From this budget equation it could be shown that the cloud thinning tendency as a result of entrainment increases smoothly with the value of the inversion stability parameter. This is different from CTEI, for which an abrupt thinning and breaking up of the cloud layer is expected as soon as a critical value of the inversion stability parameter is exceeded. The analysis in chapter 3 shows that the stratocumulus cloud can be maintained far into the CTEI regime, provided that cloud building processes, most importantly the transport of moisture that evaporates from the surface toward the cloud layer, are strong enough. Without this transport the stratocumulus layer

will quickly dissolve under the influence of entrainment.

In summary, it is argued in chapter 3 that the assumption of CTEI is not required to explain the LES results that show that stratocumulus clouds tend to break up as κ increases toward unity (Moeng, 2000; Lock, 2009). At the same time, it explains the observations of persistent stratocumulus clouds far into the CTEI regime. Together with the existing numerical and laboratory evidence showing that the CTEI mechanism is very weak for realistic stratocumulus conditions (Siems et al., 1990; Yamaguchi and Randall, 2008; Mellado et al., 2009), this makes it unlikely that CTEI plays a role in the breaking up of stratocumulus clouds.

The LWP budget equation derived in chapter 3 allowed us to quantify the contribution of individual processes, such as entrainment or radiative cooling, to the thickening or thinning of a stratocumulus cloud. We took advantage of this budget equation in chapter 5 to investigate the effect of varying the large-scale subsidence in a set of LESs of stratocumulus transitions. This research was motivated by the results of Svensson et al. (2000) and Sandu and Stevens (2011), who showed that a weakening of the large-scale subsidence tends to cause a thickening of stratocumulus clouds and a delay in the timing of the breakup of these clouds during stratocumulus transitions. Interestingly, in their simulations the stratocumulus transition was delayed despite an increase of the entrainment rate, which is typically associated with more drying and warming and hence a stronger thinning tendency of the stratocumulus cloud.

Our simulations confirmed the results of Sandu and Stevens (2011). Using the budget equation it was shown that the LWP differences among the cases were mainly the direct result of the differences in the subsidence rate. This can be expected, as a reduction of the large-scale subsidence velocity leads to a deeper boundary layer and hence a thicker stratocumulus cloud. The resulting LWP differences are damped by the absorption of solar radiation, which increases as the LWP of the stratocumulus cloud increases. Surprisingly, we found a decrease of the cloud thinning tendency due to entrainment, despite an increase of the entrainment velocity. This weaker cloud thinning due to entrainment was explained by a decrease of the inversion jump of humidity and the increased stratocumulus thickness.

In earlier studies (e.g. Wyant et al., 1997), it was argued that the deeper boundary layers resulting from a reduction of the large-scale subsidence would be more strongly decoupled and hence the moisture transport to the stratocumulus cloud layer would be decreased. Hence, a reduction of the large-scale subsidence was hypothesized to lead to an earlier break up of the stratocumulus layer, which is the opposite to what we found in the LES results. We confirmed that the turbulent humidity flux at the stratocumulus cloud base decreased as the large-scale subsidence was weakened, implying a reduction of the cloud building effect. However, this reduction was strongly anticorrelated with the reduced cloud thinning effect due to entrainment. The change of the entrainment effect therefore almost completely cancels the change of the turbulent humidity flux at cloud base, so that together they hardly influence the total LWP tendency.

Several studies suggest that the Hadley circulation will weaken in a future warmer climate, causing a weakening of the large-scale subsidence in subtropical regimes of the planet (e.g. Held and Soden, 2006; Vecchi and Soden, 2007). Our

results suggest that this weakening could lead to thicker and more persistent stratocumulus clouds. This implies a negative cloud-climate feedback, which is in accordance with the findings of Bretherton et al. (2013). They investigated the sensitivity of stratocumulus and cumulus-under-stratocumulus steady-state solutions to several idealized climate perturbations using LES and found that a decrease of the large-scale subsidence led to a thickening of the stratocumulus layer.

6.2 Stratocumulus Steady States

The change of the stratocumulus cloud amount as a result of the warming climate remains an important cause of uncertainty in climate models. We investigated the physical mechanisms responsible for the change of the stratocumulus cloud amount in a future climate in chapter 4, by performing a set of 25 idealized LESs in which the free-tropospheric temperature and humidity were systematically varied. These two parameters have been found to strongly affect, among others, the stratocumulus cloud thickness and the entrainment velocity (Klein and Hartmann, 1993; Chlond and Wolkau, 2000). The framework for this study was designed by Dal Gesso et al. (2014b) who based their setup on the CGILS cumulus-under-stratocumulus case (Blossey et al., 2013; Bretherton et al., 2013). Following these studies, we prescribed a constant diurnally averaged solar zenith angle and insolation at the top of the atmosphere and we ran the simulations long enough for the stratocumulus-topped boundary layer to reach an approximate steady state. These idealizations greatly simplified the analysis of the results.

For all free tropospheric conditions a completely overcast boundary layer was found. Interestingly, the LWP of the stratocumulus clouds was mainly a function of the free tropospheric humidity as more humid free tropospheric conditions favor lower entrainment rates and hence less drying and warming of the cloud layer by entrainment. Variations in the temperature of the free troposphere on the other hand hardly affected the LWP for these experiments.

In the second part of chapter 4 the response of marine stratocumulus-topped boundary layers to an idealized climate change scenario was investigated. To this end, a second set of 25 simulations was performed in which the initial temperatures of the atmosphere and the sea surface were increased by 2 K, while the initial relative humidity profile was kept constant. In response to this idealized climate perturbation, the stratocumulus clouds thinned for all free tropospheric conditions that were considered. This positive cloud-climate response is consistent with several recent studies (Bretherton et al., 2013; Bretherton and Blossey, 2014; Dal Gesso et al., 2014b,a). It was furthermore shown that the magnitude of the LWP decrease is not constant, but depends significantly on the free tropospheric conditions. For dry and warm free tropospheric conditions, the LWP decrease as a result of the idealized climate perturbation is smallest.

From the results of the relatively large set of simulations, it was argued that the positive cloud-climate feedback for this particular climate perturbation is mainly attributable to the increase of the bulk humidity difference between the free troposphere and the sea surface. This results in a decrease of the steady-

state relative humidity of the stratocumulus layer as compared to the reference simulations and hence in a thinner cloud layer. The LES results presented in chapter 4 were furthermore used by Dal Gesso et al. (2015) to evaluate how well six single-column models (SCMs) represented the variation of, among others, the steady-state inversion height and the LWP throughout the same phase space. On average the climate response found from the SCM results was positive and hence agreed with the LES results. However, the sign and magnitude of the response varied significantly throughout the phase space. The LES results provided an important benchmark for the SCMs in this study, by showing that there is no physical cause for the irregular behavior of the results within the phase space. Furthermore, they showed that the SCMs are in general not sensitive enough in terms of the inversion height to changes in the free tropospheric conditions.

As part of the second phase of the CGILS model intercomparison project, the stratocumulus response to a quadrupling of the atmospheric CO_2 concentration was furthermore investigated (Blossey et al., 2015). Since such an increase in the greenhouse gas concentration enhances the emissivity of the atmosphere, the incoming downwelling longwave radiation at the top of the stratocumulus cloud is increased. This, in turn, decreases the net longwave radiative cooling of the cloud, which results in reduced entrainment and a decrease of the steady-state inversion height by approximately 100 m as compared to the control case. The decreased inversion height leads to a net thinning of the cloud layer and hence suggests a positive cloud-climate feedback. The response to the quadrupling of the CO_2 concentration was very consistent among the five LES models that participated in the intercomparison study.

In a second experiment a composite climate perturbation was applied, based on the results of the third climate model intercomparison project (CMIP3). This composite perturbation consisted of, among others, a doubling of the free tropospheric CO_2 concentration, an increase of the temperature by more than 2 K and a reduction of the large-scale subsidence velocity. Similar to the quadrupled CO_2 experiment, a decrease of the inversion height was found despite the weakened subsidence, which resulted in an overall positive cloud-climate feedback.

Each of the climate change experiments performed as part of this thesis project indicate that the stratocumulus cloud amount and reflectivity in the subtropics will most likely be reduced in a future warmer climate, since all climate perturbations investigated, with the exception of a weakening of the subsidence velocity, result in a significant decrease of the LWP. Furthermore, the response among different LES models is very consistent.

6.3 Outlook

As discussed in the previous section, the steady-state phase space experiments provided some valuable new insights on the sensitivity of stratocumulus clouds on the free tropospheric conditions and their response to idealized climate perturbations. It was shown that in particular for those cases within the phase space with the deepest boundary layers, the total specific humidity in the subcloud layer was much higher than in the stratocumulus layer, which indicates decoupling. From

the structure of the boundary layer it was obvious that the turbulence was mainly driven by radiative cooling at the top of the stratocumulus cloud. The surface buoyancy flux was relatively small as a result of the negative surface sensible heat flux. In realistic stratocumulus-topped boundary layers, this is typically not the case and turbulence is often also driven from the surface. Including horizontal advection of cold and dry air will tend to enhance the surface sensible and latent heat fluxes, both of which will tend to increase the surface buoyancy flux. It is therefore worthwhile to extend our phase-space simulations with horizontal advection, similar to the CGILS experiments.

Note that, in order to maintain an equilibrium in the free troposphere, a uniform cooling must be balanced by enhanced subsidence warming. On the other hand, a uniform drying as a result of horizontal advection cannot be balanced by changing the subsidence velocity. Hence, it is not possible to achieve a steady state in the free troposphere in the presence of advective drying. A possible solution is to add the horizontal advective tendencies only in the boundary layer, as was done for in the CGILS experiments. For the entire phase space, this means that the tendency should only be applied in the lowest approximately 500 m as the inversion height greatly varies in time and among the individual cases.

In chapter 3 the LWP budget equation was presented, that was subsequently used in chapter 5 as an effective evaluation method to determine which processes are responsible for the LWP differences among the sensitivity simulations. Although this methodology was exclusively used in a Lagrangian framework here, it can be useful in Eulerian experiments as well, for instance to interpret differences among model results in future intercomparison studies. When applicable, the effects of horizontal advection on the LWP budget can straightforwardly be accounted for (Ghonima et al., 2015).

The results presented in this thesis demonstrate the usefulness of LES models for the research of stratocumulus clouds and their transition. As a consequence, the validity of the conclusions depends to a large extent on the reliability of the LES results. It is therefore important to critically assess possible weaknesses of LES models and to continue improving them. For instance, it became obvious that the numerical advection scheme used in DALES was not suitable for the accurate representation of the strong gradients in the inversion region. As described in Appendix A, a new advection scheme was therefore added to the model as part of this thesis project.

In addition, the model intercomparison study presented in chapter 2 provided an excellent opportunity to identify the main differences among different models. As was mentioned earlier, the six LES models that participated in the model intercomparison study agreed well on many of the features of the observed stratocumulus transition. The most significant differences were found in the representation of the LWP during the first night of the transition. From the intercomparison of the results from the LES models and after performing several sensitivity simulations using DALES, the microphysics parameterization was identified to be the main cause for these differences. The reduction of the variability resulting from microphysics schemes should therefore receive a high priority.

Unfortunately, the uncertainty in the observations was too large to determine which of the models produced the most realistic precipitation rates. For this

reason, more recent measurement campaigns have been focusing specifically on obtaining accurate precipitation observations in stratocumulus clouds (Stevens et al., 1998; Ackerman et al., 2009). The data from such experiments provide excellent opportunities to identify the strengths and weaknesses of current microphysics schemes, thereby giving which will help to reduce the uncertainty among them. It has furthermore been shown that large-scale cell formation in stratocumulus-topped boundary layers significantly affect precipitation rates (e.g. Stevens et al., 2005a; Sandu and Stevens, 2011). Larger domain sizes are also important to capture the variability that is present at scales up to 100 km (Stevens et al., 2002; De Roode et al., 2004). The increase of the computational resources and the development of numerical codes on alternative architectures (Schalkwijk et al., 2011) should certainly be employed to increase the domain size for future LESs to also include this variability.

A

Numerical Advection of Scalars

A.1 Momentum and Scalar Conservation

By applying momentum conservation on fluid parcels, C.-L. Navier and G. B. Stokes derived equations that describe the flow velocities of fluids. For incompressible flow, these so-called Navier-Stokes equations can be written as:

$$\frac{\partial u_i}{\partial t} + u_j \frac{\partial u_i}{\partial x_j} = -\frac{1}{\rho}\frac{\partial p}{\partial x_i} + f_i, \tag{A.1}$$

where x_i denotes the position in the i-th direction of the Cartesian coordinate system, t is time, ρ denotes the density of the fluid, p is pressure and $u_i = \partial x_i / \partial t$ is velocity. Other forces that act on the body of the fluid, such as the gravitational and the Coriolis force, are denoted by f. The effects of molecular viscosity are neglected.

In the Boussinesq approximation, the continuity equation is as follows

$$\frac{\partial u_j}{\partial x_j} = 0. \tag{A.2}$$

This approximation is the basis of DALES version 3.2 (Heus et al., 2010) that was used to perform the simulations described in chapter 2 of this thesis.

The simulations in chapters 4 and 5 have been performed with DALES 4. In the derivation of the momentum equations for this model version, the anelastic approximation is used instead of the Boussinesq approximation (Böing, 2014). In the anelastic approximation, the continuity equation becomes

$$\frac{\partial}{\partial x_j}\rho_0(z)u_j = 0. \tag{A.3}$$

Here, $\rho_0(z)$ is the base state density profile that is kept constant in time. For consistency, $\rho_0(z)$ was set constant in height, such that effectively the continuity equation of Eq. (A.2) was used for all simulations presented in this thesis.

Using Eq. (A.2), the second term on the left hand side of Eq. (A.1) can be rewritten as follows

$$u_j \frac{\partial u_i}{\partial x_j} = \frac{\partial}{\partial x_j} u_j u_i. \tag{A.4}$$

Equation (A.1) then becomes

$$\frac{\partial u_i}{\partial t} + \frac{\partial}{\partial x_j} u_j u_i = -\frac{1}{\rho}\frac{\partial p}{\partial x_i} + f_i. \tag{A.5}$$

Similarly, the prognostic equation for a conserved variable φ is

$$\frac{\partial \varphi}{\partial t} + \frac{\partial}{\partial x_j} u_j \varphi = S_\varphi, \tag{A.6}$$

where S_φ accounts for any sources or sinks due to diabatic processes such as precipitation and radiation.

Starting from Eqs. (A.5) and (A.6), Böing (2014) derived the filtered conservation that are solved in DALES, while a thorough discussion of the filtering procedure is provided by e.g. Pope (2000). Heus et al. (2010) furthermore describe the implementation of among others boundary conditions, large-scale forcing terms and parameterization schemes for radiation and microphysics in DALES.

In this appendix, some challenges regarding the discretization of the advection term for scalars, $\partial u_j \varphi / \partial x_j$, are discussed. Moreover, the hybrid advection scheme is described that was added to DALES as part of this thesis project.

A.2 Advection Equation in Flux Form

For one-dimensional advection in the absence of sources or sinks, Eq. (A.6) reduces to

$$\frac{\partial \varphi}{\partial t} + \frac{\partial}{\partial x}(u\varphi) = 0. \tag{A.7}$$

Often, this equation is written in a semi-discrete flux form,

$$\frac{\partial \varphi_i}{\partial t} = -\frac{1}{\mathrm{d}x_i}\left(f_{i+\frac{1}{2}} - f_{i-\frac{1}{2}}\right), \tag{A.8}$$

in which φ_i denotes the cell-averaged value of φ at position x_i, $f_{i-\frac{1}{2}}$ and $f_{i+\frac{1}{2}}$ are the fluxes through the left and right cell interfaces respectively, and $\mathrm{d}x_i = x_{i+\frac{1}{2}} - x_{i-\frac{1}{2}}$ is the distance between the cell faces as indicated by the schematic in Figure A.1. For simplicity, an equidistant grid is assumed, such that $\mathrm{d}x_i = \mathrm{d}x$. The flux f is simply the product of the velocity and the scalar concentration φ that is being advected at the cell interface:

$$f_{i+\frac{1}{2}} = u_{i+\frac{1}{2}} \varphi_{i+\frac{1}{2}}. \tag{A.9}$$

A.3 Interpolation

The variables in DALES are discretized on an Arakawa staggered C-grid, which means that the velocities are defined at the grid interfaces (Arakawa and Lamb, 1977; Heus et al., 2010). Therefore, the $u_{i\pm\frac{1}{2}}$ in Eq. (A.9) are known. Scalars, on the other hand, are defined at cell centers such that some form of interpolation is required to approximate $\varphi_{i\pm\frac{1}{2}}$.

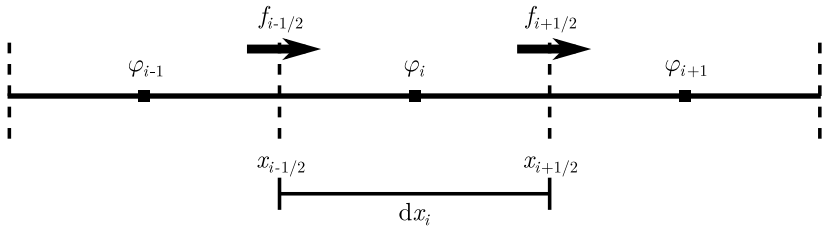

Figure A.1. Schematic representation of the computational grid used. Squares and vertical dashed lines indicate cell centers and edges respectively.

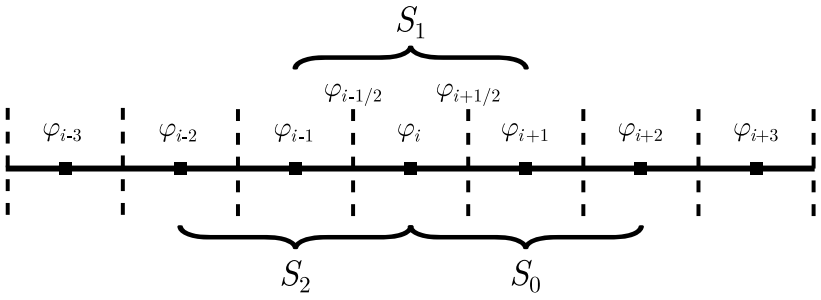

Figure A.2. Schematic representation of different stencils S_l that can be chosen for a third-order advection scheme.

In general, an rth-order accurate interpolation scheme can be written as (Durran, 2010):

$$\hat{\varphi}_{i+\frac{1}{2}} = \sum_{s=0}^{r-1} c_{l,s}\varphi_{i-l+s}. \tag{A.10}$$

Here, $\hat{\varphi}_{i+\frac{1}{2}}$ denotes the approximation of φ at $x_{i+\frac{1}{2}}$. The subscripted l denotes the left shift of the interpolation scheme. By selecting a higher value for l, the set of grid point values that is used by interpolation scheme to find $\hat{\varphi}_{i+\frac{1}{2}}$ shifts to the left. Now, an interpolation scheme can be derived by choosing the desired order of accuracy r and a corresponding left shift $|l| \leq r-1$. For flow moving from left to right, upwind schemes are defined by $l > 0$. Downwind schemes can also be derived, but their use causes advection schemes to become unstable.

Suppose a second-order ($r = 2$), central-difference ($l = 0$) scheme is desired. The following can then be written according to Eq. (A.10):

$$\begin{aligned}\hat{\varphi}(x_{i+\frac{1}{2}}) &= c_{0,0}\varphi(x_i) + c_{0,1}\varphi(x_{i+1}) \\ &= c_{0,0}\varphi\left(x_{i+\frac{1}{2}} - \frac{\mathrm{d}x}{2}\right) + c_{0,1}\varphi\left(x_{i+\frac{1}{2}} + \frac{\mathrm{d}x}{2}\right).\end{aligned} \tag{A.11}$$

Taylor expansion of the terms on the right hand side of this equation gives:

$$\hat{\varphi}(x_{i+\frac{1}{2}}) = (c_{0,0} + c_{0,1})\varphi(x_{i+\frac{1}{2}}) + (c_{0,0} - c_{0,1})\frac{\mathrm{d}x}{2}\frac{\partial\varphi}{\partial x} + \mathcal{O}\left[(\mathrm{d}x)^2\right]. \tag{A.12}$$

For the coefficients, the following must thus be true:

$$\begin{aligned} c_{0,0}+c_{0,1} &= 1 \\ c_{0,0}-c_{0,1} &= 0 \end{aligned} \tag{A.13}$$

This system of equations is solved by letting $c_{0,0} = c_{0,1} = 1/2$. Equations (A.9), (A.10) and (A.13) therefore together define the following central-difference advection scheme:

$$\hat{f}^{\mathrm{2nd}}_{i+\frac{1}{2}} = \frac{u_{i+\frac{1}{2}}}{2}(\varphi_{i+1} + \varphi_i). \tag{A.14}$$

The error in Eq. (A.12) is of second order in $\mathrm{d}x$. The division by $\mathrm{d}x$ in Eq. (A.8) reduces this error to $\mathcal{O}[(\mathrm{d}x)^3]$, and hence the scheme is second-order accurate.

Higher-order and off-center advection schemes can be derived in a similar fashion. An example is the sixth-order accurate central-difference scheme that is also included in DALES and can be written as (Wicker and Skamarock, 2002):

$$\begin{aligned} \hat{f}^{\mathrm{6th}}_{i+\frac{1}{2}} = \\ \frac{u_{i+\frac{1}{2}}}{60}\left[37(\varphi_{i+1} + \varphi_i) - 8(\varphi_{i+2} + \varphi_{i-1}) + \varphi_{i+3} + \varphi_{i-2}\right]. \end{aligned} \tag{A.15}$$

The sixth-order approximation in this equation obviously requires information on φ from positions further away from the cell edge of interest than the second-order approximation in Eq. (A.14). The set of grid indices that is considered in approximating φ at a cell face is sometimes referred to as the stencil S_l, where l is again the left shift. So the stencil of the second-order central scheme consists of grid indices i and $i+1$, or

$$S_{l=0} = \{i, i+1\}. \tag{A.16}$$

The stencil of the sixth-order central scheme is much wider:

$$S_{l=0} = \{i-2, i-1, i, i+1, i+2, i+3\}. \tag{A.17}$$

Figure A.2 schematically shows how l affects the stencil of a third-order approximation.

Typically, computationally cost of using an advection scheme increases significantly as its stencil becomes wider. Low-order schemes with compact stencils are therefore attractive and often used.

A

A.4 Dispersion

Figure A.3 shows the results of the one-dimensional advection of a step function from left to right at a constant velocity using the forward Euler time discretized advection equation:

$$\varphi_i^{t+\mathrm{d}t} = \varphi_i^t - \frac{\mathrm{d}t}{\mathrm{d}x}\left(f^t_{i+\frac{1}{2}} - f^t_{i-\frac{1}{2}}\right). \tag{A.18}$$

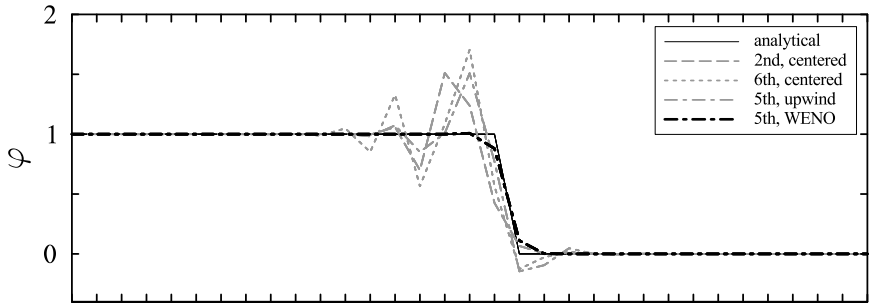

Figure A.3. An example of the advection of a step function from the left to the right. The velocity is constant in time and space and is such that the discontinuity travels exactly half a grid size per time step. The results shown are obtained after 4 time steps. Ticks on the horizontal axes indicate cell centers.

The dashed and the dotted lines indicate the results of the numerical integration of this equation using the second-order central scheme of Eq. (A.14) and the sixth-order central scheme of Eq. (A.15), respectively, to approximate the fluxes at the cell edges $f_{i\pm\frac{1}{2}}$. Both results show strong oscillatory behavior behind the discontinuity. The oscillations are caused by the fact that the wave propagation velocity is a function of the wavelength, a phenomenon called dispersion. This can relatively easily be demonstrated for the second-order central scheme, as follows.

First, by combining Eqs. (A.8) and Eq. (A.14) for a constant velocity, a differential-difference equation can be written:

$$\frac{\partial \varphi_i}{\partial t} + \frac{u}{2\mathrm{d}x}\left(\varphi_{i+1} - \varphi_{i-1}\right) = 0. \tag{A.19}$$

A solution to this equation for a single wave number k is

$$\varphi_i = e^{j(ki\mathrm{d}x - \omega t)}, \tag{A.20}$$

where j is the unit imaginary number and ω is the frequency. From substitution of Eq. (A.20) into Eq. (A.19) an equation can be found for the frequency as approximated with the second-order central difference scheme $\hat{\omega}$:

$$\hat{\omega} = u\frac{\sin\left(k\mathrm{d}x\right)}{\mathrm{d}x}. \tag{A.21}$$

The phase velocity $\hat{u}$ can now be written as

$$\hat{u} = \frac{\hat{\omega}}{k} = u\frac{\sin\left(k\mathrm{d}x\right)}{k\mathrm{d}x}. \tag{A.22}$$

This analysis demonstrates that for the second-order central scheme, the phase velocity is a function of the wavenumber k. For large wavelengths, k is small and $\hat{u} \approx u$. However, for the shortest possible wavelength, $k = \pi/\mathrm{d}x$, Eq. (A.22) shows that $\hat{u} = 0$. For a more comprehensive discussion, the reader is referred to Durran (2010, chapter 3.3).

A.5 Upwind-biased Advection Schemes

Hundsdorfer et al. (1995) described how upwind-biased advection schemes of order $r-1$ can be devised starting from a rth-order central schemes by adding a dissipation term. This spurious dissipation is actually advantageous, as it is strongest for the short wavelengths that have the largest dispersive errors. The over- and undershoots of the central scheme should therefore be smaller in the upwind-biased scheme. DALES contains a fifth-order upwind scheme that can be written as (Wicker and Skamarock, 2002):

$$\hat{f}^{5\text{th}}_{i+\frac{1}{2}} = \hat{f}^{6\text{th}}_{i+\frac{1}{2}} - \frac{|u_{i+\frac{1}{2}}|}{60}[10(\varphi_{i+1}-\varphi_i) - 5(\varphi_{i+2}-\varphi_{i-1}) + \varphi_{i+3} - \varphi_{i-2}]. \tag{A.23}$$

By taking the absolute value of the horizontal velocity, the scheme is ensured to be upwind biased. If $u_{i+\frac{1}{2}} > 0$, Eq. (A.23) becomes:

$$\hat{f}^{5\text{th}}_{i+\frac{1}{2}} = \frac{u_{i+\frac{1}{2}}}{60}\left(27\varphi_{i+1} + 47\varphi_i - 3\varphi_{i+2} - 13\varphi_{i-1} + 2\varphi_{i-2}\right), \tag{A.24}$$

from which it is clear that the stencil of this scheme consists of five consecutive grid points. Results obtained with this fifth-order upwind scheme for the idealized test case of the advection of a step function are shown in Figure A.3. The over- and undershoots are still clearly present behind the discontinuity, but their magnitudes are slightly smaller than for the sixth-order centered scheme.

For the typical LES of cumulus-topped boundary layers or deep convective cases, the fifth-order or even the second-order advection schemes often perform sufficiently well as there are typically no sharp vertical gradients in the slab-averaged profiles. However, upon inspection of instantaneous cross sections oscillations can often be easily found.

Stratocumulus clouds typically form under a strong temperature inversion. This inversion is marked by an increase of the liquid water potential temperature θ_l of up to 15 K over a vertical distance of 50 m, while q_t can decrease by as much as 80 % (Stevens et al., 2005b). The vertical structure of stratocumulus-topped boundary layers therefore resembles the example in Figure A.3. Under such conditions, the oscillatory character of the advection schemes discussed above can become problematic (Bretherton et al., 1999b).

To demonstrate this, the CGILS S12 stratocumulus case has been simulated using DALES. The specifics for this case are described by Blossey et al. (2013). Figure A.4a shows the slab-averaged profile of q_t for the 24th hour of the simulation. The cell-centered values obtained using the fifth-order upwind scheme are indicated by the black dots. The unphysical undershoot that is the result of use of the fifth-order advection scheme is clearly visible in these slab-averaged results.

A.6 Essentially Non-oscillatory Method

One method to avoid oscillatory behavior is to adaptively choose the stencil S_l that is used for the approximation of $\varphi_{i+\frac{1}{2}}$ in order to avoid the use of stencils

Table A.1. The values of the coefficients a_k^l (Jiang and Shu, 1996).

a_k^l	$l=0$	$l=1$	$l=2$
$k=0$	2/6	-7/6	11/6
$k=1$	-1/6	5/6	2/6
$k=2$	2/6	5/6	-1/6

that contain a discontinuity. This is the basic concept behind the essentially non-oscillatory (ENO) method (Harten et al., 1987; Shu and Osher, 1988, 1989).

Consider the schematic in Figure A.2 in which the flow is from left to right. For the third-order scheme depicted in this schematic, there are three candidate stencils defined by the left shifts $l \in \{0,1,2\}$. According to Eq. (A.10), the approximations for these stencils $\hat{\varphi}^l_{i+\frac{1}{2}}$ can be written as:

$$\hat{\varphi}^0_{i+\frac{1}{2}} = a^0_0\varphi_{i-2} + a^0_1\varphi_{i-1} + a^0_2\varphi_i; \tag{A.25a}$$

$$\hat{\varphi}^1_{i+\frac{1}{2}} = a^1_0\varphi_{i-1} + a^1_1\varphi_i \quad + a^1_2\varphi_{i+1}; \tag{A.25b}$$

$$\hat{\varphi}^2_{i+\frac{1}{2}} = a^2_0\varphi_i \quad + a^2_1\varphi_{i+1} + a^2_2\varphi_{i+2}. \tag{A.25c}$$

The values of the coefficients a_k^l are given in Table A.1. Similar equations for flow in the opposite direction can be obtained by mirroring the problem in the point $x_{i+\frac{1}{2}}$. For the remainder of this appendix, flow from left to right is assumed.

Suppose that the step in φ between x_{i-1} and x_i is relatively large. Stencil S_0 should in that case be used for the approximation of $\varphi_{i+\frac{1}{2}}$, as stencils S_1 and S_2 contain the discontinuity. To determine which of the stencils is smoothest and will therefore result in the most accurate approximation of $\varphi_{i+\frac{1}{2}}$, a smoothness indicator can be defined for each stencil.

In general, the maximum order of accuracy that can be obtained using a stencil consisting of r grid points is r. The sixth- and fifth-order schemes in Eqs. (A.15) and (A.24) are therefore of optimal order. Equations (A.25) show that the values of a total of five grid points are considered to give a third-order accurate ENO scheme. ENO schemes are therefore rather inefficient in terms of the order of convergence that is achieved.

A.7 Weighted ENO Method

Liu et al. (1994) noted that when all stencils are equally smooth, they should all contribute to the interpolated value $\varphi_{i+\frac{1}{2}}$, yielding an interpolation scheme of order $(r+1)$ given an r-th order ENO scheme. This can be achieved by assigning a normalized weight ω_l to the approximation $\hat{\varphi}_{i+\frac{1}{2}}$ obtained from a stencil S_l. The weight assigned to a stencil is large if the stencil is relatively smooth. The approximation of $\varphi_{i+\frac{1}{2}}$ then becomes

$$\hat{\varphi}_{i+\frac{1}{2}} = \sum_{l=0}^{r-1} \omega_l \hat{\varphi}^l_{i+\frac{1}{2}}, \tag{A.26}$$

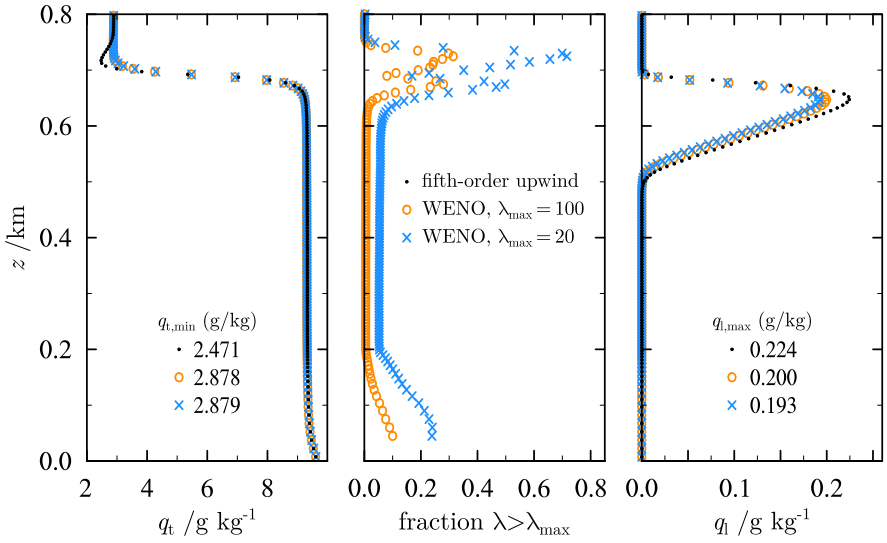

Figure A.4. Profiles of (a) total water specific humidity q_t, (b) the fraction of top/bottom grid faces at which $\lambda > \lambda_{max}$ and (c) the liquid water specific humidity q_l. The profiles have been averaged over the 24th hour of the CGILS S12 stratocumulus case. Microphysical processes were disabled for these simulations. Results obtained using the fifth-order advection scheme for scalars are indicated by black dots. The orange circles and blue crosses show the results of the hybrid advection scheme using $\lambda_{max} = 100$ and 20, respectively.

where:

$$\omega_l = \frac{\alpha_l}{\sum_l \alpha_l}. \tag{A.27}$$

This is the basic principle of weighted ENO (WENO) schemes. The weights α_l in Eq. (A.27) are derived from a smoothness metric β_l as follows:

$$\alpha_l = \frac{C_l}{(\epsilon + \beta_l)^p}, \tag{A.28}$$

in which $\epsilon = 10^{-12}$ is a small constant that bounds the value of α_l and p is a constant power that typically has a value of 1 or 2.

Jiang and Shu (1996) found that by carefully choosing the coefficients C_l and the smoothness metric β_l, WENO schemes of optimal order can be derived. In other words, a WENO scheme of order $r+2$ can be derived given a rth-order ENO scheme. As part of this thesis project, the fifth-order accurate WENO scheme of Jiang and Shu (1996) has been implemented in DALES. This scheme uses the ENO stencils described by Eq. (A.25) and Table A.1. The smoothness of each of these

Table A.2. The weights C_l used in the fifth-order WENO scheme.

	$l=0$	$l=1$	$l=2$
C_l	1/10	6/10	3/10

stencils is calculated as:

$$\begin{aligned}
\beta_0 &= \frac{13}{12}(\varphi_{i-2} - 2\varphi_{i-1} + \varphi_i \quad)^2 + \frac{1}{4}(\varphi_{i-2} - 4\varphi_{i-1} + 3\varphi_i \;)^2; \\
\beta_1 &= \frac{13}{12}(\varphi_{i-1} - 2\varphi_i \quad + \varphi_{i+1})^2 + \frac{1}{4}(\varphi_{i-1} \qquad\quad - \varphi_{i+1})^2; \\
\beta_2 &= \frac{13}{12}(\varphi_i \quad - 2\varphi_{i+1} + \varphi_{i+2})^2 + \frac{1}{4}(3\varphi_i \;- 4\varphi_{i+1} + \varphi_{i+2})^2.
\end{aligned} \tag{A.29}$$

The weights C_l are given in Table A.2. Recall that flow from left to right is assumed and that equations for flow in the opposite direction can be obtained by mirroring in $x_{i+\frac{1}{2}}$.

From Eqs. (A.27) and (A.28) it can be seen that when all stencils are equally smooth, i.e. $\beta_l = \beta$ for all l,

$$\hat{\varphi}_{i+\frac{1}{2}} = \sum_{l=0}^{r-1} C_l \hat{\varphi}^l_{i+\frac{1}{2}}, \tag{A.30}$$

given that

$$\sum_l C_l = 1. \tag{A.31}$$

From substitution of Eqs. (A.25) into Eq. (A.30), the fifth-order upwind scheme of Eq. (A.24) is obtained. This shows that the fifth-order WENO scheme and the fifth-order upwind scheme are equivalent for the advection of completely smooth fields.

The WENO scheme performs very well for the one-dimensional advection of a step function, as is evident from Figure A.3. Spurious over- and undershoots are almost completely avoided and the propagation speed of the discontinuity is well captured. It is important to keep in mind that although WENO schemes are in general very capable of avoiding oscillatory behavior, they are not strictly monotonic.

A.8 Hybrid Methodology

Despite their generally good performance in many idealized test cases, WENO advection schemes are not very suitable for use in LES models. Typically, scalars fields in an LES strongly fluctuate and are far from smooth. WENO schemes are therefore often quite dissipative in practice. Hill and Pullin (2004) therefore proposed to use the WENO method only at those cell interfaces where a smoothness metric λ exceeds a critical value $\lambda_{\max}$:

$$\lambda_{i+\frac{1}{2}} = \frac{\max_l \beta_l}{\min_l \beta_l + \epsilon_\beta} > \lambda_{\max}. \tag{A.32}$$

Table A.3. The values of the characteristic variation in the field of a scalar φ. These values are hard-coded in DALES.

φ	$\delta\varphi$	units
q_t	10^{-3}	$\mathrm{kg\,kg^{-1}}$
θ_l	1	K
q_r	10^{-6}	$\mathrm{kg\,kg^{-1}}$
N_r	10^{3}	
e''	10^{-1}	$\mathrm{m^2\,s^{-2}}$

Here, $\epsilon_\beta = 10^{-4}$ is a small regularization parameter. Furthermore, $\max_l \beta_l$ and $\min_l \beta_l$ denote the maximum and minimum value from the set of values of β_l, respectively.

Blossey and Durran (2008) propose a similar, but less computationally demanding criterion that can be formulated as:

$$\lambda_{i+\frac{1}{2}} = \frac{\max_{k\in K} \gamma_k}{\min_{k\in K} \gamma_k + \epsilon_\gamma} > \lambda_\mathrm{max}. \tag{A.33}$$

In this equation

$$\gamma_i = (\varphi_{i+1} - \varphi_i)^2 + (\varphi_i - \varphi_{i-1})^2 \tag{A.34}$$

and the values of k depend on the direction of the flow:

$$K = \begin{cases} [i-1, i, i+1], & \text{if } u_{i+\frac{1}{2}} \geqslant 0, \\ [i, i+1, i+2], & \text{otherwise.} \end{cases} \tag{A.35}$$

In Eq. (A.33), ϵ_γ represents the magnitude of the jumps of φ that are worthy of attention. It is calculated as (Peter Blossey, personal communication 2011)

$$\epsilon_\gamma = 10^{-8} \left(\delta\varphi\right)^2, \tag{A.36}$$

in which $\delta\varphi$ is the characteristic scale of spatial variations of φ. The numerical values of $\delta\varphi$ that are hard-coded in DALES are given in Table A.3 for the relevant prognostic variables.

If the criterion in Eq. (A.33) is met, the WENO scheme defined by Eqs. (A.25)-(A.29) is used. If $\lambda < \lambda_\mathrm{max}$ all stencils are assumed equally smooth, such that the fifth-order upwind scheme can be used. The threshold λ_max can be varied, but has a default value $\lambda_\mathrm{max} = 20$ (Blossey and Durran, 2008).

A

A.9 Large-Eddy Simulation Results

To evaluate the performance of the hybrid scheme for the advection of scalars and the influence of the value of λ_max on the results, the CGILS S12 stratocumulus case (Blossey et al., 2013) has been run with DALES. The simulations have been run for 24 h and the slab-averaged total specific humidity, q_t, averaged over the last hour is shown in Figure A.4a. The black dots show the cell-center values obtained with the fifth-order upwind scheme as a reference. Orange circles and blue crosses

indicate the results obtained with the hybrid scheme, using a value of $\lambda_{\max} = 100$ and 20, respectively. The results for these simulations are practically identical and there is no sign of a spurious minimum.

Figure A.4b shows the fraction of grid faces at which the critical value $\lambda_{\max}$ is exceeded. Here, only the vertical direction is taken into account. The fraction is small in the boundary layer and peaks in the inversion layer. The WENO scheme is therefore mainly active in the vicinity of the inversion and the results in the bulk of the boundary layer can be expected to be similar to the results obtained with the fifth-order scheme. The peak fraction depends significantly on $\lambda_{\max}$, with fractions up to 0.7 for $\lambda_{\max} = 20$ and 0.3 for $\lambda_{\max} = 100$.

Figure A.4c shows the slab-average liquid water specific humidity q_l for the three simulations. The fifth-order scheme gives a maximum q_l-value that is approximately 10 % greater than for the simulations with the hybrid scheme. The difference between the $\lambda_{\max} = 20$ and $\lambda_{\max} = 100$ simulations is rather insignificant.

These results illustrate that the hybrid-WENO advection scheme that has been implemented in DALES is suitable for simulations of stratocumulus-topped boundary layers under strong inversions. The scheme can be used for all scalars present in DALES in combination with the fifth-order upwind scheme for the velocity components u, v and w. The value of $\lambda_{\max}$ has limited impact on the simulation results, such that any value that is roughly between 20 and 100 can be used. The higher $\lambda_{\max}$, the more the results will resemble those obtained with the fifth-order advection scheme.

Abel, S. J. and B. J. Shipway, 2007: A comparison of cloud-resolving model simulations of trade wind cumulus with aircraft observations taken during RICO. *Q.J.R. Meteorol. Soc.*, **133 (624)**, 781–794.

Ackerman, A. S., M. P. Kirkpatrick, D. E. Stevens, and O. B. Toon, 2004: The impact of humidity above stratiform clouds on indirect aerosol climate forcing. *Nature*, **432 (7020)**, 1014–1017.

Ackerman, A. S., et al., 2009: Large-eddy simulations of a drizzling, stratocumulus-topped marine boundary layer. *Mon. Wea. Rev.*, **137 (3)**, 1083–1110.

Albrecht, B. A., C. S. Bretherton, D. Johnson, W. H. Scubert, and A. S. Frisch, 1995: The Atlantic stratocumulus transition experiment–ASTEX. *Bull. Amer. Meteor. Soc.*, **76 (6)**, 889–904.

Arakawa, A., 1975: *Modelling clouds and cloud processes for use in climate models.* WMO The Physical Basis of Climate and Climate modelling.

Arakawa, A. and V. R. Lamb, 1977: Computational design of the basic dynamical processes of the UCLA general circulation model. *Methods in computational physics*, **17**, 173–265.

Bellon, G. and B. Stevens, 2012: Time scales of the trade wind boundary layer adjustment. *J. Atmos. Sci.*, **70 (4)**, 1071–1083.

Blossey, P. N., C. S. Bretherton, A. Cheng, J. J. van der Dussen, S. Endo, T. Heus, and A. Lock, 2015: Marine low cloud sensitivity to increased CO_2 and a CMIP3 composite climate perturbations: Phase 2 of the CGILS LES intercomparison. *In preparation for the J. Adv. Model. Earth Syst.*

Blossey, P. N. and D. R. Durran, 2008: Selective monotonicity preservation in scalar advection. *J. Comput. Phys.*, **227 (10)**, 5160–5183.

Blossey, P. N., et al., 2013: Marine low cloud sensitivity to an idealized climate change: The CGILS LES intercomparison. *J. Adv. Model. Earth Syst.*, **5 (2)**, 234–258.

Böing, S., 2014: The interaction between deep convective clouds and their environment. Ph.D. thesis, Delft University of Technology.

Böing, S. J., H. J. J. Jonker, A. P. Siebesma, and W. W. Grabowski, 2012: Influence of the subcloud layer on the development of a deep convective ensemble. *J. Atmos. Sci.*, **69 (9)**, 2682–2698.

Bony, S. and J.-L. Dufresne, 2005: Marine boundary layer clouds at the heart of tropical cloud feedback uncertainties in climate models. *Geophys. Res. Lett.*, **32 (20)**, L20 806–.

Bougeault, P., 1985: The diurnal cycle of the marine stratocumulus layer: A higher-order model study. *J. Atmos. Sci.*, **42 (24)**, 2826–2843.

Bretherton, C. S., P. Austin, and S. T. Siems, 1995: Cloudiness and marine boundary layer dynamics in the ASTEX lagrangian experiments. Part II: Cloudiness, drizzle, surface fluxes, and entrainment. *J. Atmos. Sci.*, **52 (16)**, 2724–2735.

Bretherton, C. S. and P. N. Blossey, 2014: Low cloud reduction in a greenhouse-warmed climate: Results from Lagrangian LES of a subtropical marine cloudiness transition. *J. Adv. Model. Earth Syst.*, **6 (1)**, 91–114.

Bretherton, C. S., P. N. Blossey, and C. R. Jones, 2013: Mechanisms of marine low cloud sensitivity to idealized climate perturbations: A single-LES exploration extending the CGILS cases. *J. Adv. Model. Earth Syst.*

Bretherton, C. S., P. N. Blossey, and J. Uchida, 2007: Cloud droplet sedimentation, entrainment efficiency, and subtropical stratocumulus albedo. *Geophys. Res. Lett.*, **34 (3)**, L03 813–.

Bretherton, C. S., S. K. Krueger, M. C. Wyant, P. Bechtold, E. Van Meijgaard, B. Stevens, and J. Teixeira, 1999a: A GCSS boundary-layer cloud model intercomparison study of the first ASTEX Lagrangian experiment. *Bound.-Layer Meteor.*, **93 (3)**, 341–380.

Bretherton, C. S. and R. Pincus, 1995: Cloudiness and marine boundary layer dynamics in the ASTEX lagrangian experiments. Part I: Synoptic setting and vertical structure. *J. Atmos. Sci.*, **52 (16)**, 2707–2723.

Bretherton, C. S., J. Uchida, and P. N. Blossey, 2010: Slow manifolds and multiple equilibria in stratocumulus-capped boundary layers. *J. Adv. Model. Earth Syst.*, **2**, 20.

Bretherton, C. S. and M. C. Wyant, 1997: Moisture transport, lower-tropospheric stability, and decoupling of cloud-topped boundary layers. *J. Atmos. Sci.*, **54 (1)**, 148–167.

Bretherton, C. S., et al., 1999b: An intercomparison of radiatively driven entrainment and turbulence in a smoke cloud, as simulated by different numerical models. *Q.J.R. Meteorol. Soc.*, **125 (554)**, 391–423.

Bretherton, C. S., et al., 2004: The EPIC 2001 stratocumulus study. *Bull. Amer. Meteor. Soc.*, **85 (7)**, 967–977.

Briegleb, B. P., 1992: Delta-Eddington approximation for solar radiation in the NCAR community climate model. *J. Geophys. Res.*, **97 (D7)**, 7603–7612.

Caldwell, P. and C. S. Bretherton, 2009: Large eddy simulation of the diurnal cycle in southeast pacific stratocumulus. *J. Atmos. Sci.*, **66 (2)**, 432–449.

Caldwell, P., C. S. Bretherton, and R. Wood, 2005: Mixed-layer budget analysis of the diurnal cycle of entrainment in southeast pacific stratocumulus. *J. Atmos. Sci.*, **62 (10)**, 3775–3791.

Caldwell, P. M., Y. Zhang, and S. A. Klein, 2012: CMIP3 subtropical stratocumulus cloud feedback interpreted through a mixed-layer model. *J. Climate*, **26 (5)**, 1607–1625.

Carman, J. K., D. L. Rossiter, D. Khelif, H. H. Jonsson, I. C. Faloona, and P. Y. Chuang, 2012: Observational constraints on entrainment and the entrainment interface layer in stratocumulus. *Atmos. Chem. Phys.*, **12 (22)**, 11 135–11 152.

Cess, R. D., et al., 1989: Interpretation of cloud-climate feedback as produced by 14 atmospheric general circulation models. *Science*, **245 (4917)**, 513–516.

Cess, R. D., et al., 1990: Intercomparison and interpretation of climate feedback processes in 19 atmospheric general circulation models. *J. Geophys. Res.*, **95 (D10)**, 16 601–16 615.

Chen, C. and W. R. Cotton, 1987: The physics of the marine stratocumulus-capped mixed layer. *J. Atmos. Sci.*, **44 (20)**, 2951–2977.

Chlond, A. and A. Wolkau, 2000: Large-eddy simulation of a nocturnal stratocumulus-topped marine atmospheric boundary layer: An uncertainty analysis. *Bound.-Layer Meteor.*, **95 (1)**, 31–55–.

Christensen, M. W., G. G. Carrió, G. L. Stephens, and W. R. Cotton, 2013: Radiative impacts of free-tropospheric clouds on the properties of marine stratocumulus. *J. Atmos. Sci.*, **70 (10)**, 3102–3118.

Chung, D., G. Matheou, and J. Teixeira, 2012: Steady-state large-eddy simulations to study the stratocumulus to shallow cumulus cloud transition. *J. Atmos. Sci.*, **69 (11)**, 3264–3276.

Ciesielski, P. E., W. H. Schubert, and R. H. Johnson, 1999: Large-scale heat and moisture budgets over the ASTEX region. *J. Atmos. Sci.*, **56 (18)**, 3241–3261.

Ciesielski, P. E., W. H. Schubert, and R. H. Johnson, 2001: Diurnal variability of the marine boundary layer during ASTEX. *J. Atmos. Sci.*, **58 (16)**, 2355–2376.

Comstock, K. K., R. Wood, S. E. Yuter, and C. S. Bretherton, 2004: Reflectivity and rain rate in and below drizzling stratocumulus. *Q.J.R. Meteorol. Soc.*, **130 (603)**, 2891–2918.

Dal Gesso, S., A. P. Siebesma, and S. R. de Roode, 2014a: Evaluation of low-cloud climate feedback through single-column model equilibrium states. *Q.J.R. Meteorol. Soc.*

Dal Gesso, S., A. P. Siebesma, S. R. de Roode, and J. M. van Wessem, 2014b: A mixed-layer model perspective on stratocumulus steady states in a perturbed climate. *Q.J.R. Meteorol. Soc.*

Dal Gesso, S., J. J. van der Dussen, A. P. Siebesma, S. R. de Roode, I. A. Boutle, Y. Kamae, R. Roehrig, and J. Vial, 2015: A single-column model intercomparison on the stratocumulus representation in present-day and future climate. *J. Adv. Model. Earth Syst.*, n/a–n/a.

De Roode, S. R. and P. G. Duynkerke, 1996: Dynamics of cumulus rising into stratocumulus as observed during the first Lagrangian experiment of ASTEX. *Q.J.R. Meteorol. Soc.*, **122 (535)**, 1597–1623.

De Roode, S. R. and P. G. Duynkerke, 1997: Observed Lagrangian transition of stratocumulus into cumulus during ASTEX: Mean state and turbulence structure. *J. Atmos. Sci.*, **54 (17)**, 2157–2173.

De Roode, S. R., P. G. Duynkerke, and H. J. J. Jonker, 2004: Large-eddy simulation: How large is large enough? *J. Atmos. Sci.*, **61 (4)**, 403–421.

De Roode, S. R., I. Sandu, J. J. van der Dussen, A. S. Ackerman, P. N. Blossey, A. Lock, A. P. Siebesma, and B. Stevens, 2012: LES results of the EUCLIPSE Lagrangian stratocumulus to shallow cumulus transition cases. *Paper presented at 20th Symposium on Boundary Layers and Turbulence*, Boston, Mass.

De Roode, S. R., A. P. Siebesma, S. D. Gesso, H. J. J. Jonker, J. Schalkwijk, and J. Sival, 2014: A mixed-layer model study of the stratocumulus response to changes in large-scale conditions. *J. Adv. Model. Earth Syst.*, **6 (4)**, 1256–1270.

De Roode, S. R. and J. J. Van der Dussen, 2010: Large-eddy simulation of a stratocumulus to cumulus cloud transition as observed during ASTEX. *Paper presented at 19th Symposium on Boundary Layers and Turbulence*, Keystone, Colo.

Deardorff, J. W., 1972: Numerical investigation of neutral and unstable planetary boundary layers. *J. Atmos. Sci.*, **29 (1)**, 91–115.

Deardorff, J. W., 1980a: Cloud top entrainment instability. *J. Atmos. Sci.*, **37 (1)**, 131–147.

Deardorff, J. W., 1980b: Stratocumulus-capped mixed layers derived from a three-dimensional model. *Bound.-Layer Meteor.*, **18 (4)**, 495–527.

Durran, D. R., 2010: *Numerical Methods for Fluid Dynamics with Applications to Geophysics*. 2d ed., Springer New York.

Duynkerke, P. G., 1993: The stability of cloud top with regard to entrainment: Amendment of the theory of cloud-top entrainment instability. *J. Atmos. Sci.*, **50 (3)**, 495–502.

Duynkerke, P. G. and P. Hignett, 1993: Simulation of diurnal variation in a stratocumulus-capped marine boundary layer during FIRE. *Mon. Wea. Rev.*, **121 (12)**, 3291–3300.

Duynkerke, P. G., et al., 1999: Intercomparison of three- and one-dimensional model simulations and aircraft observations of stratocumulus. *Bound.-Layer Meteor.*, **92 (3)**, 453–487.

Edwards, J. M. and A. Slingo, 1996: Studies with a flexible new radiation code. I: Choosing a configuration for a large-scale model. *Q.J.R. Meteorol. Soc.*, **122 (531)**, 689–719.

Emanuel, K. A., 1994: *Atmospheric convection*. Oxford University Press.

Faloona, I., et al., 2005: Observations of entrainment in eastern pacific marine stratocumulus using three conserved scalars. *J. Atmos. Sci.*, **62 (9)**, 3268–3285.

Fu, Q. and K. N. Liou, 1993: Parameterization of the radiative properties of cirrus clouds. *J. Atmos. Sci.*, **50 (13)**, 2008–2025.

Geoffroy, O., J.-L. Brenguier, and I. Sandu, 2008: Relationship between drizzle rate, liquid water path and droplet concentration at the scale of a stratocumulus cloud system. *Atmos. Chem. Phys.*, **8 (16)**, 4641–4654.

Ghonima, M. S., J. R. Norris, T. Heus, and J. Kleissl, 2015: Reconciling and validating the cloud thickness and liquid water path tendencies proposed by R. Wood and J. J. van der Dussen et al. *J. Atmos. Sci.*, **72 (5)**, 2033–2040.

Harten, A., B. Engquist, S. Osher, and S. R. Chakravarthy, 1987: Uniformly high order accurate essentially non-oscillatory schemes, III. *Journal of Computational Physics*, **71 (2)**, 231–303.

Hazeleger, W., et al., 2010: EC-Earth: A seamless Earth-system prediction approach in action. *Bull. Amer. Meteor. Soc.*, **91 (10)**, 1357–1363.

Held, I. M. and B. J. Soden, 2000: Water vapor feedback and global warming. *Annu. Rev. Energy Environ.*, **25 (1)**, 441–475.

Held, I. M. and B. J. Soden, 2006: Robust responses of the hydrological cycle to global warming. *J. Climate*, **19 (21)**, 5686–5699.

Heus, T., et al., 2010: Formulation of the Dutch Atmospheric Large-Eddy Simulation (DALES) and overview of its applications. *Geosci. Model Dev.*, **3 (2)**, 415–444.

Hill, D. J. and D. I. Pullin, 2004: Hybrid tuned center-difference-WENO method for large eddy simulations in the presence of strong shocks. *J. Comput. Phys.*, **194 (2)**, 435–450.

Hundsdorfer, W., B. Koren, M. vanLoon, and J. Verwer, 1995: A positive finite-difference advection scheme. *Journal of Computational Physics*, **117 (1)**, 35–46.

Iacono, M. J., J. S. Delamere, E. J. Mlawer, M. W. Shephard, S. A. Clough, and

W. D. Collins, 2008: Radiative forcing by long-lived greenhouse gases: Calculations with the AER radiative transfer models. *J. Geophys. Res.*, **113 (D13)**, D13 103–.

Jiang, G.-S. and C.-W. Shu, 1996: Efficient implementation of weighted ENO schemes. *J. Comput. Phys.*, **126 (1)**, 202–228.

Jones, C. R., C. S. Bretherton, and P. N. Blossey, 2014: Fast stratocumulus time scale in mixed layer model and large eddy simulation. *J. Adv. Model. Earth Syst.*, **6 (1)**, 206–222.

Juang, H.-M. H. and S.-Y. Hong, 2009: Forward semi-Lagrangian advection with mass conservation and positive definiteness for falling hydrometeors. *Mon. Wea. Rev.*, **138 (5)**, 1778–1791.

Khairoutdinov, M. and Y. Kogan, 2000: A new cloud physics parameterization in a large-eddy simulation model of marine stratocumulus. *Mon. Wea. Rev.*, **128 (1)**, 229–243.

Khairoutdinov, M. F. and D. A. Randall, 2003: Cloud resolving modeling of the ARM summer 1997 IOP: Model formulation, results, uncertainties, and sensitivities. *J. Atmos. Sci.*, **60 (4)**, 607–625.

Klein, S. A. and D. L. Hartmann, 1993: The seasonal cycle of low stratiform clouds. *J. Climate*, **6 (8)**, 1587–1606.

Kogan, Y., 2013: A cumulus cloud microphysics parameterization for cloud-resolving models. *J. Atmos. Sci.*, **70 (5)**, 1423–1436.

Krueger, S. K., G. T. McLean, and Q. Fu, 1995: Numerical simulation of the stratus-to-cumulus transition in the subtropical marine boundary layer. Part I: Boundary-layer structure. *J. Atmos. Sci.*, **52 (16)**, 2839–2850.

Kuo, H.-C. and W. H. Schubert, 1988: Stability of cloud-topped boundary layers. *Q.J.R. Meteorol. Soc.*, **114 (482)**, 887–916.

Lenschow, D. H., et al., 1988: Dynamics and chemistry of marine stratocumulus (DYCOMS) experiment. *Bull. Amer. Meteor. Soc.*, **69 (9)**, 1058–1067.

Lewellen, D. C. and W. S. Lewellen, 1998: Large-eddy boundary layer entrainment. *J. Atmos. Sci.*, **55 (16)**, 2645–2665.

Lilly, D. K., 1962: On the numerical simulation of buoyant convection. *Tellus*, **14 (2)**, 148–172.

Lilly, D. K., 1968: Models of cloud-topped mixed layers under a strong inversion. *Q.J.R. Meteorol. Soc.*, **94 (401)**, 292–309.

Lilly, D. K., 2002: Entrainment into mixed layers. Part II: A new closure. *J. Atmos. Sci.*, **59 (23)**, 3353–3361.

Liu, X.-D., S. Osher, and T. Chan, 1994: Weighted essentially non-oscillatory schemes. *Journal of Computational Physics*, **115 (1)**, 200–212.

Lock, A. P., 1998: The parametrization of entrainment in cloudy boundary layers. *Q.J.R. Meteorol. Soc.*, **124 (552)**, 2729–2753.

Lock, A. P., 2009: Factors influencing cloud area at the capping inversion for shallow cumulus clouds. *Q.J.R. Meteorol. Soc.*, **135 (641)**, 941–952.

MacVean, M. K. and P. J. Mason, 1990: Cloud-top entrainment instability through small-scale mixing and its parameterization in numerical models. *J. Atmos. Sci.*, **47 (8)**, 1012–1030.

Malinowski, S. P., et al., 2013: Physics of stratocumulus top (POST): turbulent mixing across capping inversion. *Atmos. Chem. Phys. Discuss.*, **13 (6)**, 15 233–

15 269.

Martin, G. M., D. W. Johnson, D. P. Rogers, P. R. Jonas, P. Minnis, and D. A. Hegg, 1995: Observations of the interaction between cumulus clouds and warm stratocumulus clouds in the marine boundary layer during ASTEX. *J. Atmos. Sci.*, **52 (16)**, 2902–2922.

Medeiros, B., B. Stevens, and S. Bony, 2014: Using aquaplanets to understand the robust responses of comprehensive climate models to forcing. *Climate Dyn.*, 1–21–.

Mellado, J. P., B. Stevens, and H. Schmidt, 2013: Wind shear and buoyancy reversal at the top of stratocumulus. *J. Atmos. Sci.*, **71 (3)**, 1040–1057.

Mellado, J. P., B. Stevens, H. Schmidt, and N. Peters, 2009: Buoyancy reversal in cloud-top mixing layers. *Q.J.R. Meteorol. Soc.*, **135 (641)**, 963–978.

Mlawer, E. J., S. J. Taubman, P. D. Brown, M. J. Iacono, and S. A. Clough, 1997: Radiative transfer for inhomogeneous atmospheres: RRTM, a validated correlated-k model for the longwave. *J. Geophys. Res.*, **102 (D14)**, 16 663–16 682.

Moeng, C.-H., 2000: Entrainment rate, cloud fraction, and liquid water path of PBL stratocumulus clouds. *J. Atmos. Sci.*, **57 (21)**, 3627–3643.

Moeng, C.-H. and R. Rotunno, 1990: Vertical-velocity skewness in the buoyancy-driven boundary layer. *J. Atmos. Sci.*, **47 (9)**, 1149–1162.

Morrison, H., J. A. Curry, and V. I. Khvorostyanov, 2005: A new double-moment microphysics parameterization for application in cloud and climate models. Part I: Description. *J. Atmos. Sci.*, **62 (6)**, 1665–1677.

Myers, T. A. and J. R. Norris, 2013: Observational evidence that enhanced subsidence reduces subtropical marine boundary layer cloudiness. *J. Climate*, **26 (19)**, 7507–7524.

Nam, C., S. Bony, J.-L. Dufresne, and H. Chepfer, 2012: The 'too few, too bright' tropical low-cloud problem in CMIP5 models. *Geophys. Res. Lett.*, **39 (21)**, L21 801–.

Nicholls, S., 1984: The dynamics of stratocumulus: Aircraft observations and comparisons with a mixed layer model. *Q.J.R. Meteorol. Soc.*, **110 (466)**, 783–820.

Nicholls, S., 1989: The structure of radiatively driven convection in stratocumulus. *Q.J.R. Meteorol. Soc.*, **115 (487)**, 487–511.

Nicholls, S. and J. Leighton, 1986: An observational study of the structure of stratiform cloud sheets: Part I. Structure. *Q.J.R. Meteorol. Soc.*, **112 (472)**, 431–460.

Nicholls, S. and J. D. Turton, 1986: An observational study of the structure of stratiform cloud sheets: Part II. Entrainment. *Q.J.R. Meteorol. Soc.*, **112 (472)**, 461–480.

Noda, A. T., K. Nakamura, T. Iwasaki, and M. Satoh, 2013: A numerical study of a stratocumulus-topped boundary-layer: Relations of decaying clouds with a stability parameter across inversion. *Journal of the Meteorological Society of Japan. Ser. II*, **91 (6)**, 727–746.

Nuijens, L. and B. Stevens, 2011: The influence of wind speed on shallow marine cumulus convection. *J. Atmos. Sci.*, **69 (1)**, 168–184.

Paltridge, G. W., 1980: Cloud-radiation feedback to climate. *Q.J.R. Meteorol. Soc.*, **106 (450)**, 895–899.

Park, S., C. B. Leovy, and M. A. Rozendaal, 2004: A new heuristic Lagrangian marine boundary layer cloud model. *J. Atmos. Sci.*, **61 (24)**, 3002–3024.

Pawlowska, H. and J.-L. Brenguier, 2000: Microphysical properties of stratocumulus clouds during ACE-2. *Tellus B*, **52 (2)**, 868–887.

Pincus, R. and B. Stevens, 2009: Monte Carlo spectral integration: a consistent approximation for radiative transfer in large eddy simulations. *J. Adv. Model. Earth Syst.*, **1**, 9.

Pope, S. B., 2000: *Turbulent flows*. Cambridge University Press.

Prusa, J. M., P. K. Smolarkiewicz, and A. A. Wyszogrodzki, 2008: EULAG, a computational model for multiscale flows. *Comput. Fluids*, **37 (9)**, 1193–1207.

Ramanathan, V., R. D. Cess, E. F. Harrison, P. Minnis, B. R. Barkstrom, E. Ahmad, and D. Hartmann, 1989: Cloud-radiative forcing and climate: Results from the Earth radiation budget experiment. *Science*, **243 (4887)**, 57–63.

Randall, D. A., 1980: Conditional instability of the first kind upside-down. *J. Atmos. Sci.*, **37 (1)**, 125–130.

Randall, D. A., 1984: Stratocumulus cloud deepening through entrainment. *Tellus A*, **36A (5)**, 446–457.

Randall, D. A., J. A. Coakley, D. H. Lenschow, C. W. Fairall, and R. A. Kropfli, 1984: Outlook for research on subtropical marine stratification clouds. *Bull. Amer. Meteor. Soc.*, **65 (12)**, 1290–1301.

Randall, D. A., et al., 2003: Confronting models with data: The GEWEX cloud systems study. *Bull. Amer. Meteor. Soc.*, **84 (4)**, 455–469.

Renfrew, I. A., G. W. K. Moore, P. S. Guest, and K. Bumke, 2002: A comparison of surface layer and surface turbulent flux observations over the Labrador sea with ECMWF analyses and NCEP reanalyses. *J. Phys. Oceanogr.*, **32 (2)**, 383–400.

Rieck, M., L. Nuijens, and B. Stevens, 2012: Marine boundary layer cloud feedbacks in a constant relative humidity atmosphere. *J. Atmos. Sci.*, **69 (8)**, 2538–2550.

Sandu, I. and B. Stevens, 2011: On the factors modulating the stratocumulus to cumulus transitions. *J. Atmos. Sci.*, **68 (9)**, 1865–1881.

Sandu, I., B. Stevens, and R. Pincus, 2010: On the transitions in marine boundary layer cloudiness. *Atmos. Chem. Phys.*, **10 (5)**, 2377–2391.

Schalkwijk, J., E. J. Griffith, F. H. Post, and H. J. J. Jonker, 2011: High-performance simulations of turbulent clouds on a desktop PC: Exploiting the GPU. *Bull. Amer. Meteor. Soc.*, **93 (3)**, 307–314.

Schalkwijk, J., H. J. Jonker, A. P. Siebesma, and E. van Meijgaard, 2014: Weather forecasting using GPU-based large-eddy simulations. *Bull. Amer. Meteor. Soc.*

Schubert, W., J. Wakefield, E. S. Cox, and K. Stephen, 1979: Marine stratocumulus convection. Part II: Horizontally inhomogeneous solutions. *J. Atmos. Sci.*, **36**, 1308–1324.

Seifert, A. and K. D. Beheng, 2001: A double-moment parameterization for simulating autoconversion, accretion and selfcollection. *Atmos. Res.*, **59-60**, 265–281.

Shu, C.-W. and S. Osher, 1988: Efficient implementation of essentially non-oscillatory shock-capturing schemes. *Journal of Computational Physics*, **77 (2)**, 439–471.

Shu, C.-W. and S. Osher, 1989: Efficient implementation of essentially non-oscillatory shock-capturing schemes, II. *Journal of Computational Physics*,

83 (1), 32–78.

Shutts, G. J. and M. E. B. Gray, 1994: A numerical modelling study of the geostrophic adjustment process following deep convection. *Q.J.R. Meteorol. Soc.*, **120 (519)**, 1145–1178.

Siems, S. T., C. S. Bretherton, M. B. Baker, S. Shy, and R. E. Breidenthal, 1990: Buoyancy reversal and cloud-top entrainment instability. *Q.J.R. Meteorol. Soc.*, **116 (493)**, 705–739.

Sigg, R. and G. Svensson, 2004: Three-dimensional simulation of the ASTEX Lagrangian 1 field experiment with a regional numerical weather prediction model. *Q.J.R. Meteorol. Soc.*, **130 (597)**, 707–724.

Smolarkiewicz, P. K., 2006: Multidimensional positive definite advection transport algorithm: An overview. *Int. J. Numer. Meth. Fluids*, **50 (10)**, 1123–1144.

Smolarkiewicz, P. K. and W. W. Grabowski, 1990: The multidimensional positive definite advection transport algorithm: Nonoscillatory option. *J. Comput. Phys.*, **86 (2)**, 355–375.

Soden, B. J. and I. M. Held, 2006: An assessment of climate feedbacks in coupled ocean-atmosphere models. *J. Climate*, **19 (14)**, 3354–3360.

Stephens, G. L., 2005: Cloud feedbacks in the climate system: A critical review. *J. Climate*, **18 (2)**, 237–273.

Stevens, B., 2002: Entrainment in stratocumulus-topped mixed layers. *Q.J.R. Meteorol. Soc.*, **128 (586)**, 2663–2690.

Stevens, B., W. R. Cotton, G. Feingold, and C.-H. Moeng, 1998: Large-eddy simulations of strongly precipitating, shallow, stratocumulus-topped boundary layers. *J. Atmos. Sci.*, **55 (24)**, 3616–3638.

Stevens, B., C.-H. Moeng, and P. P. Sullivan, 1999: Large-eddy simulations of radiatively driven convection: Sensitivities to the representation of small scales. *J. Atmos. Sci.*, **56 (23)**, 3963–3984.

Stevens, B. and A. Seifert, 2008: Understanding macrophysical outcomes of microphysical choices in simulations of shallow cumulus convection. *J. Meteor. Soc. Japan*, **86A**, 143–162.

Stevens, B., G. Vali, K. Comstock, R. Wood, M. C. Van Zanten, P. H. Austin, C. S. Bretherton, and D. H. Lenschow, 2005a: Pockets of open cells and drizzle in marine stratocumulus. *Bull. Amer. Meteor. Soc.*, **86 (1)**, 51–57.

Stevens, B., et al., 2001: Simulations of trade wind cumuli under a strong inversion. *J. Atmos. Sci.*, **58 (14)**, 1870–1891.

Stevens, B., et al., 2003a: Dynamics and chemistry of marine stratocumulus–DYCOMS-II. *Bull. Amer. Meteor. Soc.*, **84 (5)**, 579–593.

Stevens, B., et al., 2003b: On entrainment rates in nocturnal marine stratocumulus. *Q.J.R. Meteorol. Soc.*, **129 (595)**, 3469–3493.

Stevens, B., et al., 2005b: Evaluation of large-eddy simulations via observations of nocturnal marine stratocumulus. *Mon. Wea. Rev.*, **133 (6)**, 1443–1462.

Stevens, D. E., A. S. Ackerman, and C. S. Bretherton, 2002: Effects of domain size and numerical resolution on the simulation of shallow cumulus convection. *J. Atmos. Sci.*, **59 (23)**, 3285–3301.

Stevens, D. E. and S. Bretherton, 1996: A forward-in-time advection scheme and adaptive multilevel flow solver for nearly incompressible atmospheric flow. *J. Comput. Phys.*, **129 (2)**, 284–295.

Stull, R., 1988: *An Introduction to Boundary Layer Meteorology*. Kluwer Academic Publishers.

Svensson, G., M. Tjernström, and D. Koračin, 2000: The sensitivity of a stratocumulus transition: Model simulations of the ASTEX first Lagrangian. *Bound.-Layer Meteor.*, **95 (1)**, 57–90.

Taylor, K. E., R. J. Stouffer, and G. A. Meehl, 2011: An overview of CMIP5 and the experiment design. *Bull. Amer. Meteor. Soc.*, **93 (4)**, 485–498.

Teixeira, J., et al., 2011: Tropical and subtropical cloud transitions in weather and climate prediction models: The GCSS/WGNE pacific cross-section intercomparison (GPCI). *J. Climate*, **24 (20)**, 5223–5256.

Toon, O. B., C. P. McKay, T. P. Ackerman, and K. Santhanam, 1989: Rapid calculation of radiative heating rates and photodissociation rates in inhomogeneous multiple scattering atmospheres. *J. Geophys. Res.*, **94 (D13)**, 16 287–16 301.

Turton, J. D. and S. Nicholls, 1987: A study of the diurnal variation of stratocumulus using a multiple mixed layer model. *Q.J.R. Meteorol. Soc.*, **113 (477)**, 969–1009.

Uchida, J., C. S. Bretherton, and P. N. Blossey, 2010: The sensitivity of stratocumulus-capped mixed layers to cloud droplet concentration: Do LES and mixed-layer models agree? *Atmos. Chem. Phys.*, **10**, 4097–4109.

Van der Dussen, J. J., S. R. de Roode, S. D. Gesso, and A. P. Siebesma, 2015: An les model study of the influence of the free tropospheric thermodynamic conditions on the stratocumulus response to a climate perturbation. *J. Adv. Model. Earth Syst.*, n/a–n/a.

Van der Dussen, J. J., S. R. de Roode, and A. P. Siebesma, 2014: Factors controlling rapid stratocumulus cloud thinning. *J. Atmos. Sci.*, **71 (2)**, 655–664.

Van der Dussen, J. J., et al., 2013: The GASS/EUCLIPSE model intercomparison of the stratocumulus transition as observed during ASTEX: LES results. *J. Adv. Model. Earth Syst.*, **5**, 483–499.

vanZanten, M. C., P. G. Duynkerke, and J. W. M. Cuijpers, 1999: Entrainment parameterization in convective boundary layers. *J. Atmos. Sci.*, **56 (6)**, 813–828.

vanZanten, M. C., B. Stevens, G. Vali, and D. H. Lenschow, 2005: Observations of drizzle in nocturnal marine stratocumulus. *J. Atmos. Sci.*, **62 (1)**, 88–106.

vanZanten, M. C., et al., 2011: Controls on precipitation and cloudiness in simulations of trade-wind cumulus as observed during RICO. *J. Adv. Model. Earth Syst.*, **3 (6)**, 19.

Vecchi, G. A. and B. J. Soden, 2007: Global warming and the weakening of the tropical circulation. *J. Climate*, **20 (17)**, 4316–4340.

Vial, J., J.-L. Dufresne, and S. Bony, 2013: On the interpretation of inter-model spread in CMIP5 climate sensitivity estimates. *Climate Dyn.*, **41 (11-12)**, 3339–3362.

Vickers, D. and L. Mahrt, 2010: Sea-surface roughness lengths in the midlatitude coastal zone. *Q.J.R. Meteorol. Soc.*, **136 (649)**, 1089–1093.

Wang, Q. and D. H. Lenschow, 1995: An observational study of the role of penetrating cumulus in a marine stratocumulus-topped boundary layer. *J. Atmos. Sci.*, **52 (16)**, 2778–2787.

Webb, M. J., F. H. Lambert, and J. M. Gregory, 2013: Origins of differences in climate sensitivity, forcing and feedback in climate models. *Climate Dynamics*,

40 (3-4), 677–707.

Wicker, L. J. and W. C. Skamarock, 2002: Time-splitting methods for elastic models using forward time schemes. *Mon. Wea. Rev.*, **130 (8)**, 2088–2097.

Williams, K. and M. Webb, 2009: A quantitative performance assessment of cloud regimes in climate models. *Climate Dynamics*, **33 (1)**, 141–157–.

Wood, R., 2005: Drizzle in stratiform boundary layer clouds. Part I: Vertical and horizontal structure. *J. Atmos. Sci.*, **62 (9)**, 3011–3033.

Wood, R., 2012: Stratocumulus clouds. *Mon. Wea. Rev.*, **140**, 2373–2423.

Wood, R. and C. S. Bretherton, 2004: Boundary layer depth, entrainment, and decoupling in the cloud-capped subtropical and tropical marine boundary layer. *J. Climate*, **17 (18)**, 3576–3588.

Wyant, M. C., C. S. Bretherton, H. A. Rand, and D. E. Stevens, 1997: Numerical simulations and a conceptual model of the stratocumulus to trade cumulus transition. *J. Atmos. Sci.*, **54 (1)**, 168–192.

Xiao, H., C.-M. Wu, and C. R. Mechoso, 2011: Buoyancy reversal, decoupling and the transition from stratocumulus to shallow cumulus topped marine boundary layers. *Climate Dyn.*, **37 (5-6)**, 971–984.

Xu, K.-M., A. Cheng, and M. Zhang, 2010: Cloud-resolving simulation of low-cloud feedback to an increase in sea surface temperature. *J. Atmos. Sci.*, **67 (3)**, 730–748.

Yamaguchi, T. and D. A. Randall, 2008: Large-eddy simulation of evaporatively driven entrainment in cloud-topped mixed layers. *J. Atmos. Sci.*, **65 (5)**, 1481–1504.

Yamaguchi, T. and D. A. Randall, 2012: Cooling of entrained parcels in a large-eddy simulation. *J. Atmos. Sci.*, **69 (3)**, 1118–1136.

Yamaguchi, T., D. A. Randall, and M. F. Khairoutdinov, 2011: Cloud modeling tests of the ULTIMATE-MACHO scalar advection scheme. *Mon. Wea. Rev.*, **139 (10)**, 3248–3264.

Zhang, M., C. Bretherton, M. Webb, and A. Siebesma, 2010: CFMIP-GCSS intercomparison of large eddy models and single column models (CGILS). *GEWEX News*, **20**, 6–8.

Zhang, M., et al., 2013: CGILS: Results from the first phase of an international project to understand the physical mechanisms of low cloud feedbacks in single column models. *J. Adv. Model. Earth Syst.*, **5 (4)**, 826–842.

Zhang, T., K. Stamnes, and S. A. Bowling, 2001: Impact of the atmospheric thickness on the atmospheric downwelling longwave radiation and snowmelt under clear-sky conditions in the arctic and subarctic. *J. Climate*, **14 (5)**, 920–939.

Zhu, P., et al., 2005: Intercomparison and interpretation of single-column model simulations of a nocturnal stratocumulus-topped marine boundary layer. *Mon. Wea. Rev.*, **133 (9)**, 2741–2758.

About the Author

Johan van der Dussen, born 31 January 1986 in Dordrecht

1998-2004	CSG De Lage Waard, Papendrecht
2004-2007	BSc Applied Physics, Delft University of Technology, Delft
2007-2010	MSc Applied Physics, Delft University of Technology, Delft
2009-2010	Internship, Meteo Consult, Wageningen
2010-2014	PhD project, Delft University of Technology, Delft
Present	Engineer, Senior Aerospace Bosman BV, Barendrecht

Peer Reviewed

J.J. van der Dussen, S.R. de Roode, A.S. Ackerman, P.N. Blossey, C.S. Bretherton, M.J. Kurowski, A.P. Lock, R.A.J. Neggers, I. Sandu and A.P. Siebesma, 2013: The GASS/EUCLIPSE model intercomparison of the stratocumulus transition as observed during ASTEX: LES results. *Journal of Advances in Modeling Earth Systems*, **5**, 483–499.

J.J. van der Dussen, S.R. de Roode and A.P. Siebesma, 2014: Factors controlling rapid stratocumulus cloud thinning. *Journal of the Atmospheric Sciences*, **71** (**2**), 655–664.

S. Dal Gesso, J.J. van der Dussen, A.P. Siebesma, S.R. de Roode, I.A. Boutle, Y. Kamae, R. Roehrig and J. Vial, 2015: A Single-column model intercomparison on the stratocumulus representation in present-day and future climate. *Journal of Advances in Modeling Earth Systems*

J.J. van der Dussen, S.R. de Roode, S. Dal Gesso and A.P. Siebesma, 2015: An LES model study of the influence of the free troposphere on the stratocumulus response to a climate perturbation. *Journal of Advances in Modeling Earth Systems*

J.J. van der Dussen, S.R. de Roode and A.P. Siebesma, 2015: How large-scale subsidence affects stratocumulus transitions. *Atmospheric Chemistry and Physics*, submitted.

R.A.J. Neggers, A.S. Ackerman, W. Angevine, E. Basile, I. Beau, P.N. Blossey, I. Boutle, C. de Bruijn, A. Cheng, J.J. van der Dussen, J. Fletcher, S. Dal Gesso, H. Kawai, S. Kumar, V. Larson, M.-P. Lefebvre, A. P. Lock, W. de Rooij, I. Sandu and H. Xiao, 2015: Single-column model simulations of subtropical marine boundary-layer cloud transitions under weakening inversions. *Journal of Advances in Modeling Earth Systems*, in preparation

P.N. Blossey, C.S. Bretherton, A. Cheng, J.J. van der Dussen, S. Endo, T. Heus and A. Lock, 2015: Marine low cloud sensitivity to increased CO_2 and a CMIP3 composite climate perturbations: Phase 2 of the CGILS LES intercomparison. *Journal of Advances in Modeling Earth Systems*, in preparation

Conference Proceedings

S.R. de Roode and J.J. van der Dussen, 2010: Large-eddy simulation of a stratocumulus to cumulus cloud transition as observed during ASTEX. *Paper presented at the 19th Symposium on Boundary Layers and Turbulence*, Keystone, Colo.

J.J. van der Dussen, S.R. de Roode and A.P. Siebesma, 2012: Large-eddy simulation sensitivity experiments of the ASTEX stratocumulus to cumulus transition. *Paper presented at the 20th Symposium on Boundary Layers and Turbulence*, Boston, Mass.

S.R. de Roode, I. Sandu, J.J. van der Dussen, A.S. Ackerman, P.N. Blossey, A. Lock, A.P. Siebesma and B. Stevens, 2012: LES results of the EUCLIPSE Lagrangian stratocumulus to shallow cumulus transition cases. *Paper presented at the 20th Symposium on Boundary Layers and Turbulence*, Boston, Mass.

Dankwoord

Je overschat zo gemakkelijk je eigen aandeel en vergeet wat je geworden bent uitsluitend door anderen.

— Dietrich Bonhoeffer, *Verzet en Overgave*

Het is al meer dan 6 jaar geleden dat ik kwam informeren voor een Master eindproject bij de groep Clouds, Climate and Air Quality. Stephan, je enthousiasme voor het vakgebied heeft me toen overgehaald om voor het onderwerp stratocumulus transities te kiezen. Ook tijdens mijn promotieproject wist je me steeds weer te motiveren met dit aanstekelijke enthousiasme voor alles wat je doet, of het nu gaat om onderzoek doen, college geven of wielrennen. Na ieder overleg (waar je altijd tijd voor maakte) kon ik weer met nieuwe ideeën en vol goede moed verder. Ik heb ontzettend veel van je geleerd en ik ben je dankbaar voor je hulp en de kansen die je me hebt geboden.

Pier, ook jij bent onmisbaar geweest in de afgelopen periode. Doordat je maar één dag per week in Delft werkt, hebben we elkaar minder vaak gesproken, maar desondanks was je steeds goed op de hoogte van de voortgang van het onderzoek. Je bent altijd behulpzaam, geïnteresseerd en ontspannen, ondanks je overvolle agenda. Bedankt dat je, met je immense inzet voor EUCLIPSE, dit prachtige promotieproject mogelijk hebt gemaakt.

Onlangs hoorde ik van een onderzoek waaruit bleek dat de kans om een promotieproject succesvol af te ronden aanzienlijk toeneemt door de aanwezigheid van collega-PhDs. Dit kan ik absoluut beamen. Ik heb ontzettend veel hulp en nog meer gezelligheid te danken aan mijn Delftse collega's. Vanaf het begin kon ik met al mijn DALES gerelateerde problemen (die ik overigens vaak zelf veroorzaakte) bij Steef aankloppen. Ook van Jerôme heb ik op dat gebied veel geleerd. Ik sta steeds weer versteld van jullie enorme kennis en van jullie vermogen om binnen no-time problemen te begrijpen en op te lossen. De dagelijkse koffie- en lunchpauzes zorgden steeds weer een welkome onderbreking. Bedankt, Patrick, voor het strikt handhaven daarvan. Vincent, dankzij jou mooie verhalen over je klimexpedities waren de ontelbare fietstochten richting het station aan het eind van de dag nooit saai. Sara, I really feel lucky to have been in the company of an experienced traveler like you during the many trips we went on. It has been great having you as a colleague and I have enjoyed working together with you our articles. Jessica en Jesse, jullie aanwezigheid in Delft op de woensdagen zorgden steeds weer voor veel levendigheid binnen de vakgroep.

Degene die al deze mensen in de afgelopen jaren bij elkaar heeft gehouden, zelfs door een verhuizing heen, is Harm. Bedankt dat ik onderdeel mocht zijn van je vakgroep. Erwin, bedankt voor het draaiend houden van het netwerk en voor het beantwoorden van al mijn Linux gerelateerde vragen. Alle studenten die

hun Bachelor of Master eindproject hebben gedaan in onze groep wil ook graag bedanken. Ik heb veel van jullie geleerd.

I am grateful to Peter Blossey, who was always patient enough to provide me with detailed responses to my countless questions about advection and microphysics schemes. He had many good suggestions for the model intercomparison article and was of great help during the work on the CGILS project. I am also grateful for the pleasant cooperation with the other coauthors of the first article in this thesis: Andy Ackerman, Chris Bretherton, Marcin Kurowski, Adrian Lock, Roel Neggers and Irina Sandu. Your input on the early drafts has greatly improved the final result and helped me a lot during the rest of my PhD project. Working with you has been a real privilege.

Tot slot wil ik alle familie en vrienden bedanken. Jullie zijn met te veel om iedereen persoonlijk te noemen, maar dat betekent niet dat jullie minder belangrijk zijn! Bedankt voor jullie interesse en voor de broodnodige afleiding op zijn tijd. Zonder jullie steun zou ik dit project nooit hebben kunnen afmaken. En natuurlijk mijn lieve Pauline, bedankt dat je er altijd voor me bent. Bovenal prijs en dank ik God voor de onmisbare hulp en zegen waarmee Hij mij in deze periode heeft geleid.